Friedrich-Alexander-Universität
Erlangen-Nürnberg

Simulation and Validation of an Optical-Thermal Model of a Molten Salt Solar Tower Receiver

Master Thesis

Handed in by:	Shimaa Ismail
Matriculation number:	23034736
Advisor:	Dr.-Ing. Manuel Münsch (FAU)
First supervisor:	Konrad Busch (DLR)
Second supervisor:	Kathrin Ingenwepelt (DLR)
Editing time:	1.08.2024 – 03.02.2025

Written at

Institute of Fluid Mechanics (LSTM),

Friderich-Alexandria-Universität Erlangen - Nürnberg

in Cooperation with DLR Institute of Solar Research

Declaration of authorship

I confirm that I have written this thesis unaided and without using sources other than those listed and that this thesis has never been submitted to another examination authority and accepted as part of an examination achievement, neither in this form nor in a similar form. All content that was taken from a third party either verbatim or in substance has been acknowledged as such.

Erlangen, January 2025

Shimaa Ismail
(Matriculation number: 23034736)

Acknowledgement

I would like to thank my supervisor Dr. Manuel Münsch for his incredible support and valuable suggestions during my thesis.

First and foremost, I would like to thank my Advisor, Dr. Manuel Münsch at FAU University, for his incredible support and valuable suggestions.

I am also deeply grateful to my supervisor, Mr. Konrad Busch, and Ms. Kathrin Ingenwepelt at DLR. Their continuous encouragement, helpful advice, and motivation made a significant difference throughout this journey. They were always enthusiastic and eager to assist in any way they could, and it was a pleasure working with them.

Lastly, I want to thank my parents and friends for their unwavering support and motivation. Their belief in me and constant encouragement kept me going, and I couldn't have done this without them.

I would like to express my sincere gratitude to my supervisor Mr. Konrad Busch, and Ms. Kathrin Ingenwepelt at DLR for thier continuous guidance, encouragement and motivating me throughout the thesis. She were very enthusiastic to assist in any way they could and It was a pleasure working with them.

Finally, I wish to thank my parents and friends for their continuous support and motivation throughout my study.

Abstract

Concentrated Solar Power (CSP) plants may play a key role in future energy systems, offering clean, cost-effective, and large-scale energy generation. Solar tower plants using solar salts are the most popular among other types due to their cost-effective storage and ability to provide dispatchable electricity. These plants typically have an outlet salt temperature of 565°C, commonly paired with a subcritical Rankine cycle. Increasing the outlet temperature to 600°C improves efficiency and reduces the Levelized Cost of Electricity (LCOE) by using a supercritical Rankine cycle. However, exceeding 565°C can cause salt degradation and higher corrosion rates.

In the High Performance Molten Salt II (HPMS-II) Project, the receiver system is pressurized with synthetic air, stabilizing the molten salt mixture (60% $NaNO_2$ + 40% KNO_3) at higher temperatures, allowing the outlet temperature to reach up to 600°C. In the latest measurement campaign DLR achieved a maximum outlet temperature of 602°C.

The objective of this thesis is to study, validate, and optimize the thermo-optical behavior of the HPMS-II receiver during preheating and solar operation.The study begins with optical simulations to determine the heat flux densities reflected onto the receiver surface using ray-tracing software (SPRAY). Subsequently, the optical simulation is optimized. Parameters influencing optical efficiency—such as the power reflected by the heliostats, the power incident on the receiver, and the solar absorptance of the receiver geometry—are also evaluated.

The incident flux density obtained from the optical simulation serves as a boundary condition for thermal simulations. Two types of thermal simulations are conducted: a transient simulation for preheating operations and a steady-state simulation for solar operations. To calculate convection losses from the outer wall of the receiver to the ambient environment, the heat transfer coefficient is treated as a function of the outer wall temperature. Additionally, a CFD model is developed to compute the heat transfer coefficient within the tubes during preheating operation.

Contents

List of Figures

List of Tables

List of Abbreviations

MFT Multifocus Tower

DNI Direct Normal Irradiance

GA Genetic Algorithm

HTF Heat Transfer Fluid

HPMS High Performance Molten Salt

DLR German Aerospace Center

SPRAY Solar Power Raytracing Tool

LCOE Levelized Cost Of Electricity

IRENA International Renewable Energy Agency

CSP Concentrated Solar Thermal Power

SPT Solar Power Tower

CFD Computational Fluid Dynamics

FEM Einite Element Method

MSE Mean Square Error

RMS Root Mean Square

Nomenclature

β	Coefficient of volume expansion	[1/K]
$\Delta T/\Delta x$	Temperature gradient	[K/m]
$\dot{m}$	Mass flow rate	[kg/s]
$\dot{Q}_{\mathrm{Rad}}$	Radiative heat transfer rate	[W]
ϵ	Emissivity of the body	[-]
μ	Dynamic viscosity of the fluid	[Pa · s]
ν	Kinematic viscosity	[m^2/s]
ρ	Density	[kg/m^3]
σ	Stefan-Boltzmann constant (5.67×10^{-8})	[W/($m^2 \cdot K^4$)]
Gr_D	Grashof number for characteristic diameter D	[-]
Gr_L	Grashof number for characteristic length L_c	[-]
Nu	Nusselt number	[-]
Pr	Prandtl number at the mean fluid temperature	[-]
$\mathrm{Pr}_{t,i}$	Prandtl number at the inner wall temperature	[-]
Ra	Rayleigh number	[-]
ξ	Friction factor	[-]

A	Area	$[m^2]$
A_s	Surface area for convection heat transfer	$[m^2]$
D	Diameter of the tube	$[m]$
g	Gravitational acceleration	$[m/s^2]$
h	Convective heat transfer coefficient	$[W/m^2 \cdot K]$
h_{combined}	Combined CONVECTIVE heat transfer coefficient	$[W/m^2 \cdot K]$
h_{fc}	Forced convective heat transfer coefficient	$[W/m^2 \cdot K]$
h_{nc}	Natural convective heat transfer coefficient	$[W/m^2 \cdot K]$
k	Thermal conductivity	$[W/m \cdot K]$
k_s/D	Relative roughness of the tube	[-]
l_{heat}	Length of the heated section	[m]
L_c	Characteristic length of the geometry	[m]
Q_{cond}	Heat conduction rate	[W]
$Q_{\text{Conv,amb}_1}$	Convective heat loss to the atmosphere	[W]
$Q_{\text{Conv,amb}_2}$	Convective heat loss to the ambient$_2$	[W]
$Q_{\text{Conv,HTF}}$	Convective heat transfer to the heat transfer fluid	[W]
Q_{conv}	Convective heat transfer rate	[W]
$Q_{\text{Rad,amb}_1}$	Radiative heat loss to the atmosphere	[W]
$Q_{\text{Rad,S2S}}$	Radiative heat exchange between surfaces	[W]
$Q_{\text{Reflection}}$	Heat lost due to reflected solar radiation	[W]

Q_{Solar}	Heat absorbed from solar radiation	[W]
r_i	Inner radius of the tube	[m]
Re	Reynolds number	[-]
T	Temperature	[K]
T_∞	Fluid temperature far from the surface	[°C]
$T_{\text{Wall,in}}$	Inner wall temperature	[°C]
$T_{\text{Wall,out}}$	Outer wall temperature	[°C]
T_{W}	Outer wall temperature	[°C]
T_f	Film temperature	[°C]
T_s	Surface temperature	[°C]
T_{salt}	Molten salt temperature	[°C]
v_m	Mean fluid velocity	[m/s]

Introduction

1 Motivation

Concentrated Solar Thermal Power (CSP) technology has emerged as a prominent method for harnessing solar energy to generate electricity. CSP systems are primarily classified into two mechanisms: line concentrating and point concentrating.

Line concentrating systems utilize a single-axis tracking mechanism that adjusts to the sun's movement, ensuring that solar radiation is continuously focused on the receiver pipes as illustrated in Figure 1. This single-axis tracking system is simpler to implement compared to **point concentrating systems**, which require tracking the sun along two axes as illustrated in Figure 2.

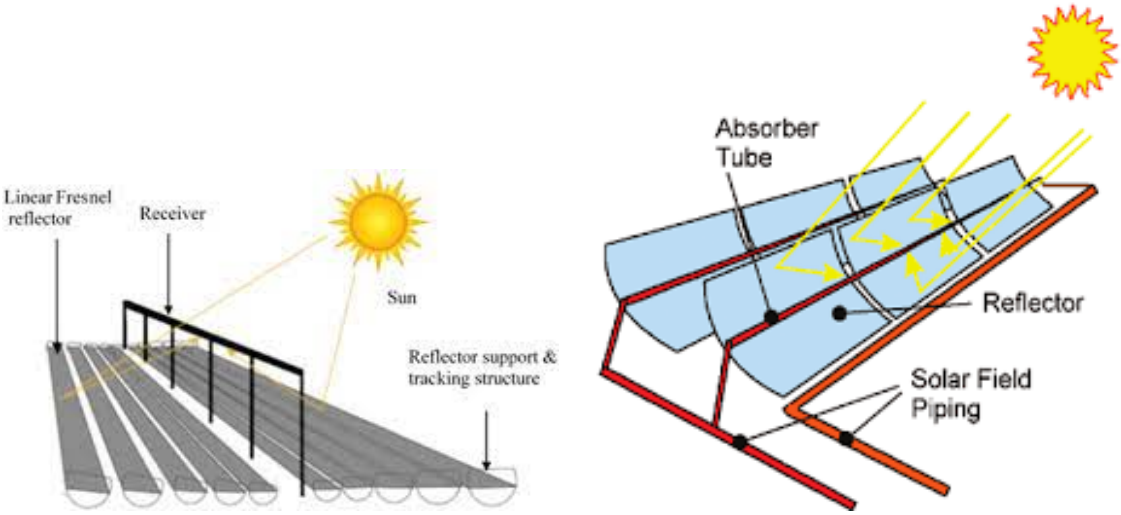

(a) Linear Fresnel reflector **(b)** parabolic trough collectors

Figure 1: Line Focus Concentrated Solar Power System.

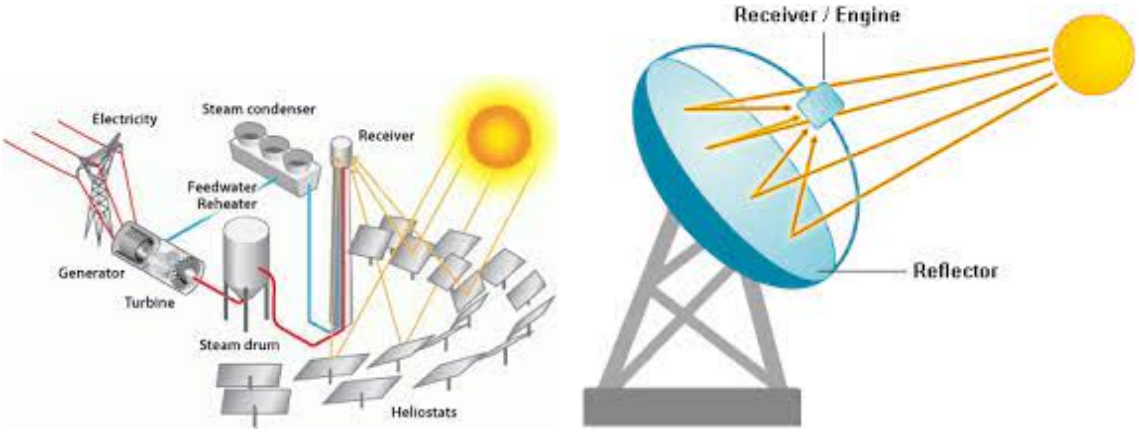

(a) solar tower **(b)** dish/engine system

Figure 2: Point Focus Concentrated Solar Power System.

Parabolic trough collectors and solar towers are among the most widely utilized technologies in CSP. Solar towers can achieve exceptionally high solar concentration levels, often exceeding 1,000 suns, enabling operation at significantly higher temperatures compared to parabolic trough collectors (IRENA) 2021. Additionally, solar towers offer the flexibility to integrate hybrid systems and storage solutions, enhancing their operational efficiency and versatility.

The Global Accumulative Capacity for Concentrated Solar Power, as reported by International Renewable Energy Agency (IRENA) 2024, shows a steady increase from 4600 MW in 2014 to 6876 MW in 2023. Between 2014 and 2017, growth was gradual, reaching 5200 MW, followed by a significant jump to 6312 MW in 2018. The period from 2019 to 2021 experienced stagnation around 6400 MW. However, renewed growth is observed in 2022 and 2023, with a 300 MW increase between these years, indicating advancements in CSP technology s shown in Figure 3.

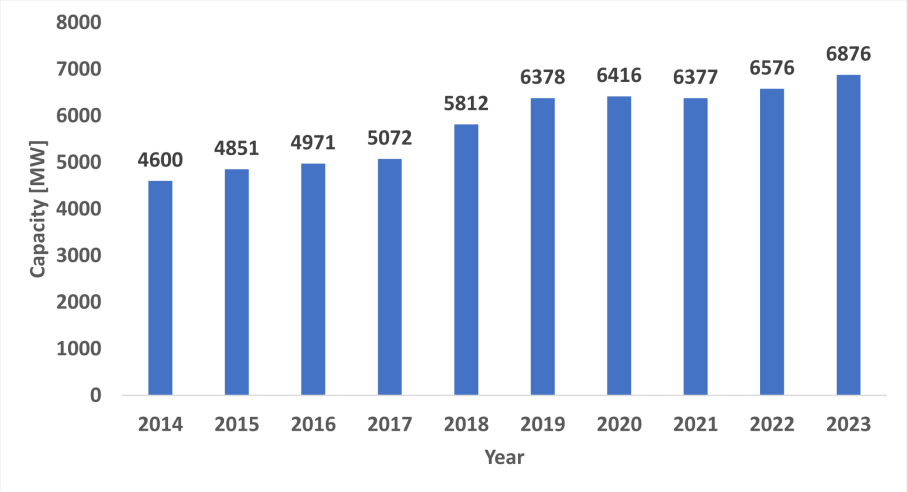

Figure 3: Global CSP Capacity International Renewable Energy Agency (IRENA) 2024.

The Solar Tower System achieves the highest temperatures among solar technologies. It utilizes mirrors, known as heliostats, to focus sunlight onto a central, elevated tower. At this focal point, the concentrated solar radiation is transferred to a heat transfer fluid, enabling efficient energy conversion. Despite its potential, significant technological challenges must be overcome before solar tower plants operating at high temperatures become commercially viable. A thorough understanding of the performance of the heliostat field and the receiver subsystem is therefore essential for designing an effective solar tower system.

Consequently, this work aims to reduce the cost of solar tower plants utilizing molten salt as a heat transfer and storage medium. The objective is to advance the design of high-efficiency receiver systems for the next generation of molten salt solar tower plants .

2 Objectives

This thesis is divided into four tasks to achieve the overall objective, which aims to address the following goals.

2.1 Optical Simulation

The main objective of the optical simulation is to calculate the incident flux reflected from the heliostat field onto the receiver, and distributed across its surface at pre-specified locations, called "Aim Points." To perform an accurate calculation of the incident flux and the associated losses, the software SPRAY, an in-house software, has been utilized. It is developed considering the heliostat alignment, optical performance, and environmental conditions in order to obtain the most accurate system behavior. A detailed explanation of the methodology and implementation of the simulation is presented in 2.

2.2 Validation of Optical Simulation Results with Experimental Data

The genetic algorithm was used to optimize the optical simulation, and it greatly improved the performance of the system. In this regard, the impact of the optimization was analyzed in depth, showing improvements in optical efficiency and system reliability. A simulation was performed and subsequently validated by comparing its predictions with experimental measurements obtained during both the preheating and solar operation phases. These results highlight the strength of the optimization process. Chapter 5 comprehensively discusses the analysis methods, and further, it shows the practical implications of this optimization for solar tower technology.

2.3 Thermal Simulation

Once the optical simulation is completed, the incident flux data was transferred to a thermal model using FEMRAY, an interface software connecting optical and thermal simulations. Then, a detailed thermal behaviour for such a receiver using different scenarios of operational conditions could be simulated in ANSYS Workbench: Chapter 6 introduces the concept by describing the integration process for

optical results into thermal analyses. Boundary conditions, such as convection and radiation, are included in the thermal model, as they are crucial for predicting the thermal response of the receiver. All of these will be described, along with the importance of their contribution to the system, in Chapter 3. The model predictions should be validated to ensure their reliability. This process includes selecting an optimal mesh that balances accuracy with the computational time required for running the simulation. The model validation, along with the criteria used for mesh selection, is discussed in detail in Chapter 4.

2.4 Validation of Thermal Simulation Results with Experimental Data

The primary objective of the thermal simulation is to validate the molten salt temperature as well as the rear sidetube temperature at the thermocouple locations, where measurements will be taken. There are two modes of operations, the preheating mode under a transient thermal model, and the solar operation under a steady-state simulation model. During the preheating operation, an optimization procedure was required to determine the effect of convection losses on the rear tube side by optimizing the ambient temperature. The optimization process, aimed at improving the accuracy of the simulation, was employed to refine the unknown parameters based on the experimental data. To ensure the accuracy of these estimates, the mean square error between the simulation results and the experimental measurements was used as the validation metric for these parameters, as outlined in Chapter 7. Additionally, a comparison between the convection and radiation losses has been addressed. These losses are important to understand, as they reflect the receiver's thermal performance.

1 Solar Power Tower Plant

This chapter describes the components of a solar tower power plant and compares current commercial molten salt power towers with the new generation of high-temperature molten salt systems.

1.1 Components of a Solar Power Tower Plant

A Solar Power power plant typically consists of a solar field containing thousands of heliostats focused on a central receiver atop a supporting tower. The system also includes a thermal energy storage system and a power block. The associated piping, storage tanks, and heat exchanger systems often involve up to three distinct working fluids: the heat transfer fluid (HTF) used in the receiver, the storage medium in the thermal energy storage tanks, and the working fluid driving the turbine, As illustrated in Figure 4.

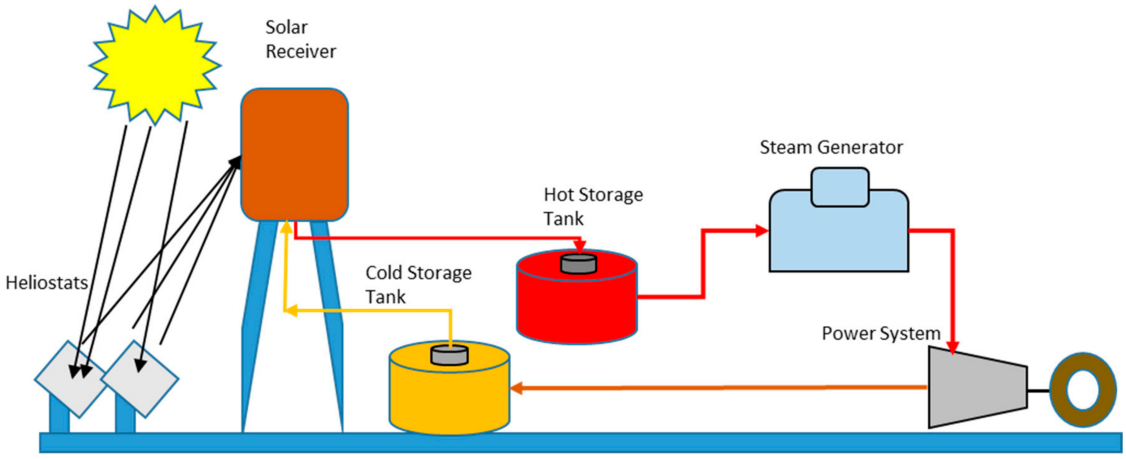

Figure 4: A Typical Configuration of Solar Power Tower Plants Albarbar and Arar 2019.

1.1.1 Heliostat

In solar tower thermal power plants, heliostats are essential components that direct sunlight to the receiver's heat-transfer fluid Mun and Tutul 2023. These mirrors, which are either flat or slightly concave, use a two-axis tracking system to continuously follow the sun's azimuth and altitude angles, maximizing energy collection efficiency throughout the plant's operation Zhang, Baeyens, et al. 2013.

1.1.2 Receiver

The receiver is located at the top of the tower structure and plays a critical role in solar tower power plants. Central receivers are characterized by the type of heat transfer medium they employ, which can include liquids, gases, or solid particles. Current commercial systems commonly use water/steam or molten salt receivers, typically integrated with steam-Rankine power cycles operating at temperatures below 600°C. Emerging technologies—such as volumetric air receivers, supercritical carbon dioxide (sCO_2) systems, solid particle receivers, and liquid-metal designs—are under extensive research and development, as summarized in Table 1.

The primary function of the receiver is to convert concentrated solar radiation into thermal energy, which is subsequently transferred to the heat transfer fluid (HTF) circulating through the system Zhu and Libby 2017. Among various HTFs studied for solar tower systems, molten salt is the most widely adopted in commercial projects due to its high thermal storage capacity and cost-effectiveness. This preference is evident in projects summarized in Table 2, where molten salt serves as the primary HTF SolarPACES 2024.

The heliostat field, comprising the heliostats and receiver, is a critical subsystem in solar power plants. It accounts for approximately 40%–50% of the facility's total investment cost and contributes significantly to system losses, representing around 40% of the total energy losses Hussaini et al. 2020.

Receiver Design	**HTF**	**Attributes**	**Limitations**
Volumetric Air Receiver	Air	• Extensive operating temperature range • Compatible with direct power cycles • Economic • Environmentally friendly	• Relatively low heat transfer coefficient • Large pumping power • Indirect storage required • Potentially high pressure in receiver
External receiver	Water/Steam	• Compatible with direct power cycles • Economic • Environmentally friendly	• Temperature range limited by available steam turbines • High pressure required for efficient direct power cycle • Indirect storage required at large scale • Cooling system required
External tabular receiver	Molten Salt	• High heat capacity and low cost • Compatible with direct storage • Nontoxic, nonflammable • Low vapor pressure at working temperature	• Operating temperature limited by chemical stability • Relatively high melting point creates salt freezing risks • Can cause pitting and corrosion at high temperature
External receiver	Liquid Metal	• Stable at high temperature • High heat transfer coefficients at high thermal loads	• Low heat capacity • High melting point • Relatively high cost • Can be corrosive, reactive, and/or toxic depending on most stainless alloys
Fluidized-bed/ Centrifugal receiver	Solid Particle	• Stable at high temperature • Compatible with direct storage • Compatible with high-efficiency air-Brayton and sCO_2 power cycles • Particles can be low cost	• Requires complex mass flow control and relatively high parasitic load • Requires efficient air-solid heat exchangers • Current designs result in lower thermal efficiency
Cavity receiver	Supercritical CO_2	• Stable over the typical engineering application temperature range • Low viscosity • Compatible with sCO_2 power cycle • Compatible with sensible-heating fluids for indirect storage • Environmentally benign in closed-cycle application	• Poor energy density at low pressure • Requires high pressure for efficient integration with sCO_2 power cycle • Requires indirect storage • Poor heat transport properties require high fluid velocity and induce large pressure loss • Moderately corrosive for stainless alloys at high temperatures

Table 1: Comparison of HTFs and Receiver Types for Central Receivers Zhu and Libby 2017, & Ho 2016 & Falahat and Gomaa 2022.

Country	**Project Name**	**CSP Technology**	**Capacity [MW]**	**HTF**	**Operational Date**
China	Cosin Solar	Solar Tower	100	Molten Salt	2022
United Arab Emirates	DEWA "NOOR"	Tower & Trough	700	Molten Salt	95% Completed as of 2023
Morocco	NOOR I,II,III	Tower & Trough	550	Molten Salt	Operational since 2018
South Africa	Redstone Tower	Solar Tower	100	Molten Salt	Expected completion by 2024
Chile	Cerro Dominador	Solar Tower	110	Molten Salt	Operating since 2021
Spain	Sener Solgest	Trough	110	Molten Salt	Under Construction
Israel	Ashalim	Tower & Trough	230	Molten Salt	Operational since 2019
USA	Crescent Dunes	Tower	110	Molten Salt	Operational since 2015;currently non-operational

Table 2: Recent Projects Utilizing Molten Salt as a Heat Transfer Fluid in Concentrated Solar Power Systems SolarPACES 2024.

1.1.3 Power Block

In the study by Kolb 2011, the selection of the steam Rankine cycle is determined by the outlet temperature of the HTF exiting the receiver. For molten salts with a maximum temperature of 565°C, the subcritical Rankine cycle is the most commonly employed configuration. However, if the HTF temperature increases to 600°C, it becomes possible to utilize a supercritical steam Rankine cycle. Furthermore, achieving a receiver salt temperature of 650°C allows for the implementation of an ultra-supercritical steam Rankine cycle, enabling significantly higher thermodynamic efficiency. The choice of the steam cycle is, therefore, closely linked to the HTF outlet temperature, as higher temperatures facilitate the adoption of more advanced and efficient thermodynamic cycles.

1.1.4 Thermal Storage

A key advantage of solar power tower (SPT) technology over other renewable energy systems is its capacity for large-scale thermal energy storage. This capability is particularly pronounced in molten salt-based SPTs, where the HTF serves both as the working fluid in the receiver and as the storage medium. The HTF is stored in two insulated tanks located at the base of the tower, as shown in Figure 4. To minimize heat loss, the tanks are thoroughly insulated, and internal mechanisms are employed to prevent thermal stratification, ensuring uniform temperature distribution throughout the stored salt Reyes Rodríguez Sánchez 2015.

1.2 Current Commercial Molten-Salt Power Towers

Molten-salt central receiver power systems use a tubular receiver positioned atop a tower. Solar energy, reflected by a field of heliostats, heats the receiver, with molten salt serving as both the heat transfer fluid and the receiver's cooling medium. As illustrated in Figure 5, the molten salt temperature increases from 290°C to 565°C within the receiver. The heated fluid is then directed to thermal storage via insulated pipes.

Hot salt from the storage system is withdrawn to produce steam in a molten-salt steam generator, which drives a Rankine cycle turbine to generate electricity. The cooled salt is cycled back to the thermal storage system and subsequently to the receiver. The thermal storage system stabilizes steam generation by mitigating fluctuations in solar input and enables energy production during non-solar periods, such as nighttime or cloudy conditions.

Throughout the process, the molten salt remains in a single liquid phase. Its high heat capacity allows for relatively compact storage tanks. With a hot salt temperature of 565°C, steam is produced at conditions comparable to those in conventional subcritical Rankine-cycle plants Kolb 2011.

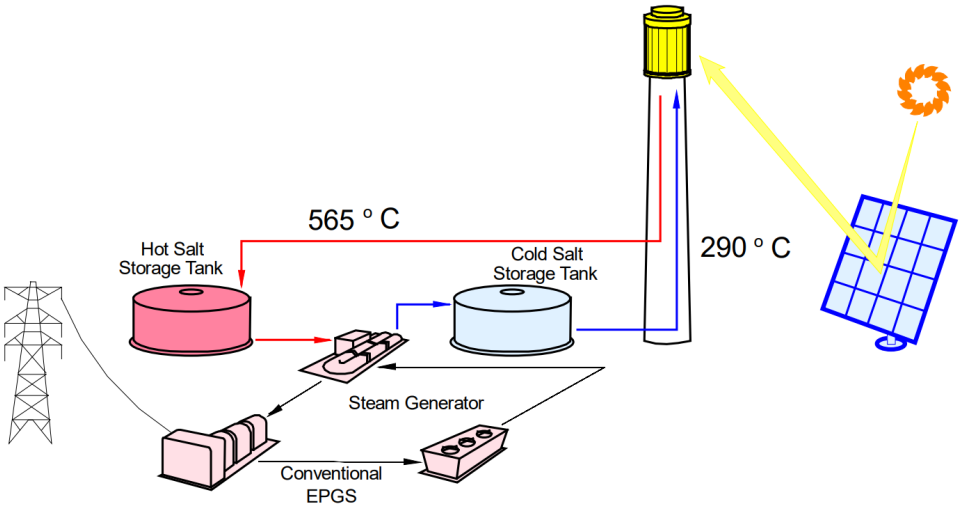

Figure 5: Flow Schematic of a Molten-Salt Central Receiver SystemKolb 2011.

Molten salt central tower systems are currently constrained by a maximum operating temperature of 565°C due to accelerated salt degradation and increased corrosion rates at higher temperatures Frantz, Ebert, et al. 2023. However, operating at receiver temperatures above 600°C offers significant potential for reducing the levelized cost of electricity (LCOE). Higher temperatures enable the integration of supercritical and ultrasupercritical steam cycles, which enhance cycle efficiency and further lower the LCOE Kolb 2011.

1.3 High Performance Molten Salt II Project

The scope of the HPMS-II Project is to demonstrate a closed-loop molten salt cycle using conventional Solar Salt, a mixture of 60% $NaNO_3$ and 40% KNO_3, with salt temperatures reaching up to 600 °C. The project also aims to measure the thermal efficiency of the receiver and validate the simulation models used during the design phase.

The test setup features a receiver designed as a scaled-down model of a commercial receiver panel, replicating and validating critical operational scenarios at 600 °C within a Technology Readiness Level 7 (TRL 7) environment Frantz, Ebert, et al. 2023.

In the system, molten salt is maintained at elevated temperatures to prevent solidification within the salt tank. A dedicated molten salt pump transfers the heated salt upward through a riser into a pressurized receiver inlet tank. At the receiver inlet, a primary control valve regulates the mass flow rate and outlet temperature. As the molten salt flows through the tubular receiver panels in a serpentine path, it is further heated by concentrated solar radiation from the heliostat field. The heated salt exits through the pressurized outlet tank, flows into a downcomer, and is returned to the storage tank as illustrated in Figure 6.

A molten-salt-to-air cooler is installed within the downcomer to reduce the salt temperature to the desired storage level. To maintain operational temperatures and prevent solidification of the salt, all piping and tanks are equipped with heat tracing systems. During nighttime or extended shutdown periods, the entire salt inventory can be drained and safely stored in the main salt tank. Unlike conventional systems, both the storage and outlet tanks are blanketed with synthetic air rather than being open to the atmosphere Cathy Frantz and Busch 2022.

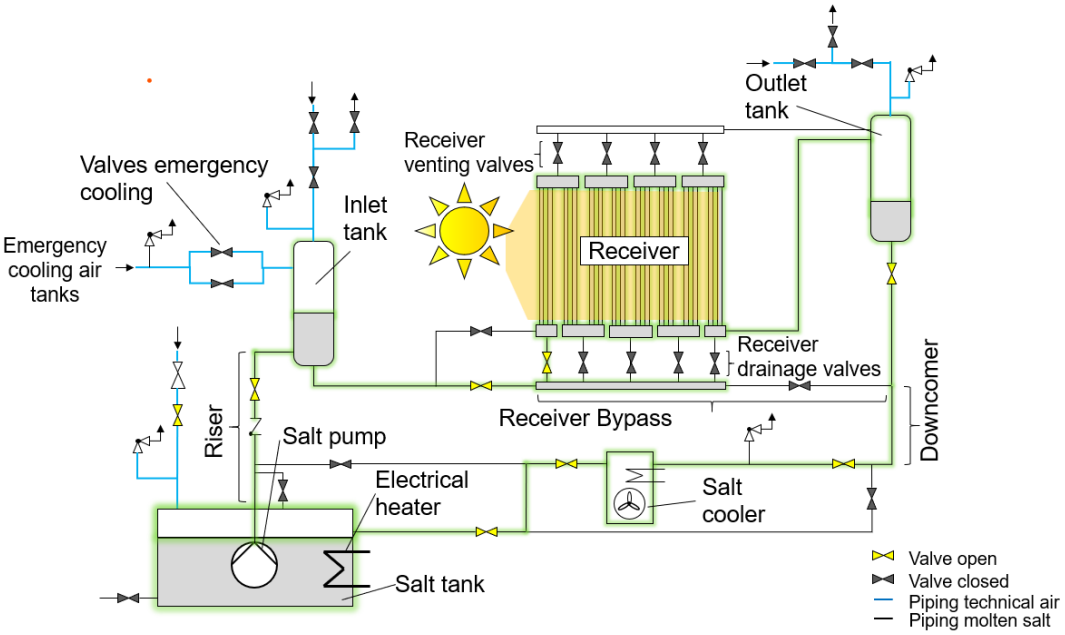

Figure 6: Simplified P&ID of the HPMS-II System.

2 Methodology

This chapter outlines the methodology used to evaluate the optical and thermal performance of the receiver system. The Monte Carlo ray tracing method is implemented to simulate and analyze the solar flux distribution on the receiver surface, providing detailed flux maps for further evaluation. The chapter also presents the governing thermal equations that model energy transfer within the receiver, incorporating both convection and radiation heat transfer mechanisms. Convection coefficients are determined for various operating conditions, while radiation heat losses are calculated based on the receiver's surface temperatures and emissivity.

2.1 Optical Model

The primary objective of optical simulation is to quantify the incident flux reaching the receiver. This is achieved by concentrating solar radiation using heliostats, which are directed toward strategically distributed aim points on the receiver. These aim points are selected to optimize energy capture and maximize efficiency. The flux density on the receiver surface can be evaluated using numerical or analytical methods, with the Monte Carlo ray tracing method being a widely adopted numerical approach.

Monte Carlo ray tracing involves generating and tracking a large number of rays as they traverse various optical components. By analyzing the intersection of these reflected rays with the receiver surface, a flux map is generated, providing detailed insights into the distribution of flux density Besarati et al. 2014.

The solar flux density on the receiver is influenced by multiple parameters, including DNI, the number and arrangement of focused heliostats, the reflectivity of heliostat surfaces, and optical imperfections. Optical errors encompass mirror slope errors,

which quantify surface imperfections and roughness García et al. 2015, as well as tracking inaccuracies in the heliostat drive mechanisms. Additionally, solar position parameters, such as elevation and azimuth angles, significantly influence the flux distribution. The incident heat flux is calculated using the SPRAY R.Buck 2024 and HeliOS control software, which provide detailed simulations and analyses for CSP system optimization.

SPRAY

SPRAY, an in-house ray tracing software tool developed by the German Aerospace Center (DLR), employs the Monte Carlo ray tracing method to calculate the solar flux distribution on the receiver in concentrating solar thermal systems. This method is characterized by its high flexibility, making it suitable for a wide range of applications in the field. The precision of this approach allows for detailed modeling of solar energy concentration, which is critical for optimizing the performance of the receiver system Hicdurmaz et al. 2024.

SPRAY generates rays on the heliostat surface, with each ray carrying energy based on factors such as direct normal irradiance (DNI), the number of rays produced, and the heliostat's surface area. These rays are reflected toward target points on the receiver, located in the Multifocus tower, as illustrated in Figure 7. SPRAY also calculates spillage losses caused by shading or atmospheric absorption by simulating ray attenuation, which reduces the number of rays reaching the receiver. Among the rays that reach the receiver, a portion is absorbed depending on the receiver's absorptivity, while the rest are reflected back into the environment.

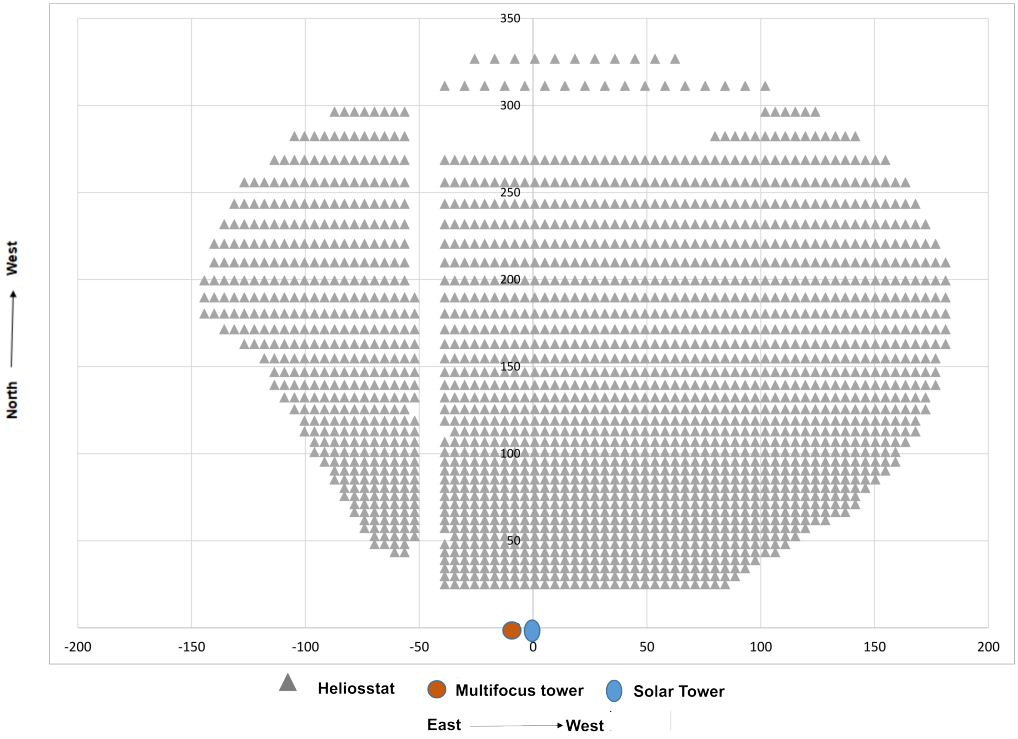

Figure 7: Illustration of the Heliostat Field at Jülich.

HeliOS

The HeliOS control system is designed to manage large heliostat fields, with the capacity to control over 20,000 heliostats. It ensures safe regulation of solar flux on the receiver by utilizing either real-time radiation simulation data or infrared measurements. HeliOS is a commercial project currently under development by DLR Geiger1 et al. 2018.

To regulate the heliostat array, the HeliOS system distributes 24 aim points across the receiver, modeling it as a 5x5 grid as shown in Figure 8. The distribution begins with aim point 0 in the upper left corner, aim point 4 in the upper right corner, aim point 20 in the lower left corner, and aim point 24 in the lower right corner.

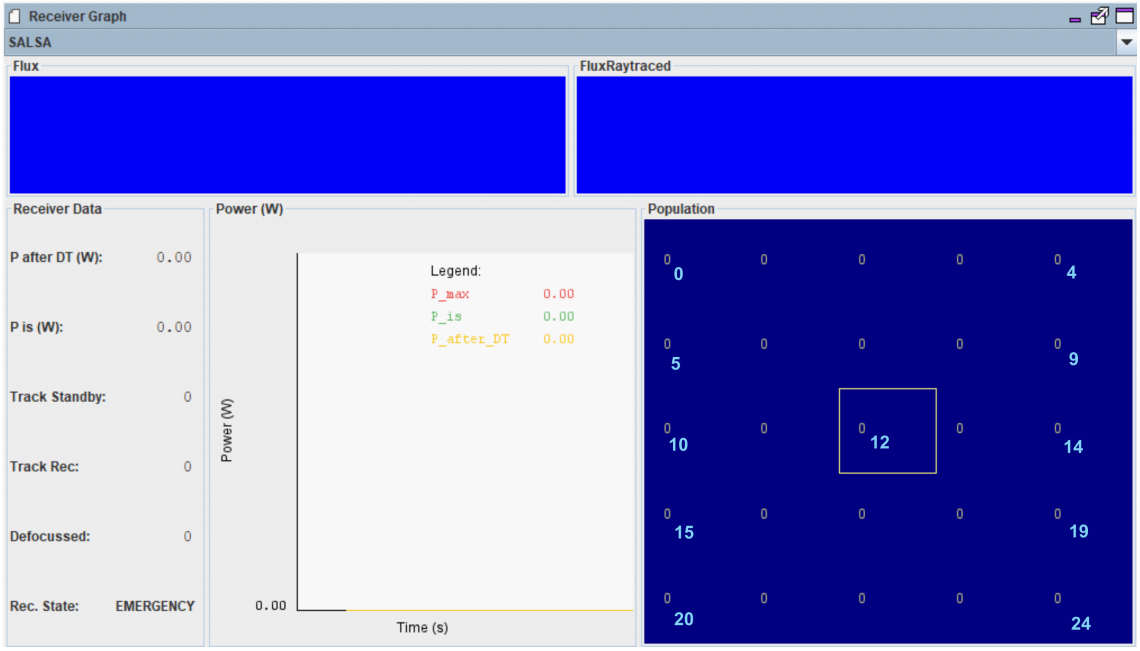

Figure 8: Illustration of Aim Point Distribution on the Receiver Surface.

2.2 Optimization

Over the past decade, genetic algorithms (GAs) have seen extensive application in optimizing solar thermal systems Besarati et al. 2014. GAs are optimization methods inspired by the principles of natural selection. These algorithms simulate evolutionary processes by generating a population of candidate solutions, referred to as "individuals," which evolve across multiple generations. Through genetic operations—such as selection, crossover, and mutation—GAs iteratively improve the population by favoring individuals that most closely satisfy the optimization criteria. This evolutionary approach enables GAs to effectively explore and exploit complex problem spaces, identifying near-optimal solutions for non-linear and multi-objective problems.

In the context of optimizing the solar flux distribution on a solar power tower receiver, a GA has been implemented to minimize the mean squared error between the simulated and measured flux density distributions. This optimization is achieved by adjusting the aiming points of individual heliostats based on three key parameters: the heliostat's slope error, and the x- and z-coordinates of its aiming points.

2.3 Thermal Model

Heat is defined as the energy transferred across the boundary of a thermodynamic system as a result of a temperature difference between the system and its surroundings. Heat transfer occurs through three primary mechanisms: conduction, convection, and radiation Çengel 2003.

2.3.1 Conduction

Energy transfer through conduction occurs when more energetic particles in a material pass energy to neighboring, less energetic particles through direct interactions. This process occurs in solids, liquids, and gases, although the mechanism varies across these states. In gases and liquids, conduction primarily results from molecular collisions and diffusion due to random molecules motion. In solids, energy transfer occurs through a combination of molecular vibrations within the lattice structure and the movement of free electrons that carry energy across the material Çengel 2003. The rate of heat conduction through a flat layer is directly proportional to the temperature difference across the layer and the area through which heat is transferred. Conversely, it is inversely proportional to the layer's thickness, as illustrated in Equation 2.1.

$$\dot{Q}_{\text{cond}} = kA\frac{T_1 - T_2}{\Delta x} = -kA\frac{\Delta T}{\Delta x} \quad \text{(W)} \tag{2.1}$$

Where:

k	= Thermal conductivity	[W/m K]
A	= Area	[m^2]
$\frac{\Delta T}{\Delta x}$	= Temperature gradient	[K/m]

If a heat balance is applied to an infinitesimal Cartesian volume element, it yields Fourier's differential equation, as shown in Equation 2.2:

$$\frac{\partial}{\partial x}\left(k\frac{\partial T}{\partial x}\right) + \frac{\partial}{\partial y}\left(k\frac{\partial T}{\partial y}\right) + \frac{\partial}{\partial z}\left(k\frac{\partial T}{\partial z}\right) + \dot{q} = \rho c\frac{\partial T}{\partial \tau} \tag{2.2}$$

2.3.2 Convection

Convection refers to the process of energy transfer that occurs between a solid surface and the nearby moving liquid or gas. Generally, increased fluid motion enhances the rate of convective heat transfer Çengel 2003. The rate of convective heat transfer is directly related to the temperature difference between the surface and the surrounding fluid. This relationship is effectively described by Newton's law of cooling, which can be expressed mathematically as illustrate in Equation 2.3:

$$\dot{Q}_{\text{conv}} = hA_s(T_s - T_\infty) \tag{2.3}$$

Where:

A_s	= Surface area for convection heat transfer	[m^2]
h	= Convection heat transfer coefficient	[W/m^2 K]
T_s	= Surface temperature	[°C]
T_∞	= Fluid temperature far from the surface	[°C]

Forced Convection

Forced convection occurs when a fluid is forced to flow over a surface by external mechanisms, such as fans, pumps, or wind. It is further classified into internal forced convection, which occurs within confined geometries such as pipes or ducts, and external forced convection, which takes place over surfaces exposed to the surrounding environment.

Internal Forced Convection:

The flow of liquids or gases through pipes or ducts is widely used in heating and cooling applications. The fluid flow behavior depends on the flow conditions and can be classified as either laminar or turbulent. At low velocities, the flow is streamlined and exhibits laminar characteristics. However, as the velocity increases beyond a critical threshold, the flow transitions to turbulence. For flow in a circular tube, the Reynolds number (Re), which quantifies the ratio of inertial forces to viscous forces in the fluid, is defined as:

$$Re = \frac{\rho v_m D}{\mu}, \tag{2.4}$$

Where:

v_m	= Mean fluid velocity	[m/s]
D	= Diameter of the tube	[m]
ρ	= Density of the fluid	[kg/m^3]
μ	= Dynamic viscosity of the fluid	[Pa·s]

The flow in a tube is considered laminar if Re $<$ 2300 and turbulent for Re $>$ 10000 Çengel 2003. To calculate the heat transfer of molten nitrate salt in a circular tube under turbulent flow conditions, various experiments were conducted at DLR. The results were compared with several correlations, including those by Gnielinski, Sieder-Tate, and Dittus-Boelter. It was concluded that the Gnielinski correlation, as illustrated in Equations 2.5 and 2.6, provides the best agreement with experimental data Frantz, Buck, et al. 2023.

$$\mathrm{Nu_{m,REF}} = \frac{\frac{\xi}{8}\cdot \mathrm{Re}\cdot \mathrm{Pr}}{1+12.7\cdot\sqrt{\frac{\xi}{8}}(\mathrm{Pr}^{2/3}-1)}\left[1+\left(\frac{2r_i}{l_{\mathrm{heat}}}\right)^{2/3}\right]\left(\frac{\mathrm{Pr}}{\mathrm{Pr}_{t,i}}\right)^{0.11} \tag{2.5}$$

$$\mathrm{Nu_{x,REF}} = \frac{\frac{\xi}{8}\cdot \mathrm{Re}\cdot \mathrm{Pr}}{1+12.7\cdot\sqrt{\frac{\xi}{8}}(\mathrm{Pr}^{2/3}-1)}\left[1+\frac{1}{3}\left(\frac{2r_i}{x}\right)^{2/3}\right]\left(\frac{\mathrm{Pr}}{\mathrm{Pr}_{t,i}}\right)^{0.11} \tag{2.6}$$

$$\xi = (1.8\cdot\log_{10}\mathrm{Re}-1.5)^{-2} \tag{2.7}$$

Where:

ξ	= Friction factor	
r_i	= Inner radius of the tube	[m]
l_{heat}	= Length of the heated section	[m]
x	= Axial position along the tube	[m]
Pr	= Prandtl number at the mean fluid temperature	[-]
$\mathrm{Pr}_{t,i}$	= Prandtl number at the inner wall temperature	[-]

Natural Convection

Natural convection refers to the process of heat transfer driven by buoyancy forces, which occur when temperature gradients cause density variations, resulting in fluid motion.The Grashof number (Gr) is a dimensionless parameter that represents the ratio of buoyancy forces to viscous forces acting on the fluid. It is expressed as:

$$\mathrm{Gr}_L = \frac{g\beta(T_s - T_\infty)L_c^3}{\nu^2} \tag{2.8}$$

Where:

g	= Gravitational acceleration	[m/s^2]
β	= Coefficient of volume expansion	[1/K]
T_s	= Surface temperature	[°C]
T_∞	= Fluid temperature far from the surface	[°C]
L_c	= Characteristic length of the geometry	[m]
ν	= Kinematic viscosity of the fluid	[m^2/s]

Empirical Relations For Free Convection:

Over the years, researchers have determined that the average heat transfer coefficients for free convection can be expressed in a standard functional form that applies across a wide range of situations.

$$\overline{\mathrm{Nu}_f} = C(\mathrm{Gr}_f\,\mathrm{Pr}_f)^m \tag{2.9}$$

Where:

f	= Properties evaluated at the film temperature	[°C]
T_f	= Film temperature, defined as $T_f = \frac{T_\infty + T_w}{2}$	[°C]
Nu	= Nusselt number	[-]
Ra	= Rayleigh number, defined as $\mathrm{Ra} = \mathrm{Gr} \cdot \mathrm{Pr}$	[-]

Free Convection From Vertical Planes and Cylinders

In general, a vertical cylinder can be approximated as a vertical flat plate under certain conditions, as shown in Equation 2.10. However, if the cylinder's diameter

is too small to satisfy this criterion, the average heat transfer coefficient should be adjusted by multiplying it by a factor F (see Equation 2.11) to account for the effects of curvature Holman 2009.

$$\frac{D}{L} \geq \frac{35}{\mathrm{Gr}_L^{1/4}} \tag{2.10}$$

$$F = 1.3(L/\mathrm{D})/\mathrm{Gr}_D]^{1/4} + 1 \tag{2.11}$$

$$\mathrm{Nu}_f = 0.10(\mathrm{Gr}_f \, \mathrm{Pr}_f)^{1/3} \tag{2.12}$$

Where:

D	= Diameter of the cylinder	[m]
L	= Length of the cylinder	[m]
Gr_L	= Grashof number based on the cylinder length	[-]
Gr_D	= Grashof number based on the cylinder diameter	[-]

More complicated relations have been provided by Churchill and Chu that are applicable over wider ranges of the Rayleigh number as illustrated in Equation 2.13:

$$\overline{\mathrm{Nu}} = \left(0.825 + \frac{0.387\,\mathrm{Ra}_L^{1/6}}{[1 + (0.492/\mathrm{Pr})^{9/16}]^{8/27}}\right)^2 \quad \text{for } 10^{-1} < \mathrm{Ra}_L < 10^{12} \tag{2.13}$$

Natural Convection In Enclosed Spaces

The fluid is enclosed between two vertical plates separated by a distance of δ, as illustrated in Figure 9. The *Grashof number*, Gr_δ, represents the ratio of buoyancy to viscous forces and is given by the following equation:

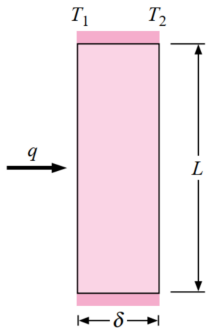

Figure 9: Free Convection in Enclosed Vertical Spaces.

$$\mathrm{Gr}_\delta = \frac{g\beta(T_1 - T_2)\delta^3}{\nu^2} \tag{2.14}$$

Where:

T_1, T_2	= Temperatures of the plates	[°C]
δ	= Distance between the vertical plates	[m]

The empirical correlations obtained were used to predict the heat transfer to a number of liquids under constant-heat-flux conditions with some conditions as illustrated in Equations 2.16 and 2.15 Holman 2009.

$$\mathrm{Nu} = 0.42\,\mathrm{Ra}_L^{1/4}\,\mathrm{Pr}^{0.012}\left(\frac{\delta}{L}\right)^{-0.3} \tag{2.15}$$

$$10 < \frac{H}{L} < 40, \quad 1 < \mathrm{Pr} < 2 \times 10^4, \quad 10^4 < \mathrm{Ra}_L < 10^7$$

$$\mathrm{Nu} = 0.46\,\mathrm{Ra}_L^{1/3} \tag{2.16}$$

$$1 < \frac{\delta}{L} < 40, \quad 1 < \mathrm{Pr} < 20, \quad 10^6 < \mathrm{Ra}_L < 10^9$$

Numerical studies have examined the impact of higher aspect ratios (AR = height / length) on natural convection in vertical rectangular enclosures with various fluids. Pendyala1 et al. 2021 investigated natural convection in air, water, engine oil, mercury, and glycerine within three-dimensional enclosures, considering aspect ratios from 0.125 to 150 and temperature differences between hot and cold surfaces ranging from 20 K to 100 K. These analyses were conducted using computational fluid dynamics simulations.

Convection In Solar Towers

Siebers and Kraabel 1984 describe the convective heat transfer coefficient for the receiver as a combination of two factors: the cross-flow transfer coefficient, influenced by wind velocity, and the natural convection coefficient.

$$\bar{h} = \left(h_{fc}^{3.2} + h_{nc}^{3.2}\right)^{\frac{1}{3.2}} \tag{2.17}$$

Where

h_{fc} = Forced heat transfer coefficient.
h_{nc} = Natural heat transfer coefficient.

The forced convection coefficient is influenced by the Nusselt and Reynolds numbers, which are based on the receiver's diameter (2.18), as well as the relative roughness of the tube (k_s/D), where k_s represents the effective sand grain roughness height. Since k_s cannot be determined in a straight forward manner, it is recommended to approximate k_s using the radius of a single receiver tube in the absence of a better estimation. This approach is illustrated in Equations (2.19), (2.20), (2.21), and (2.22). The thermophysical properties of air are evaluated at the film temperature, T_f.

$$h_{fc} = kNu_D/D \tag{2.18}$$

For a Smooth Cylinder ($k_s/D = 0.0$):

$$\text{(all } Re_D\text{)}: \quad Nu_D = 0.3 + 0.488Re_D^{0.5}\left(1.0 + \left(\frac{Re_D}{282000}\right)^{0.625}\right)^{0.5} \tag{2.19}$$

For $k_s/D = 75 \times 10^{-5}$:

$$\begin{array}{ll} \text{If } Re_D \leq 7.0 \times 10^5, & \text{use smooth cylinder correlation, Eq. (2.19),} \\ \text{If } 7.0 \times 10^5 < Re_D < 2.2 \times 10^7, & Nu_D = 2.57 \times 10^{-3} Re_D^{0.98}, \\ \text{If } Re_D \geq 2.2 \times 10^7, & Nu_D = 0.0455 Re_D^{0.81}. \end{array} \tag{2.20}$$

For $k_s/D = 300 \times 10^{-5}$**:**

$$\begin{aligned} &\text{If } Re_D \leq 1.8 \times 10^5, && \text{use smooth cylinder correlation, Eq. (2.19),} \\ &\text{If } 1.8 \times 10^5 < Re_D < 4.0 \times 10^6, && Nu_D = 0.0135 Re_D^{0.89}, \\ &\text{If } Re_D \geq 4.0 \times 10^6, && Nu_D = 0.0455 Re_D^{0.81}. \end{aligned} \tag{2.21}$$

For $k_s/D = 900 \times 10^{-5}$**:**

$$\begin{aligned} &\text{If } Re_D \leq 1.0 \times 10^5, && \text{use smooth cylinder correlation, Eq. (2.19),} \\ &\text{If } Re_D > 1.0 \times 10^5, && Nu_D = 0.0455 Re_D^{0.81}. \end{aligned} \tag{2.22}$$

The natural convection coefficient is influenced by the Nusselt and Grashof numbers based on the receiver height and by the ambient and tube wall temperature (2.23). Equation (2.24) is applicable for the analysis of pure turbulent natural convection heat transfer from cylindrical, external type receivers. To account for the effect of vertical ribs on natural convection, the smooth surface heat transfer coefficient h , will be modified by a factor of $\frac{\pi}{2}$ (2.25). This factor represents the ratio of the total rib surface area to the circumferential receiver area. The thermophysical properties of air are evaluated at the film temperature, T_∞.

$$h_{nc} = k Nu_L / L \tag{2.23}$$

$$Nu_L = 0.098 \cdot \mathrm{Gr}_L^{1/3} \left(\frac{T_w}{T_\infty} \right)^{-0.3} \tag{2.24}$$

$$h_{nc}(rough) = \left(\frac{\pi}{2} \right) h_{nc}(smooth) \tag{2.25}$$

Uhlig et al. 2016 investigated the influence of the ribbed surface of the receiver using three different CFD models. The study compared heat losses obtained from experimental data with both correlation-based results and simulated results for three selected test cases: a no-wind case, a low-wind case with 3.4 m/s wind speed (at receiver height), and a medium-wind case with 8.9 m/s wind speed (at receiver height). The CFD results showed good agreement with the correlation-based results; however, at high wind velocities, the CFD results indicated higher heat loss compared to the correlation-based predictions.

2.3.3 Radiation

Radiation is the energy emitted by matter as electromagnetic waves or photons due to changes in the electronic configurations of atoms or molecules. Unlike conduction and convection, radiation transfers energy without the need for a medium. The net rate of radiation heat transfer between matter and its surroundings is given by Equation (2.26) Çengel 2003.

$$\dot{Q}_{\text{Rad}} = \sigma \epsilon A_s (T_s^4 - T_{\text{amb}}^4) \tag{2.26}$$

Where:

σ	= Stefan's Boltzmann constant 5.67×10^{-8}	[W/(m^{2}K^4)]
ε	= Emissivity of the body	[-]
A_s	= Surface Area	[m^2]
T_s	= Surface Temperature	[K]
T_{amb}	= Ambient Temperature	[K]

Radiation heat transfer between surfaces depends on their relative orientation, radiative properties, and temperatures. The view factor, a geometric parameter independent of surface properties and temperature, quantifies the effect of orientation Çengel 2003. For two surfaces i and j with areas A_i and A_j, separated by a distance R and oriented at angles θ_i and θ_j, the view factor (F_{ij}) is given by:

$$F_{ij} = \frac{1}{A_i} \int_{A_i} \int_{A_j} \frac{\cos\theta_i \cos\theta_j}{\pi R^2} \, dA_i \, dA_j \tag{2.27}$$

The radiation losses between the surfaces can then be approximated analytically as:

$$\dot{Q}_{ij} = F_{ij} \sigma \epsilon_i A_i (T_i^4 - T_j^4) \tag{2.28}$$

Radiation heat transfer to or from a surface surrounded by a gas, such as air, occurs alongside convection. The total heat transfer is determined by combining the contributions of both mechanisms. For simplicity, this is often represented using a combined heat transfer coefficient, $h_{combined}$, which accounts for both convection and radiation. The total heat transfer rate is then expressed as 2.29: :

$$\dot{Q}_{\text{total}} = h_{combined} A_s (T_s - T_{amb}) \tag{2.29}$$

3 Thermo - Optical Model of the HPMS-II Receiver

The Thermo - Optical Model is developed to predict the temperature distribution within the molten salt at different locations of the receiver. To achieve this, a finite element method (FEM) interface, referred to as "Femray," is utilized. This interface incorporates ray-tracing to compute the solar radiation absorbed by the system. Given the high computational cost of using detailed CFD models to simulate the receiver, a simplified approach is adopted. This approach employs one-dimensional fluid flow elements to represent the movement of molten salt, allowing for efficient modeling of mass and heat transfer. The forced convective heat transfer between the absorber tubes and the molten salt is pre-calculated using the **Gnielinski correlation** and applied as a boundary condition for the absorber and connecting tubes Cathy Frantz and Busch 2022.

Finite Element Analysis was performed using the "Steady-State Thermal" and "Transient Thermal" modules in ANSYS software. Ray-tracing simulations were conducted in SPRAY software to determine the heat flux distribution on the receiver surface. The details of the modeling approach and boundary conditions applied in ANSYS are presented in the following sections.

Following the design of the receiver geometry, the geometry was discretized through meshing, and the resulting mesh file was used as input for SPRAY simulations. In SPRAY, heliostat aiming was configured to calculate the heat flux distribution across the receiver surface. The resulting heat flux data were subsequently imported into ANSYS Workbench as external input for further thermal analysis as illustrated in Figure 10.

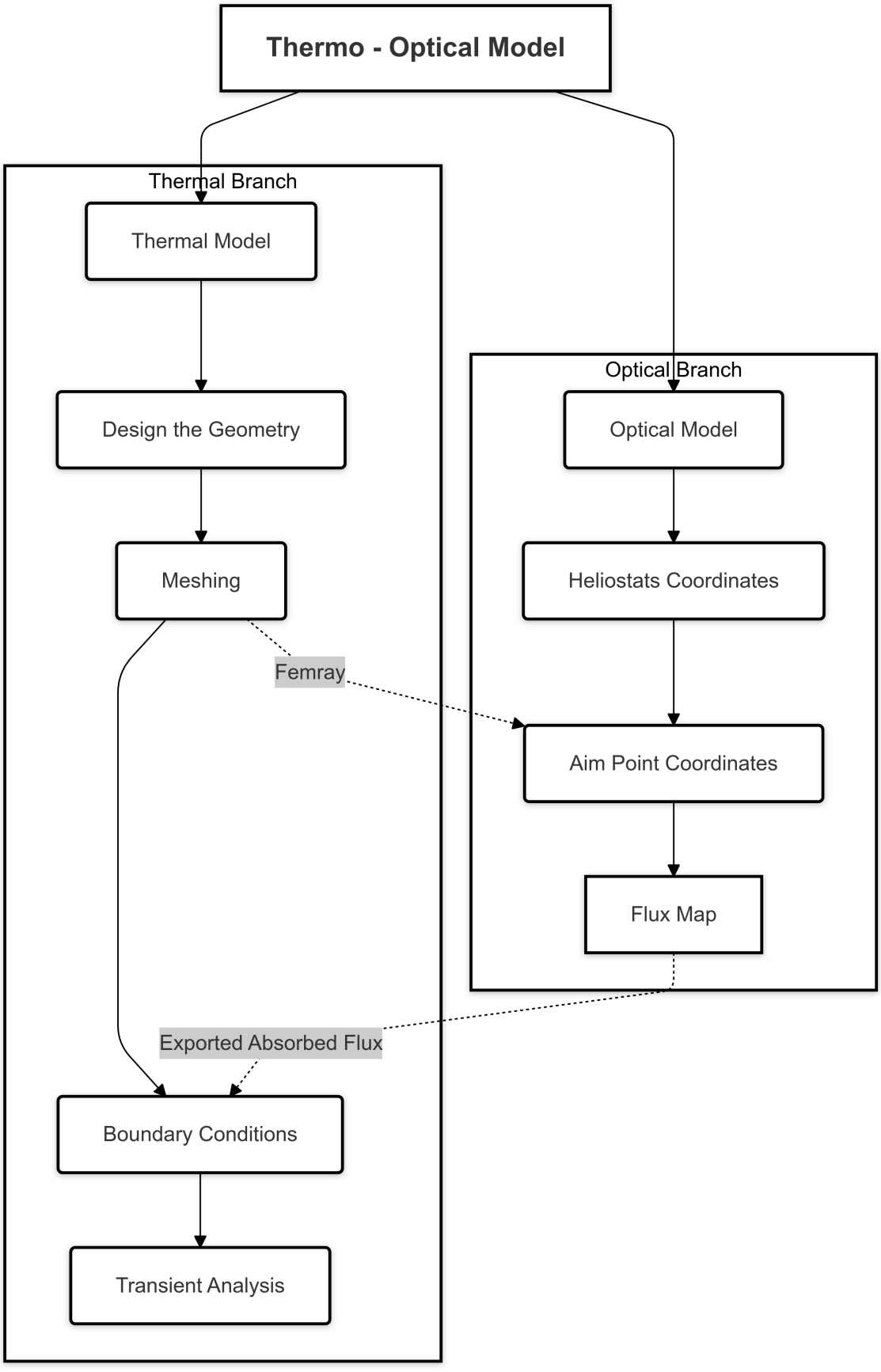

Figure 10: Thermo - Optical Flowchart.

3.1 Receiver Design

The receiver's thermal capacity for HPMS-II is set at 1 MW_{th}, with the maximum incident flux from heliostat field 1000 kW/m^2. This specification determines the available absorber surface area. In commercial receivers, the irradiated tube lengths are typically much greater than the hydrodynamic and thermal entrance lengths, thereby minimizing the impact of entrance length effects. To replicate forced convective heat transfer conditions comparable to those in commercial solar receivers, the irradiated absorber length was maximized in this study Frantz, Ebert, et al. 2023. To achieve low measurement uncertainty during solar operation, a configuration with $n_{par} = 2$ parallel tubes, each having an inner diameter of 32.8 mm, and 8 serial panels was implemented. The main design parameters are summarized in Table 3. Additionally, Figure 11 shows an illustration of the receiver along with the flow rate of molten salt.

Feature	**Value**
Thermal rating	1 MW
Maximum flux density	1000 kW/m^2
Tube outside diameter	36.8 mm
Tube wall thickness	2 mm
Irradiated tube length	2.5 m
Number of absorber tubes	16
Number of serial panels	8
Maximum salt temperature	600 °C

Table 3: Main Parameters of HPMS-II Test Receiver Layout.

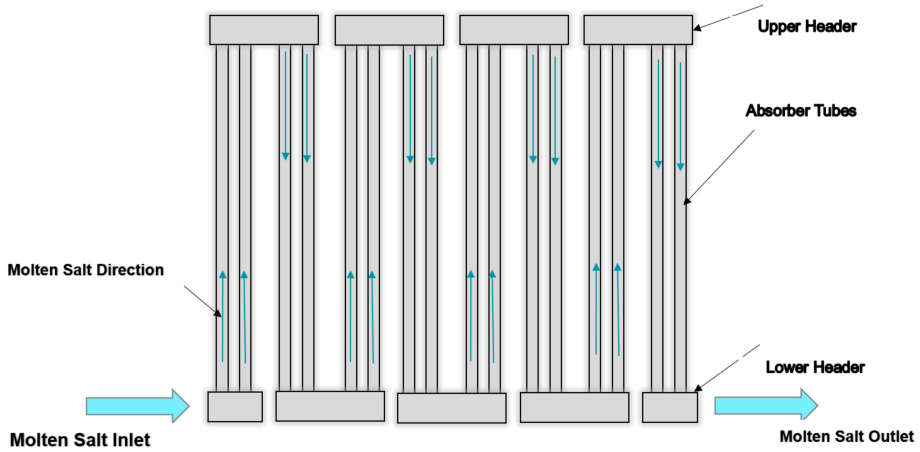

Figure 11: Schematic of the Molten Salt HPMS-II Receiver System.

The absorber tubes are fabricated from DMV 310N material and coated with Black Pyromark, a specialized paint renowned for its exceptional solar radiation absorption properties. For all other receiver components, 321H material is utilized due to its good availability. During solar operation, the system uses the standard nitrate solar salt, consisting of 60% $NaNO_3$ and 40% KNO_3 as the heat transfer fluid. The thermophysical properties of both the tube material and the molten salt vary with temperature, as detailed in Appendix A.

3.2 Operation Modes

HPMS-II operates under two modes: preheating operation and solar operation. During the preheating phase, the receiver is filled with synthetic air, while during the solar operation phase, it is filled with solar salt.

3.2.1 Preheating Mode

The preheating mode prepares the system by preventing the solidification of molten salt, which has a high solidification temperature (240°C). Solidification can lead to blockages, mechanical damage, and thermal stresses. In this process, absorber tubes are preheated using solar energy reflected by heliostats, while the upper and lower headers and connecting tubes within the insulation shield are heated using heat tracing, as shown in Figures 12 and 13.

To avoid overflux on the receiver, the predicted flux distribution must be calculated accurately, and the optimal number of heliostats determined BRADSHAW 2002. The heliostats were aligned toward the vertical centerline of the receiver at varying elevations, ensuring an even flux distribution across its surface. When the absorber tubes reach 350°C, the receiver is ready for filling with molten salt, initiating the solar operation mode.

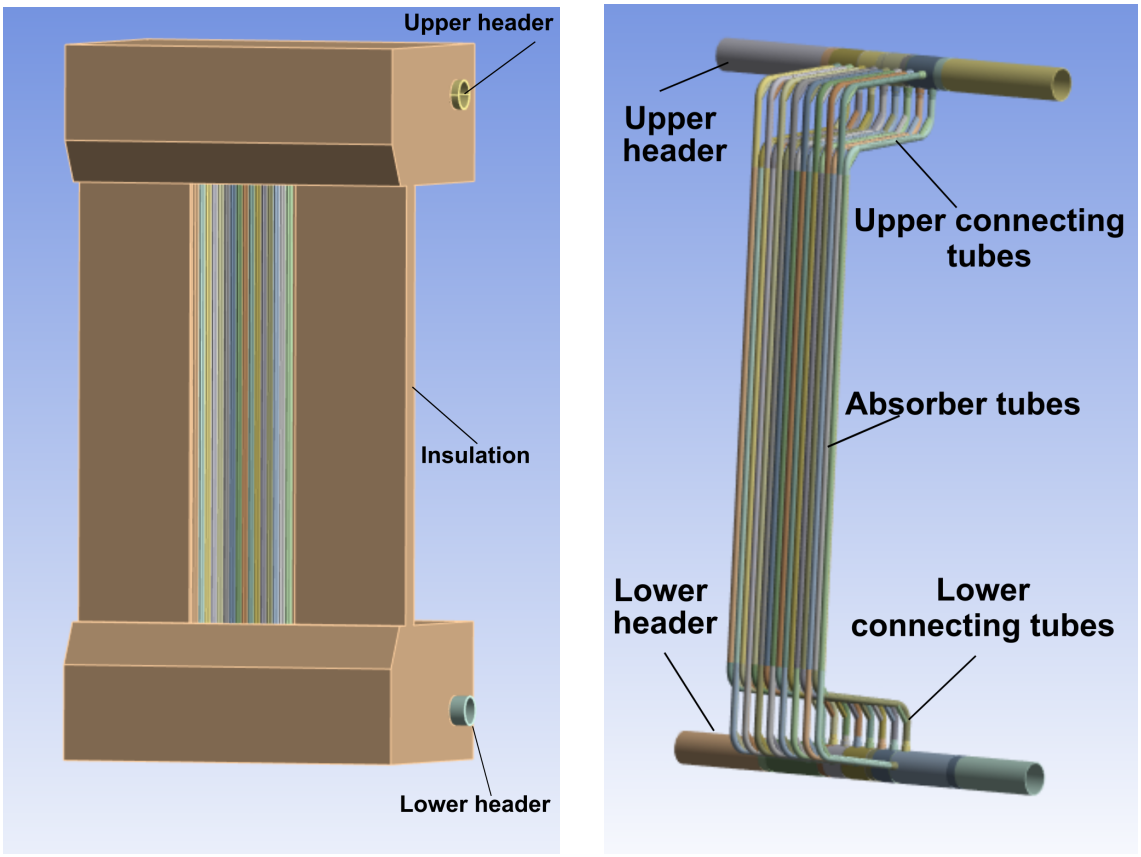

(a) Receiver with Insulation. **(b)** Receiver without Insulation.

Figure 12: Receiver Model.

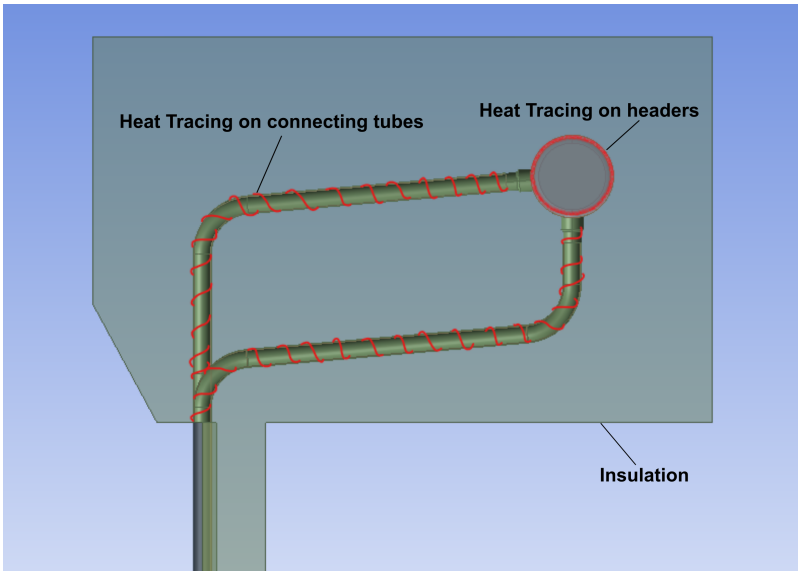

Figure 13: Sketch of the Heat Tracing System.

3.2.2 Solar Operation Mode

The solar operation mode utilizes solar energy as a thermal energy source for heat transfer and power generation. Solar radiation is concentrated onto absorber tubes by heliostats, with molten salt as the heat transfer medium. This mode enables efficient thermal energy collection and storage for subsequent power generation.

3.3 Case Studies: Problem Definition

Two operational modes were analyzed: preheating and solar operation. In the preheating mode, a transient approach was adopted over a duration of 20 minutes, with a gradual increase in solar flux to evaluate the receiver's performance. For the solar operation mode, steady-state conditions were examined to evaluate the effects of mass flow rate, solar flux distribution, and wind velocity on the receiver. The results for both modes were validated using experimental measurements obtained on 19 August 2024. To assess the system's performance, four distinct cases were analyzed by varying the molten salt's mass flow rate ($\dot{m}$) and incident flux, as summarized in Table 4.

Operation	**Pre Heating**	Solar		
		Callibration	**Partial Load**	**Full Load**
Avg.Wind velocity, v [m/s]	0.6	1.9	2.9	1.5
Time	9:50 - 10:10	11:00	11:41	15:51
Simulation Model	Transient	Steady State	Steady State	Steady State
Heat Transfer Fluid	Air	Molten Salt		
Mass Flow Rate per Panel, $\dot{m}$ [kg/s]	-	4.1	4	11.5
Number of Heliostat	90 - 160	-	630	839
Total Power on Absorbed Tubes [kW]	13.58 - 32.42	-	361.10	370.25
Salt Inlet Temperature [°C]	-	350.53	356.855	585.90
Ambient_1 Temperature [°C]	19.75	21	21.41	24.22
Average Rear Side Temperature [°C]	252.2	350	385	598
Ambient_2 Temperature [°C]	123.74	175.2	192	299

Table 4: Summary of Case Studies for Preheating and Solar Operating Scenarios.

3.4 Thermal Boundary Conditions

The heat loss from the outer surface of the receiver to the surrounding environment is characterized by convection and radiation losses on both sides of the tubes. On the front side, where the absorber tube is exposed to solar radiation, and on the rear side, which is not directly exposed to irradiance, temperature gradients develop. Additionally, heat transfer to the HTF occurs through convection. The boundary conditions are illustrated in Figure 14.

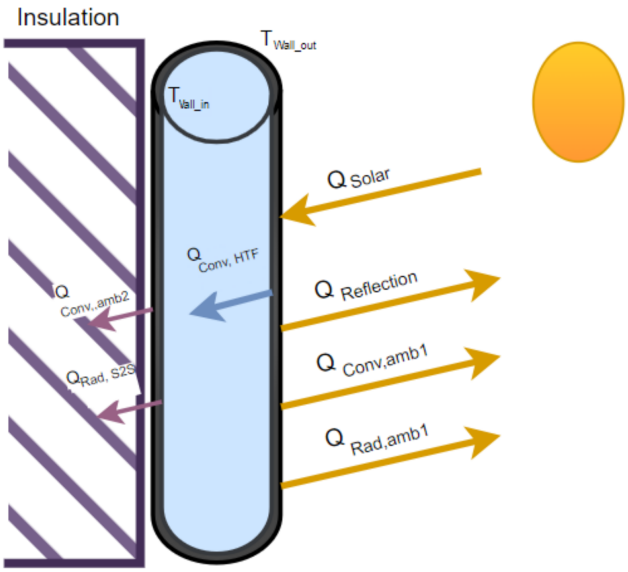

Figure 14: Illustration of Boundary Conditions.

3.4.1 Convection Losses

Convection to Ambient1

As illustrated in Figure 14, the convection losses from the front-side tube surface to the surrounding environment were estimated by analyzing both forced and natural convection mechanisms. In the absence of explicit data for the front-side tube surface temperature, the convective heat transfer coefficient (HTC) was expressed as a function of the outer wall temperature, T_w, using Equation 2.17. Forced and natural convection were evaluated using a smooth cylinder model, as defined by

Equations 2.19 and 2.24, respectively. Wind speed values were obtained from measurement data.

Forced convection was analyzed only for the front side of the receiver, as the rear side is shielded by the irradiation shield. The narrow 1 mm gap between the rear side and the irradiation shield prevents significant airflow, rendering forced convection negligible on the rear-side. Consequently, only natural convection was considered in this region. To account for forced convection on the front-side, which depends on the Reynolds number, as illustrated in Equation 2.19, the receiver diameter was simplified and assumed equal to the receiver width (0.6 m).

The average ambient temperature during the experimental day was 20°C. While wind speeds is varies during and can reach up to 20 m/s during winter, the measured wind speeds on the experimental day during preheating were significantly lower, averaging 0.6 m/s between 09:50 and 10:10. During solar operation, the wind speeds averaged 1.9 m/s at 11:00, 2.9 m/s at 11:41, and 1.5 m/s at 15:51. These measurements were recorded by a ground-level wind station located within the heliostat field.

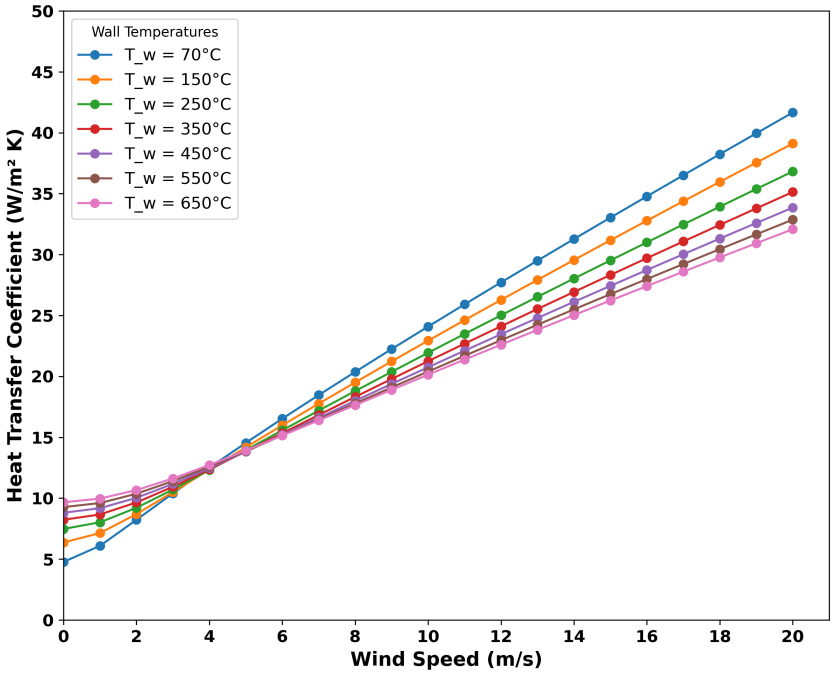

Figure 15: Convective Heat Transfer Coefficient vs. Wind Speed for Different Wall Temperatures.

Figure 15 illustrates the variation in HTC with respect to different wind speeds and wall temperatures. The HTC increases with the wall temperature, T_w, for wind velocities below 4 m/s. In this regime, natural convection dominates, leading to an increase in the Grashof number (Gr) as T_w rises. For wind velocities exceeding 4 m/s, the HTC decreases as T_w increases. This behavior occurs because forced convection becomes dominant, and the variable property effects associated with forced convection influence the heat transfer characteristics.

In the HPMS-II system, the absorber tubes are enclosed within the tower, which significantly reduces wind speed. A consequently, heat losses are primarily governed by natural convection. To evaluate the impact of this configuration, the wind speed at the receiver was approximated based on the average measured wind speed. During solar operation, the HTC was estimated to range from 7 W/m^2·K at 70 °C to 11.5 W/m^2·K at 690 °C. During preheating operation, the HTC was estimated to range from 5.4 W/m^2·K at 70 °C to 10 W/m^2·K at 690 °C, due to changing in weather conditions as illustrated in Figure 16.

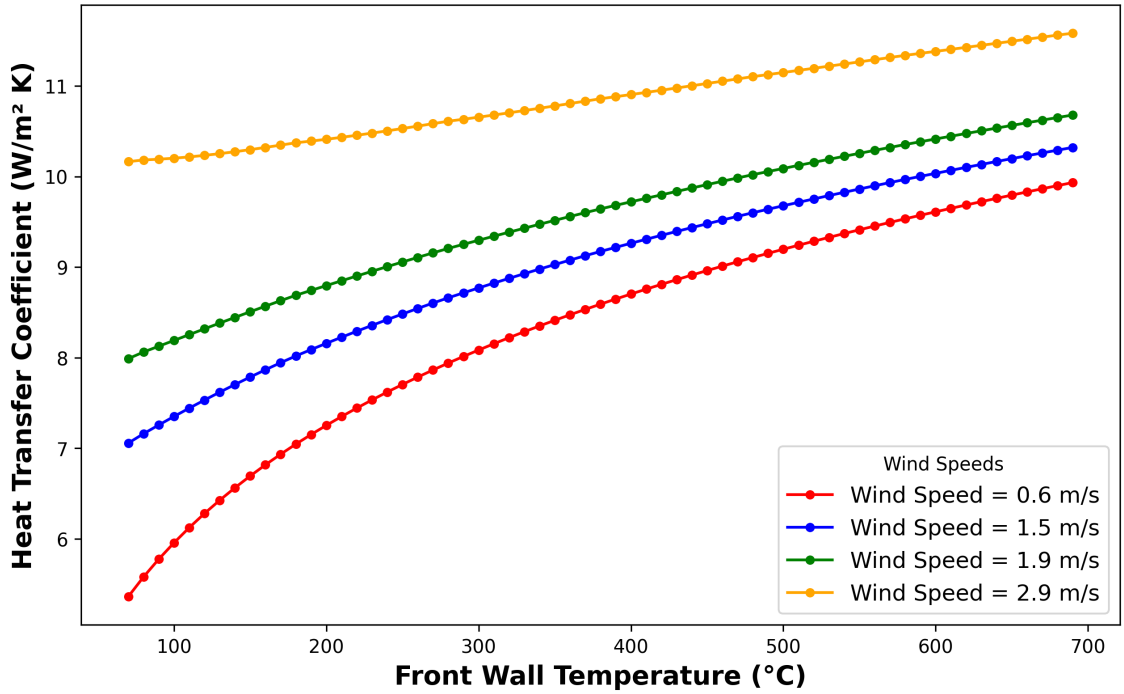

Figure 16: Convective Heat Transfer Coefficient vs. Front Wall Temperature for Average Wind Speed During Experimental Day.

Convection to Ambient2

As illustrated in Figure 14, the rear side of the tube is subject only to natural convection, as described by Equations 2.24 and 2.23. Due to the absence of air temperature measurements in the gap between the rear side of the tube and the insulation shield, the ambient2 temperature was assumed to be a function of the average rear side temperature. This assumption is based on thermocouple measurements obtained from the rear side of the tube, as shown in Figure 17.

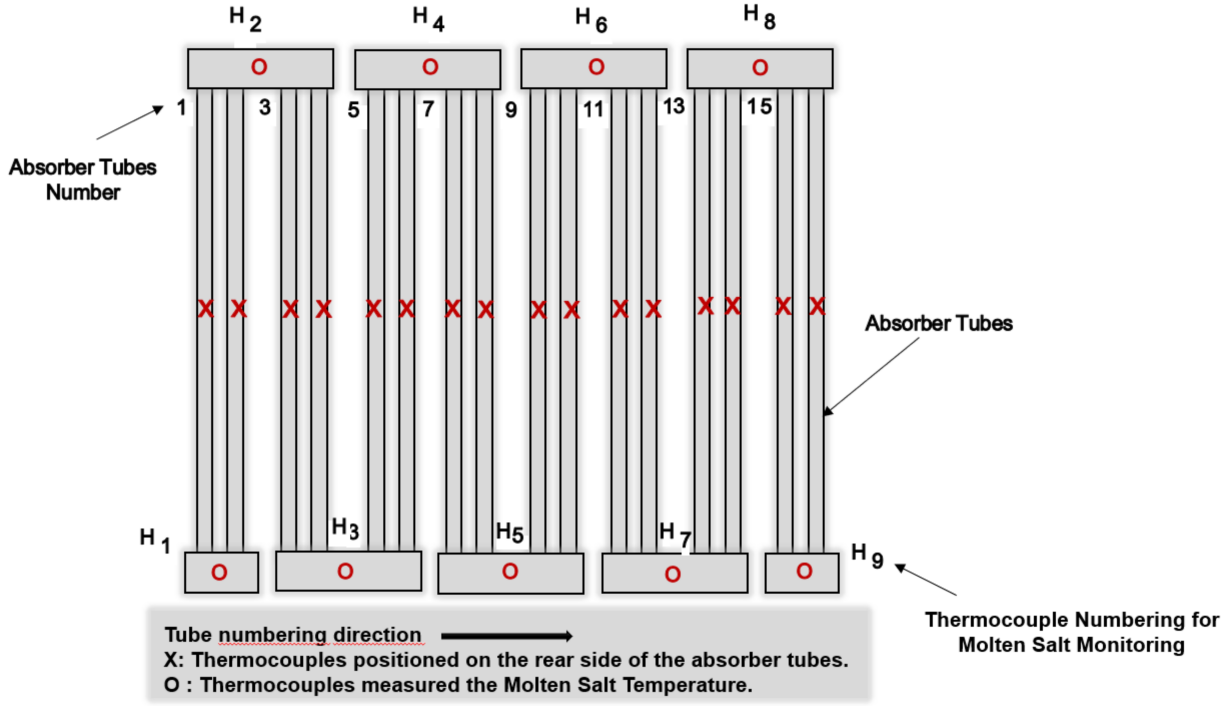

Figure 17: Thermocouple Layout on the Rear Side of the Absorber Tubes.

Optimization Process for Ambient2

During preheating operation, where the simulation is transient, the ambient2 significantly influences convection losses. To ensure accuracy, an optimization process was conducted for various values of ambient2, ranging between 20% and 80% of the average rear side temperature. The process minimized the mean square error (MSE) between simulated and measured data, as detailed in Preheating Operation Scenario. The results indicate that ambient2 values near 50% of the average rear-side temperature yielded the lowest error. In contrast, during the solar operation,

where the simulation is in a steady state, variations in ambient2 showed negligible impact on results. Consequently, the same value (50% of the average rear side temperature) was adopted for the solar operation as well.

The HTC during preheating and solar operation depends on the rear side temperature, as illustrated in Figures 18, 19 and 20. It can be observed that lower ambient2 temperatures are associated with higher HTC values, as highlighted in Figures 18, 19, and 20. These figures compare HTC values at a consistent wall temperature of 350 °C for different ambient2 temperatures, as detailed in Table 4.

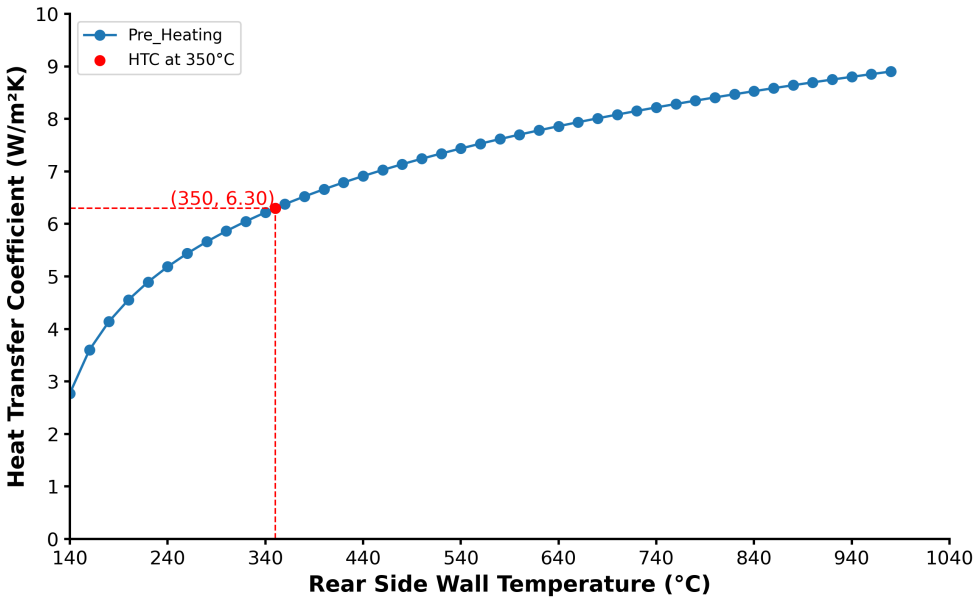

Figure 18: Convective Heat Transfer Coefficient vs. Rear-Side Wall Temperature During Preheating Operation.

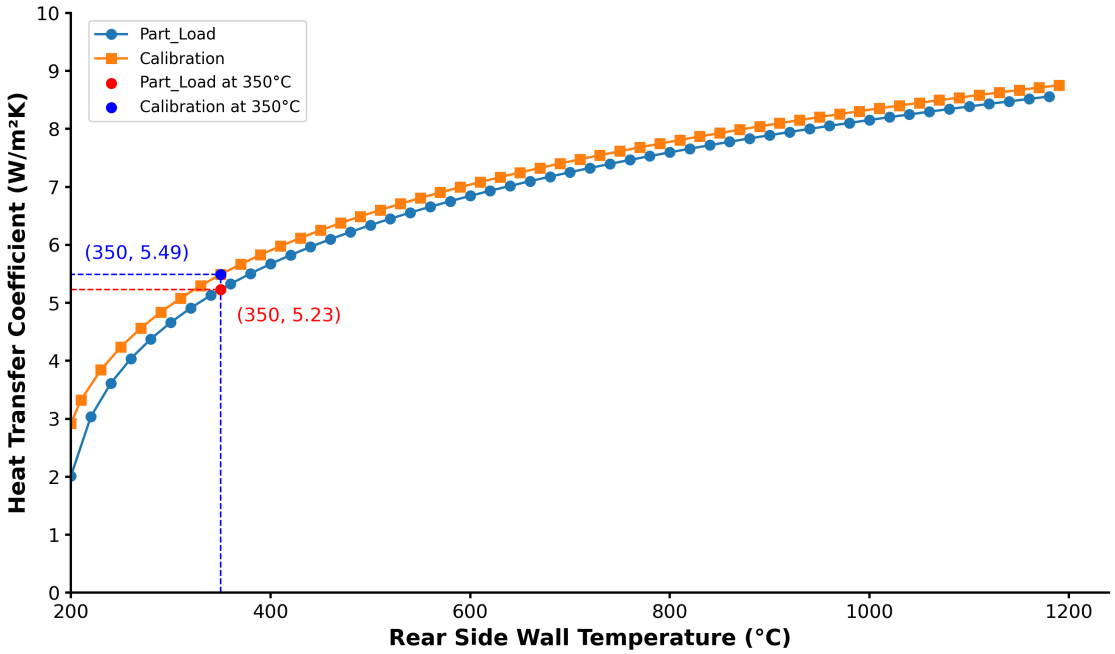

Figure 19: Convective Heat Transfer Coefficient vs. Rear-Side Wall Temperature During Calibration and Partial Load Solar Operation.

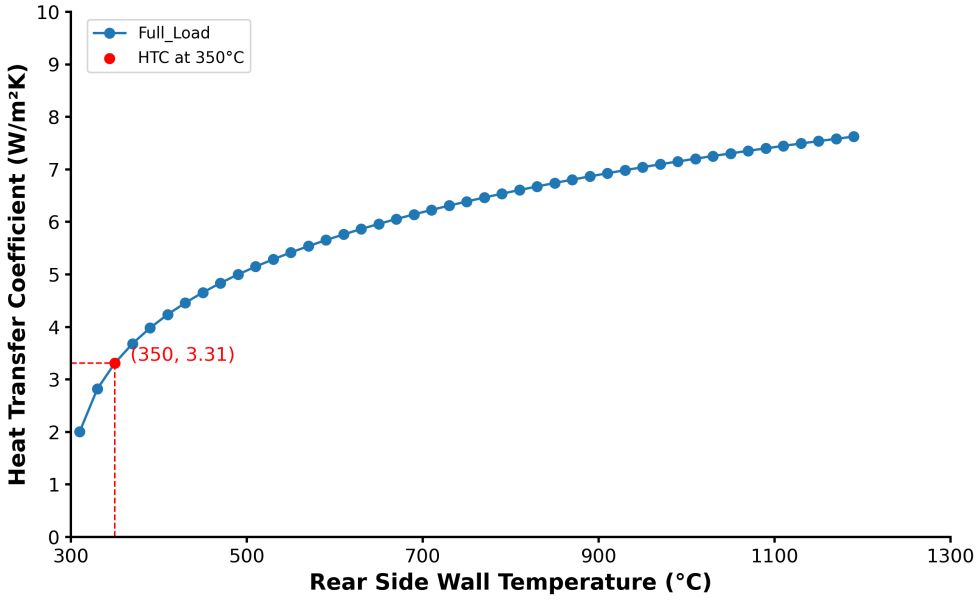

Figure 20: Convective Heat Transfer Coefficient vs. Rear-Side Wall Temperature During Full Load Solar Operation.

Convection within the Absorber Tubes

The HTF within the absorber tube varies based on the operational mode. During preheating, the tubes are filled with air, whereas during solar operation, they are filled with molten salt. This variation significantly influences the convection regime and, consequently, the HTC.

Preheating Operation

The correlation for Natural Convection in Enclosed Spaces was initially considered for preheating but deemed unsuitable for this case due to the non-uniform flux distribution, which leads to uneven temperature distributions across the tube surfaces, as illustrated in Figure 21. To address this limitation, a CFD model was developed to determine the HTC within the pipes, as existing correlations and experimental studies do not adequately account for this scenario.

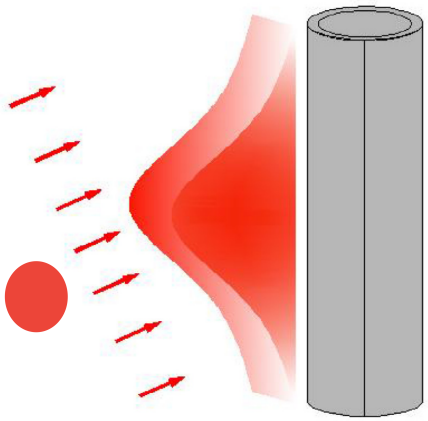

Figure 21: Illustration of Flux Distribution on the Absorber Tube.

To simplify the simulation, only a middle pipe of the absorber tubes was modeled. The CFD model setup is designed for single-phase flow within the selected geometry, with fine meshing applied near the edges to enhance accuracy in capturing temperature gradients. The Boussinesq approximation is employed to model buoyancy-driven flow, incorporating gravitational acceleration in the z-direction. Steady-state simulations were conducted, solving the energy equation, a laminar flow model, and surface-to-surface radiation. The convergence criteria were based on root mean square (RMS) residuals for momentum, energy, and mass continuity

equations. To ensure numerical accuracy and stability, the High-Resolution scheme was employed for discretizing advection terms.

Boundary conditions are determined by applying a constant temperature to the edges of the selected tube. The incident flux distribution is incorporated as an energy source. Convection and radiative losses were computed analytically, as detailed in Appendix B.

Validation of the simulation was challenging due to the limited availability of correlations and experimental measurements. Consequently, simulations were performed for three case studies at discrete time steps: 10:00, 10:06, and 10:10. At 10:10, the maximum flux distribution on the front-side of the absorber tube is $3.498 \times 10^3\,\mathrm{W/m^2}$, as illustrated in Figure 22. This results in a non-uniform temperature distribution, as shown in Figure 23. The variations in flux distribution induced differences in buoyancy forces, which increased with rising temperatures and decreased as temperatures declined. These effects are depicted in Figure 24, illustrating the transition from regions of higher to lower temperature.

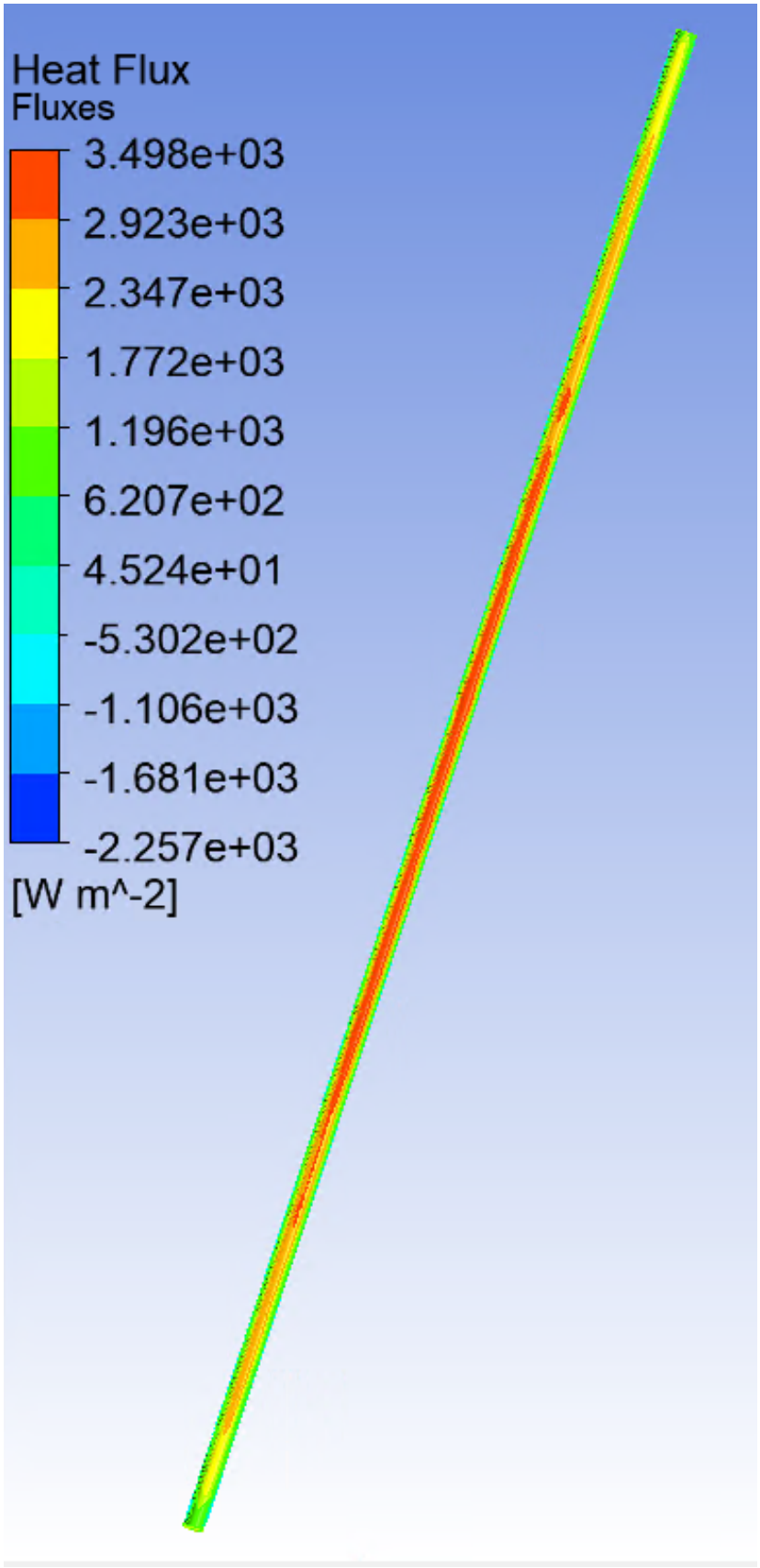

Figure 22: Flux Distribution on the Front Side of the Absorber Tube During Preheating at 10:10.

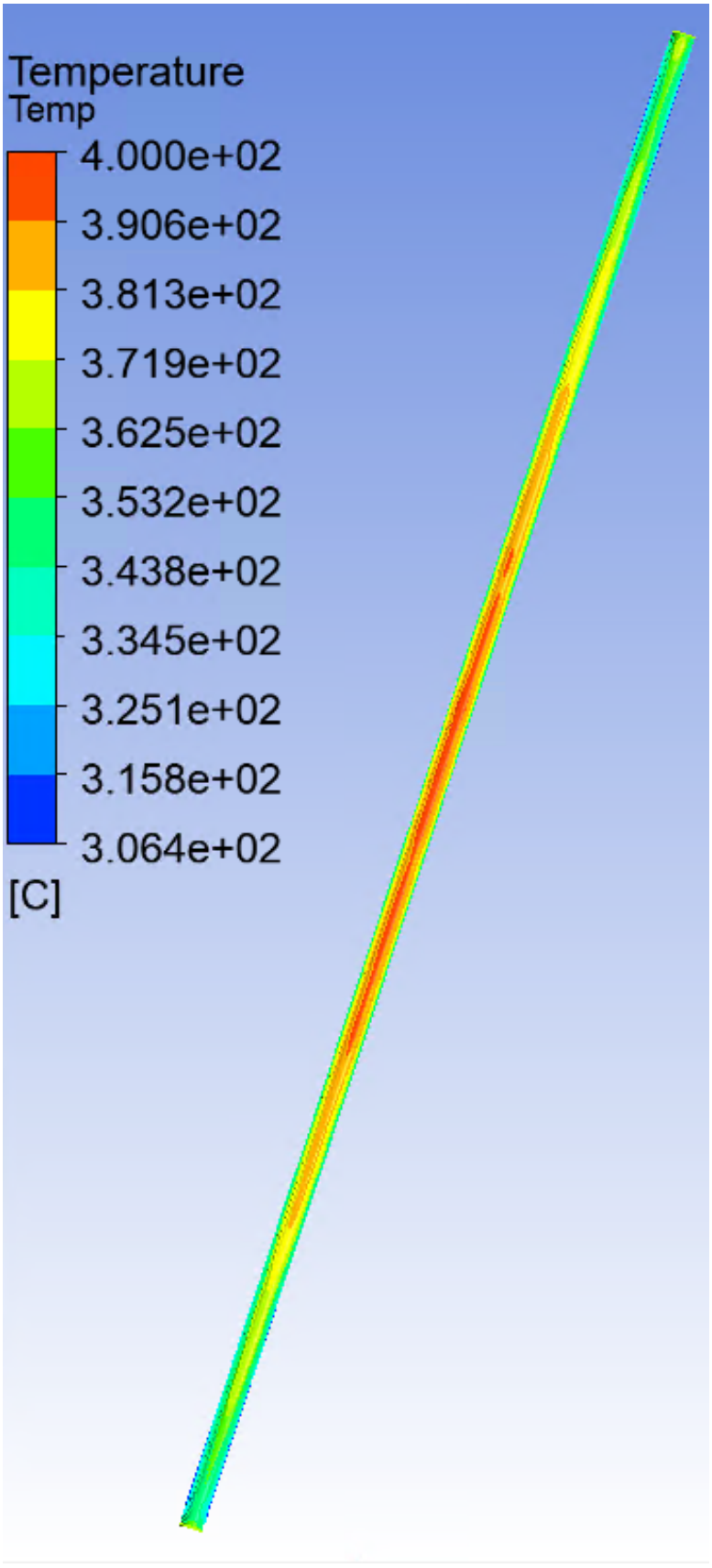

Figure 23: Temperature Distribution on the Front Side of the Absorber Tube During Preheating at 10:10.

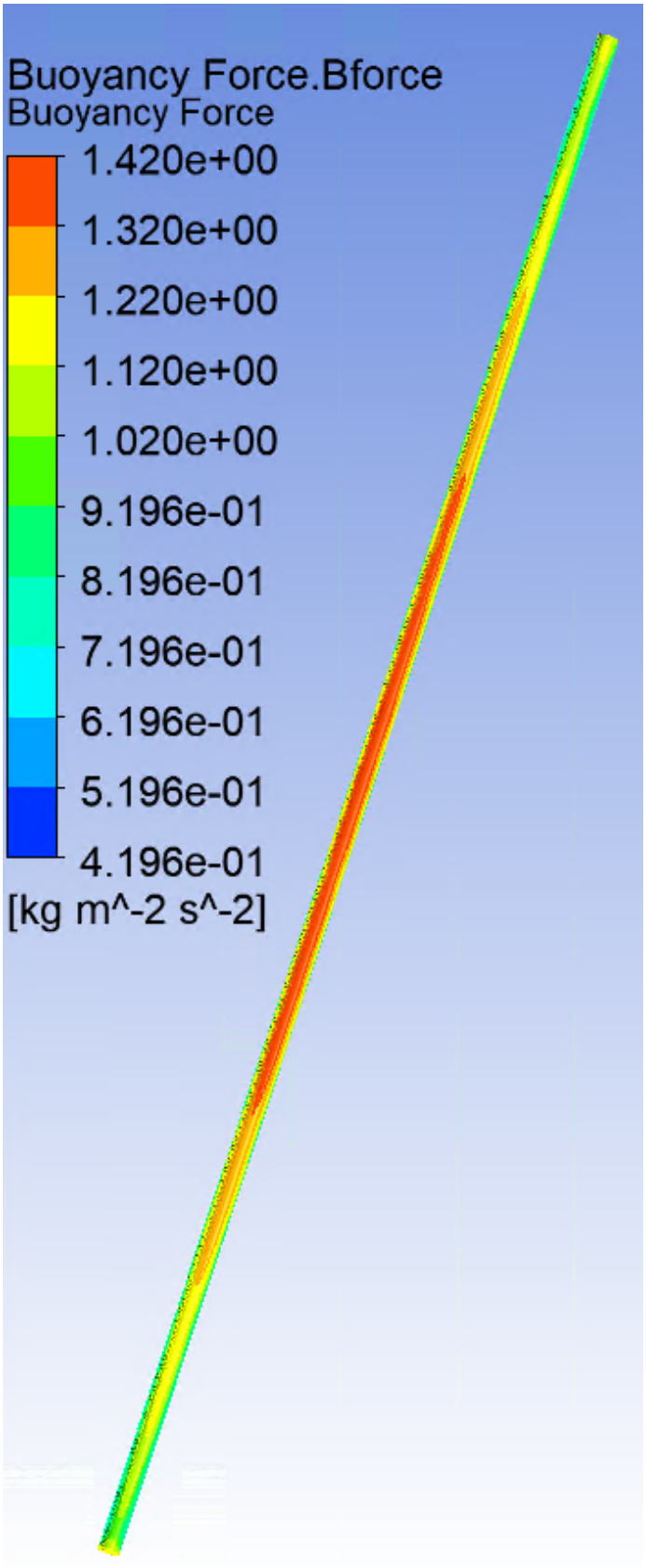

Figure 24: Buoyancy Force Distribution on the Front Side of the Absorber Tube During Preheating at 10:10.

The temperature distribution of air in the ZX plane is illustrated in Figure 25. To validate the model, the simulated temperature at the center of the rear side of the selected absorber tube was compared with measurements. This comparison resulted in a relative error of 2.51 %. The simulated temperature was 314.826°C, while the measured temperature was 322.942°C.

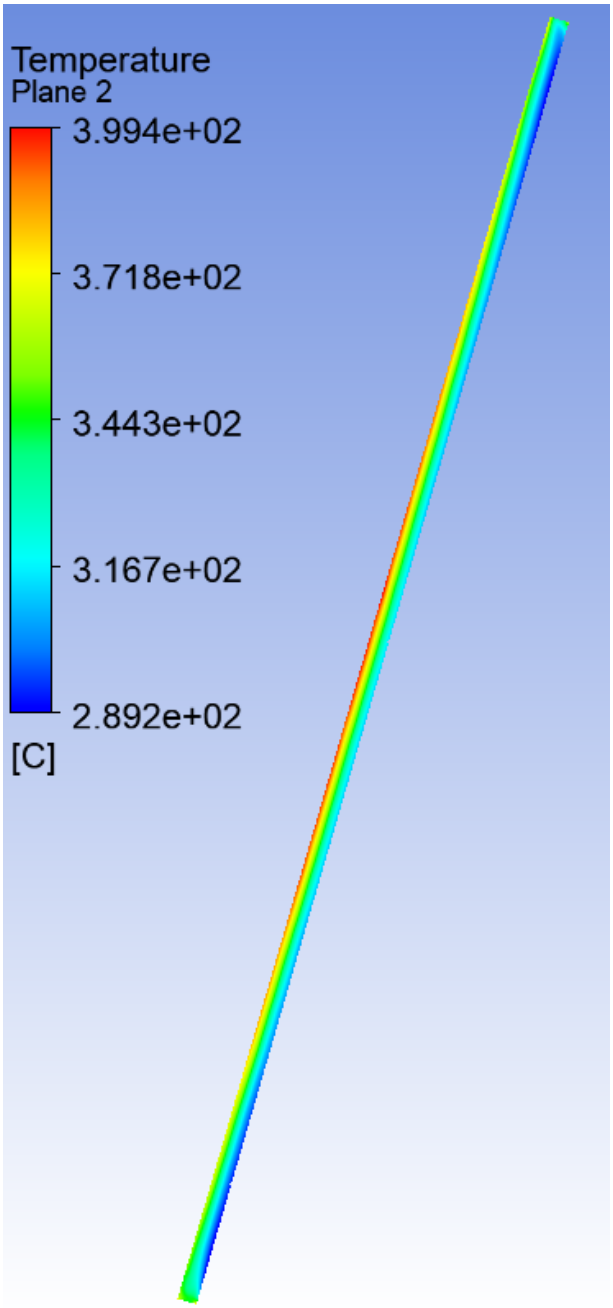

Figure 25: Temperature Distribution in the ZX Plane During Preheating at 10:10.

To calculate the wall HTC within the tube, its variation along the Z-axis is illustrated in Figure 26. As described in Table 3, the length of the absorber tube is 2.5 meters. However, the mean wall HTC along the Z-axis is calculated over a length of 1.5 meters only. This is due to the constant temperature and lower incident fluxes near the edges compared to the highest fluxes at the center, which lead to uncommon behavior in the results within 0.5 meters from each end. The average wall HTC at 10:10 is calculated as 4.09 W/m^2K at average air temperature 336.169°C. Detailed results for other time steps are provided in **Appendix B**. The average wall HTC used in the thermal simulations for all three time steps is 4.44 W/m^2K.

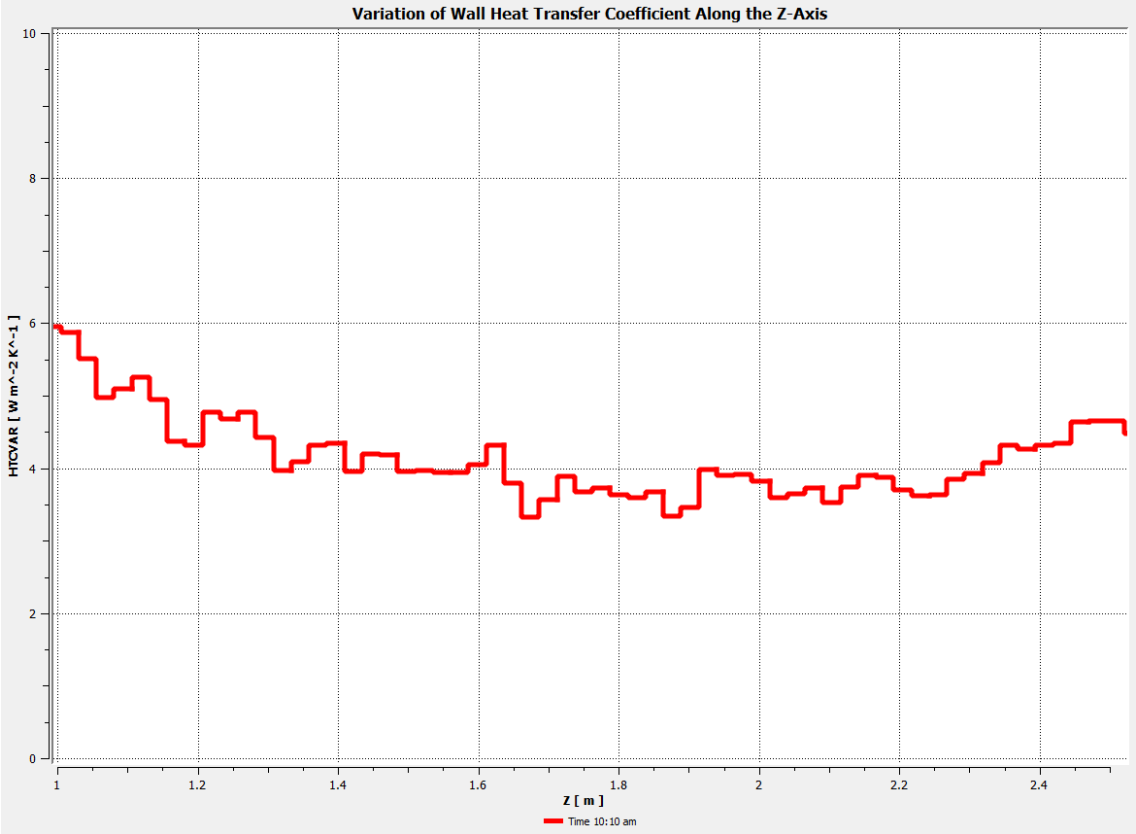

Figure 26: Wall Heat Transfer Coefficient Variation along the Z-Axis During Preheating at 10:10.

Solar Operation

In solar operations, the convection within the tubes is classified as forced convection. The Reynolds number for the three case studies was calculated, and the results confirm that the flow inside the tubes is turbulent. Consequently, several correlations can be used to analyze turbulent flow. Experimental studies conducted at DLR have shown that the Gnielinski correlation provides good agreement with experimental data Frantz, Buck, et al. 2023. Therefore, the Gnielinski correlation has been applied to calculate the HTC, as presented in Equation 2.5. Since the tube thickness is only 2 mm, it is assumed that the inner wall temperature is equal to the outer wall temperature. The fluid properties of molten salt were determined at the inlet temperature of the molten salt, and the HTC was subsequently calculated as a function of the wall surface temperature, as illustrated in Figure 27.The mean forced convective heat transfer in the headers, as illustrated in Figure 28, is modeled using heat transfer coefficients derived from CFD simulations as function of salt temperature and salt mass flow rate Cathy Frantz and Busch 2022.

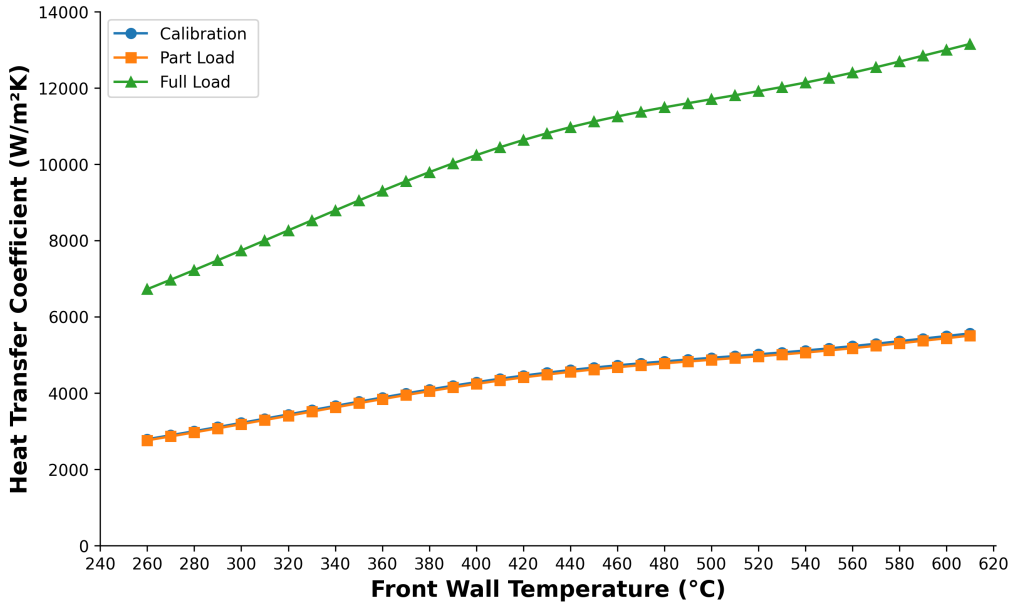

Figure 27: Molten Salt Convective Heat Transfer Coefficients in the Absorber Tube.

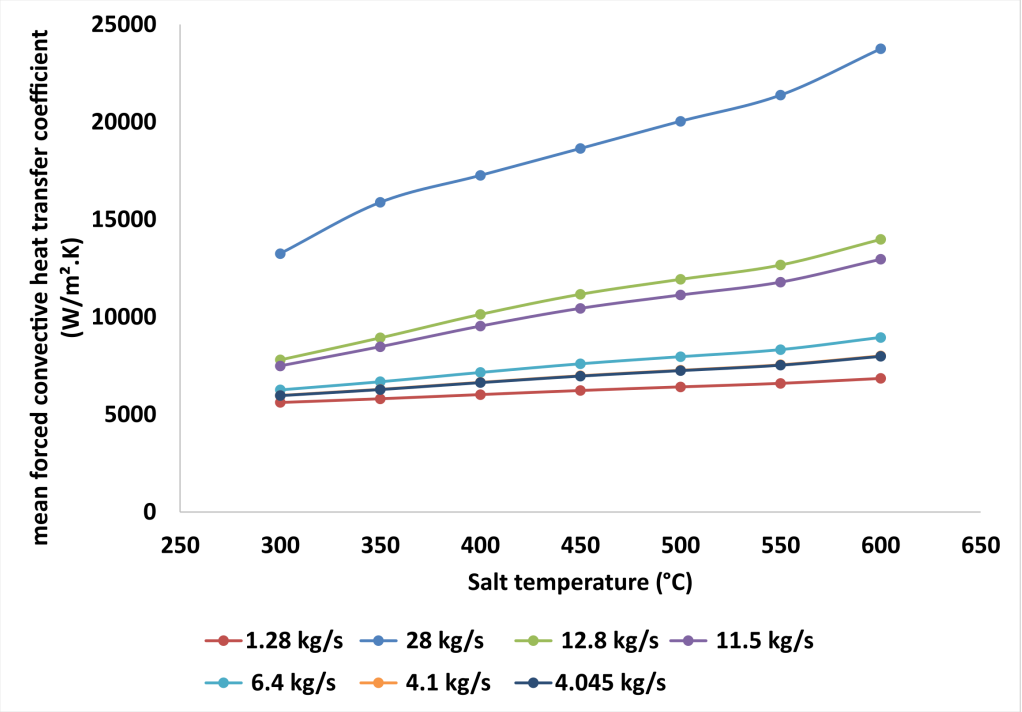

Figure 28: Molten Salt Convective Heat Transfer Coefficients in the Header.

3.4.2 Radiation Losses

Pyromark 2500

According to Ho, Mahoney, et al. 2013 , presents the hemispherical emissivity of Pyromark 2500 as a function of temperature, measured at 26 °C and 600 °C, as illustrated in Figure 29. For calculations, the conservative emissivity value of 0.8 at 600 °C is assumed as illustrated in Table 5 .

Property	Value
Solar-weighted hemispherical absorptivity of the absorber tube (Pyromark)	0.90
Hemispherical emissivity of the absorber tube	0.8

Table 5: Optical Properties of the Absorber Tube.

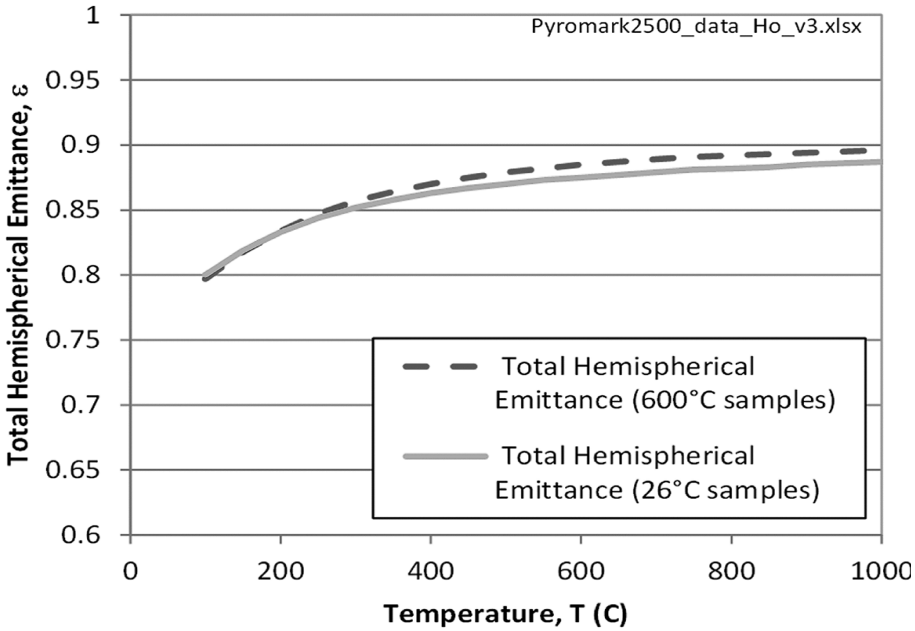

Figure 29: Total Hemispherical Emittance as a Function of Temperature for Pyromark 2500 Ho, Mahoney, et al. 2013.

Optical Properties of Radiation Shielding

The measurements of reflectivity and emissivity of the radiation shielding were conducted in the quartz laboratory at DLR Cologne, revealing a solar-weighted hemispherical reflectivity of 77.7%. The measurements also determined a solar-weighted hemispherical emissivity of 76.4%.

Property	**Value**
Solar-weighted hemispherical absorptivity of the radiation shielding	0.223
Hemispherical emissivity of the insulation	0.764

Table 6: Optical properties of the Radiation Shielding and Insulation.

4 Quality control

The primary objective of model validation is to achieve a mesh-independent solution. This is accomplished by systematically varying the element sizes in both the circumferential and axial directions for absorber tubes, headers, and insulation, as detailed in **Appendix C**. The model uses hexahedral and prism elements to ensure accurate geometric representation and solution convergence.

Two models were developed for validation: a computational fluid dynamics (CFD) model and a thermal model. In the CFD model, the rear side temperature of a selected middle tube, along with heat transfer, momentum, and mass, were monitored to ensure convergence below the specified threshold and to evaluate mesh resolution adequacy. For the thermal model, three key parameters were assessed: the outlet molten salt temperature, the rear side temperature of a selected middle tube (Tube7), and the molten salt temperature T_{Salt} in a selected header (Header4), as illustrated in Figure 17.

4.1 CFD Model

Nine mesh configurations with varying grid refinements were developed for the CFD model, as described in **Appendix C**. The results are summarized in Table 7. Convergence for the rear side temperature of the middle absorber tube was observed starting at Set6 (Figure 30). To balance computational efficiency and accuracy, Set7 was selected as the final mesh configuration.

Mesh	No. of Nodes	No. of Elements	Rare Side Temperature of Middle Absorber Tube7 (°C)	Computational Time [min]
Set1	70,523	135,610	290.922	3
Set2	102,547	186,184	291.032	4
Set3	152,711	297,894	291.157	7
Set4	230,674	435,964	288.943	8
Set5	324,682	619,567	289.842	13
Set6	373,959	676,370	290.299	14
Set7	384,846	699,212	290.331	15
Set8	429,403	795,820	290.292	21
Set9	499,823	940,662	290.295	27

Table 7: Mesh Refinement and Temperature Results for CFD Model.

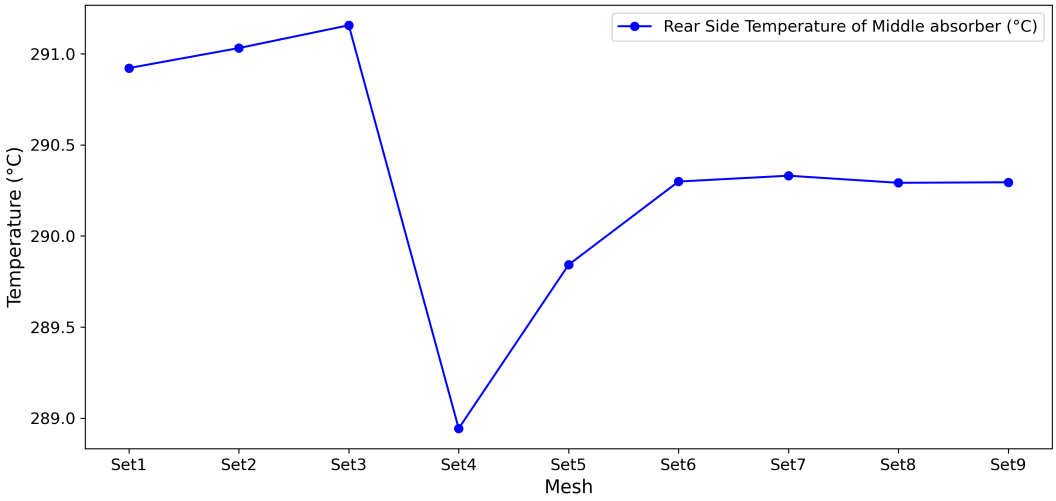

Figure 30: Rear Side Temperature of the Absorber Tube for Different Mesh Sizes in CFD Model.

4.2 Thermal Model

Eight mesh configurations with varying grid refinements were developed for the thermal model, as detailed in **Appendix C**. The results are presented in Table 8. Convergence for the outlet molten salt temperature was achieved at Set5 as illustrated in Figure 31, while convergence for the molten salt temperature at Header4 and the rear side temperature of Tube7 occurred at Set4 as illustrated in Figures 32 and 31. Based on these results, Set6 was selected as the final configuration to ensure a balance between computational cost and accuracy.

Mesh	**No. of Nodes**	**No. of Elements**	**Outlet Molten Salt Temperature (°C)**	**Rare Side Temperature of Middle Absorber $Tube_7$ (°C)**	**Molten Salt Temperature Located in $Header_4$ (°C)**	**Computational Time**
Set1	85,607	49,207	410.37	382.79	376.61	2 min
Set2	583,691	138,908	408.14	379.17	376.01	4 min
Set3	912,922	230,481	407.17	378.23	375.35	7 min 30 s
Set4	1,342,805	418,618	407.06	378.11	375.40	10 min
Set5	1,626,592	512,773	407.23	378.07	375.38	15 min
Set6	2,147,111	772,623	407.29	378.10	375.42	25 min
Set7	2,424,734	872,776	407.20	378.09	375.40	35 min
Set8	2,482,398	905,074	407.15	378.07	375.38	1 h 10 min

Table 8: Mesh Refinement and Temperature Results for Thermal Model.

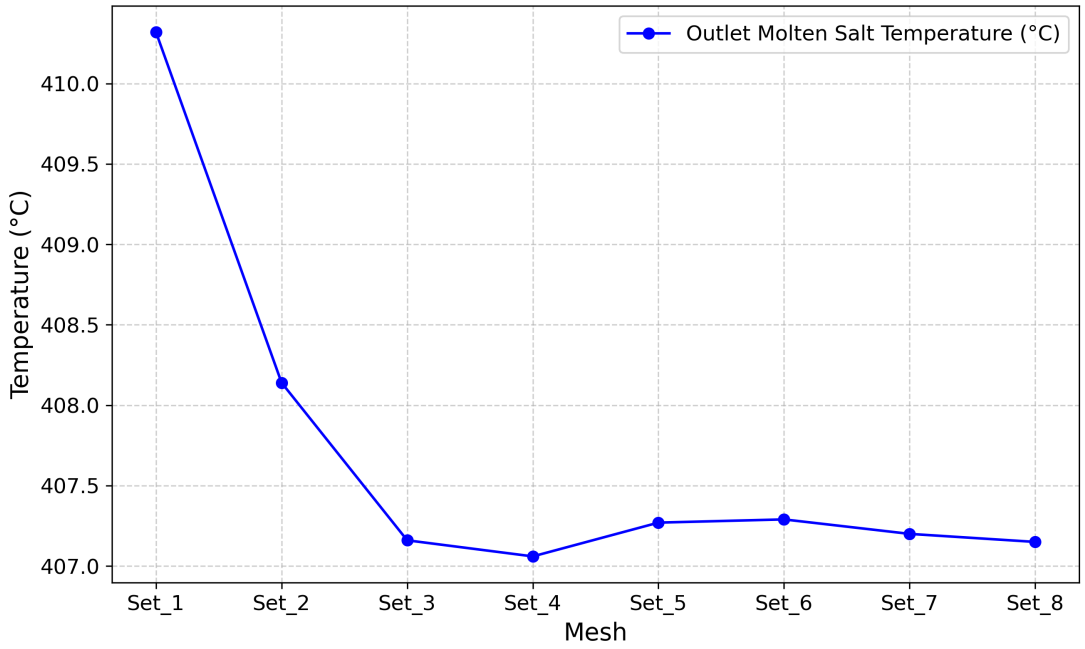

Figure 31: Outlet Molten Salt Temperature for Different Mesh Sizes in Thermal Model.

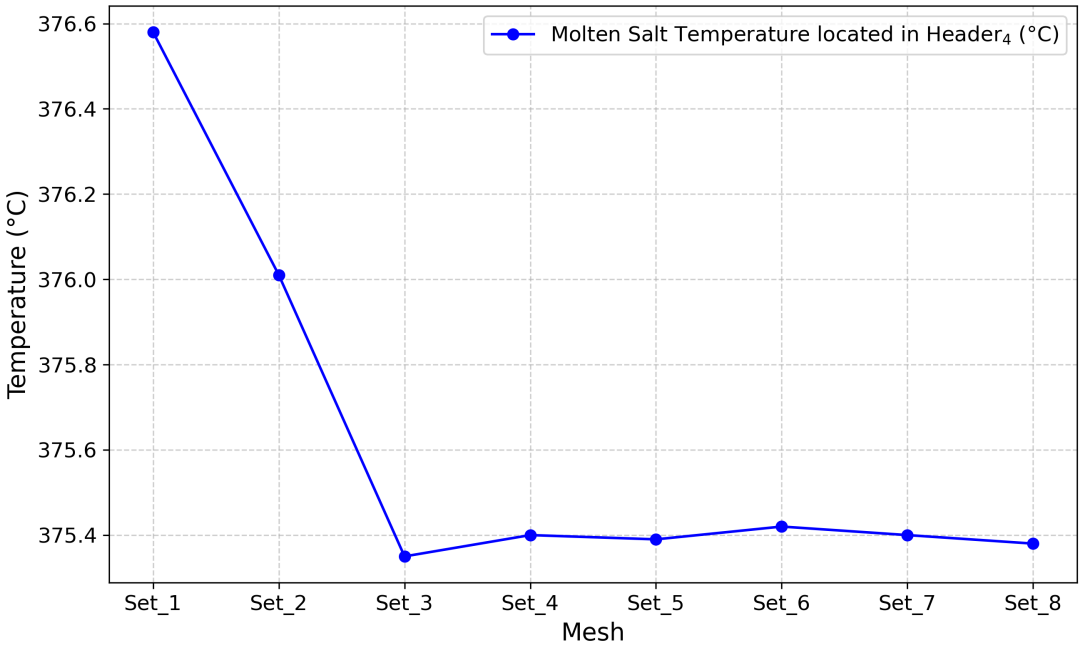

Figure 32: Molten Salt Temperature at Header4 for Different Mesh Sizes in the Thermal Model.

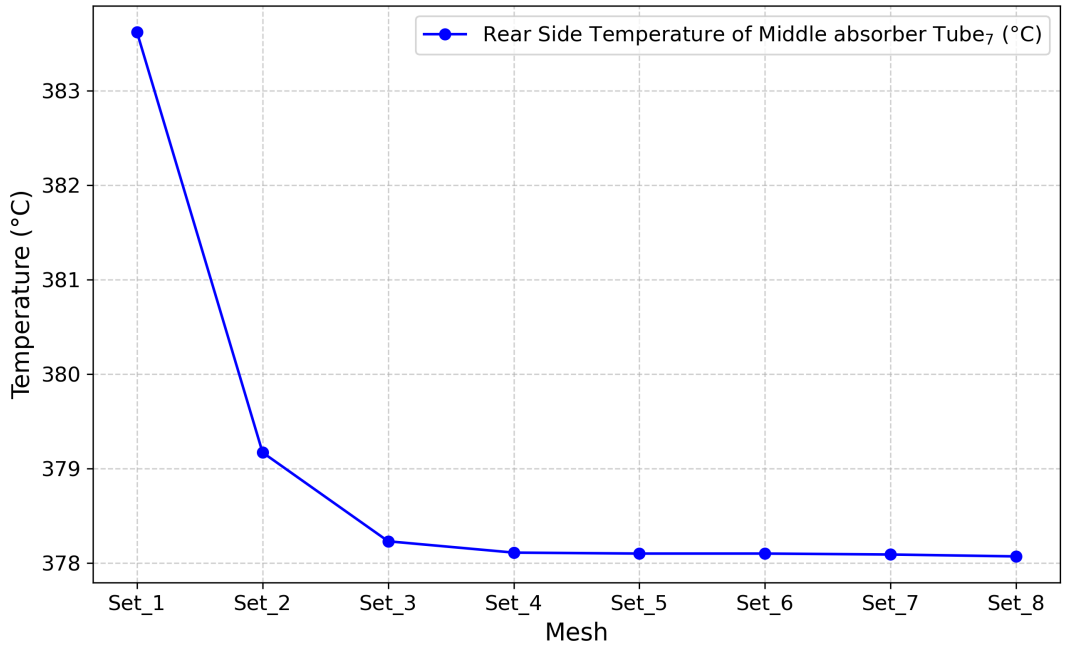

Figure 33: Rear Side Temperature of the Absorber Tube7 for Different Mesh Sizes in Thermal Model.

5 Opticl Results

The primary objective of optical simulation is to accurately model and analyze the flux distribution along the receiver surface. This is accomplished using the SPRAY software. Furthermore, this chapter covers the validation of the simulation results using experimental measurement data. For these measurements, eight Gardon-type flux gauges (accuracy $\delta = \pm 3\%$), distributed along the receiver height monitored the solar flux density depicted in Figure 34.

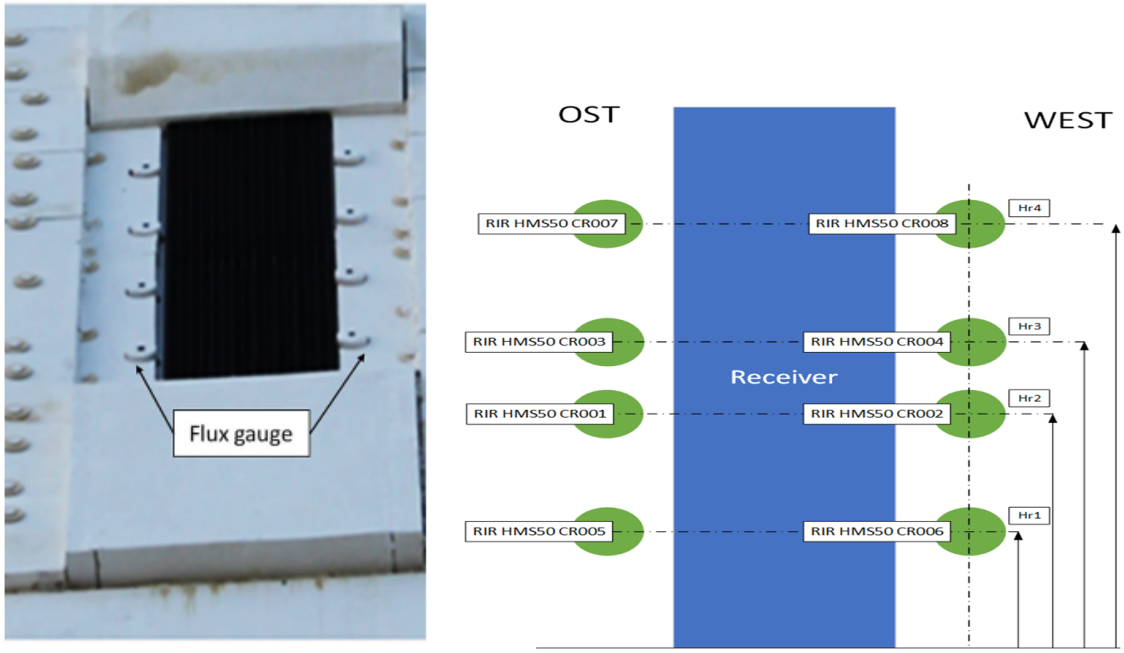

Figure 34: Flux Gauge Distribution on the Receiver Surface.

Three cases were validated under preheating and solar operation conditions, as outlined in Table 9. During preheating, time steps were selected from periods with a linearly increasing mean flux, while solar operation focused on a period with a nearly constant mean flux.

The HPMS-II test receiver is located at the MFT facility in Jülich, Germany, at a latitude of 50.912 ° N and an elevation of 87 meters above sea level. The key parameters for the associated solar field are provided in Table 9. The dimensions of the solar tower and multifocus tower significantly influence the degree of blocking and shading on the heliostats. Precise measurements of these dimensions, as well as the coordinates of the towers, heliostats, and aim points, are crucial for reliable optical simulations. For detailed specifications, see Appendix D.

Parameter	**Pre-Heating**	**Solar Operation**	
		Partial Load	**Full Load**
Date	19 August 2024		
Time	9:50 - 10:10	11:41	15:51
Mirror Reflectivity (%)	77.5		
Grid Resolution (nSubFact)	270 × 270		
No. of Heliostats	90 - 160	630	839
Direct Normal Irradiance (DNI) (W/m^2)	516.6662 - 561.759	654.6415	553.1058
Total Power Absorbed (W)	13,580 - 32,419	361,095	370,251

Table 9: Summary of Parameters for Simulated Case Studies in Preheating and Solar Operation.

5.1 Preheating Operation

The preheating period spans from 09:00 to 11:00, during which the number of active heliostats in the northern solar field is gradually increased to raise the average solar flux density, as shown in Figures 35 and 36. This adjustment aims to achieve a target receiver temperature of 350°C, minimizing thermal stress caused by temperature gradients between the front and back sides of the absorber tubes.

For the optical simulation, the selected simulated period was 20 minutes, from 09:50 to 10:10, during which a nearly linear increase in mean flux is observed (Figure 36). Additionally, Figure 36 presents measurements from eight flux gauges distributed along the receiver, as illustrated in Figure 34.

At the start of this interval, 90 heliostats focused on four aim points (0, 4, 20, and 24) on the receiver surface. By the end of the interval, 160 heliostats were distributed across five aim points (0, 4, 20, 22, and 24).

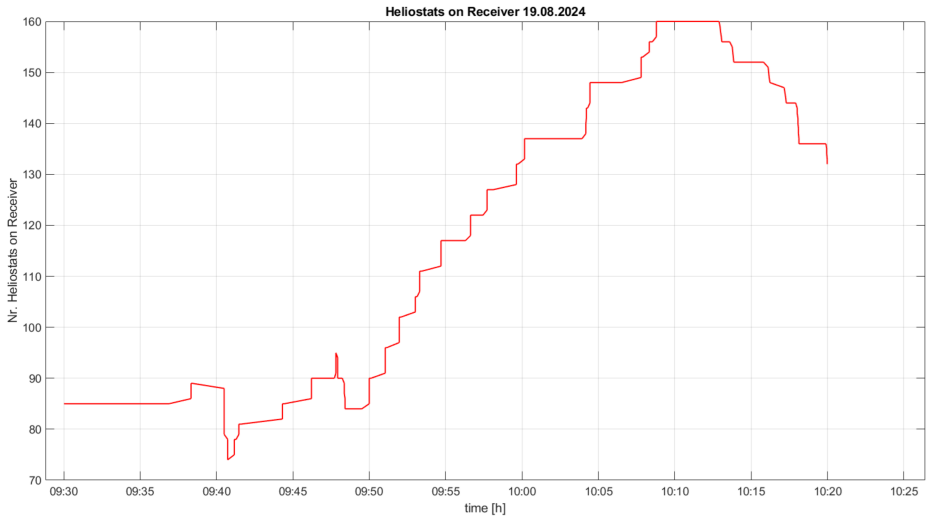

Figure 35: Number of Focused Heliostats During Preheating Phase.

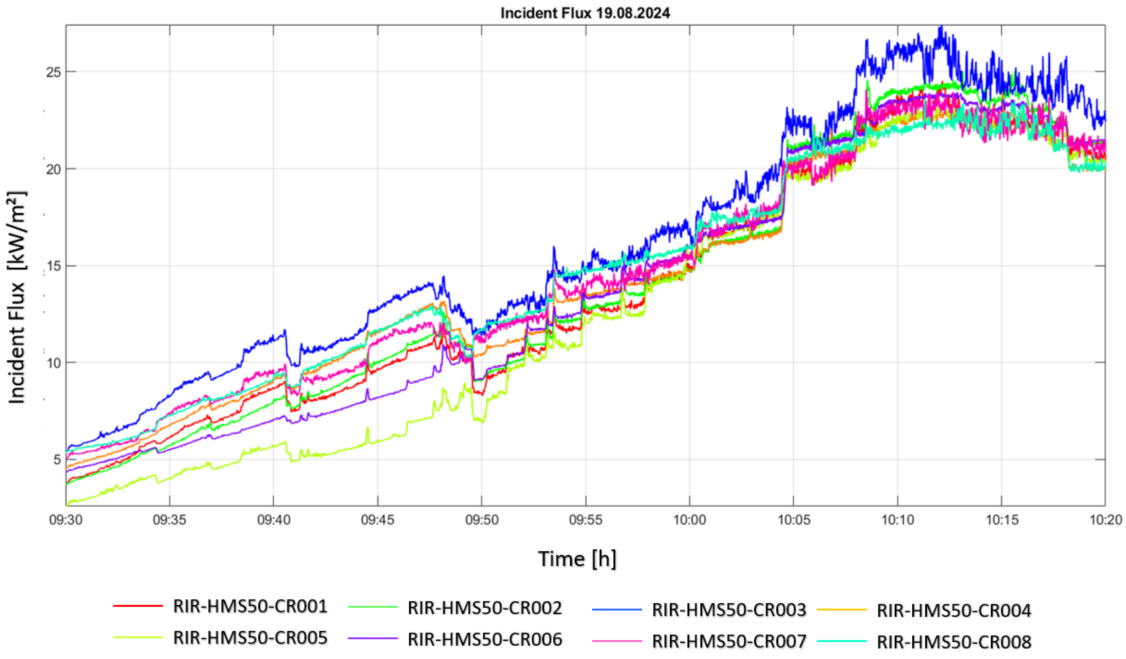

Figure 36: Incident Flux Measurements Using Flux Gauges During Preheating.

During the preheating operation, optical simulation validation was performed at 2-

minute intervals, resulting in a total of 10 flux simulations. To optimize the results and minimize the mean square error (MSE) between measured and simulated flux, a genetic algorithm was employed. The key parameters considered included rotational errors of the tracking axes, mirror slope error, and the X and Z coordinates of the aim points, as summarized in Table 10.

Parameter	Before Optimization	After Optimization
`Rotation error of tracking axes [rad]`	0.002 , 0.002	0.00 , 0.00
`Mirror Slope Error [rad]`	0.00115	0.003344
`Aim Points [X,Y,Z] [m]`		
`0`	-17.985 , -3.2 , 29.75	-17.68311 , -3.2 , 29.83663
`4`	-18.725, -3.2, 29.75	-18.42311 , -3.2 , 29.83663
`20`	-17.985 , -3.2 , 28.25	-17.68311 , -3.2 , 28.33663
`24`	-18.725 , -3.2 , 28.25	-18.42311 , -3.2 , 28.33663

Table 10: Optimized and Initial Parameter Values During Preheating at 9:50.

Since SPRAY software uses Monte Carlo ray tracing, which relies on a Gaussian distribution, variations can occur across different simulation runs. To ensure consistency and reproducibility, the rotational error of the tracking axes was set to zero for all simulations. Additionally, minor adjustments to the X and Z aim point coordinates, by 0.30189 m and 0.00685 m, respectively, reduced the flux error by approximately 50% to 60%, as shown in Tables 11, and Figure 37.

Flux Gauge No.	Measurement Results (kW/m^2)	Simulated Results (kW/m^2)	Error (%)
`RIR-HMS50-CR001`	8.404	14.9371	77.732 %
`RIR-HMS50-CR002`	9.142	15.226	66.544 %
`RIR-HMS50-CR003`	11.454	16.2769	42.104 %
`RIR-HMS50-CR004`	10.449	17.3605	66.145 %
`RIR-HMS50-CR005`	6.992	11.3052	61.691 %
`RIR-HMS50-CR006`	9.127	11.554	26.597 %
`RIR-HMS50-CR007`	11.359	17.1731	51.186 %
`RIR-HMS50-CR008`	11.611	16.8979	45.531 %

Table 11: Measured Flux Gauge Values vs. Simulated Results at 9:50 During Pre-Optimization Simulation.

Flux Gauge No.	Measurement Results (kW/m^2)	Simulated Results (kW/m^2)	Error (%)
`RIR-HMS50-CR001`	8.404	9.029	7.434%
`RIR-HMS50-CR002`	9.142	9.6428	5.4745%
`RIR-HMS50-CR003`	11.454	10.0913	**-11.899**%
`RIR-HMS50-CR004`	10.449	11.4195	9.288%
`RIR-HMS50-CR005`	6.992	6.867	-1.786%
`RIR-HMS50-CR006`	9.127	8.0311	**-12.004**%
`RIR-HMS50-CR007`	11.359	10.7241	-5.589%
`RIR-HMS50-CR008`	11.611	11.7228	0.0961%

Table 12: Measured Flux Gauge Values vs. Simulated Results at 9:50 Post-Optimization Simulation.

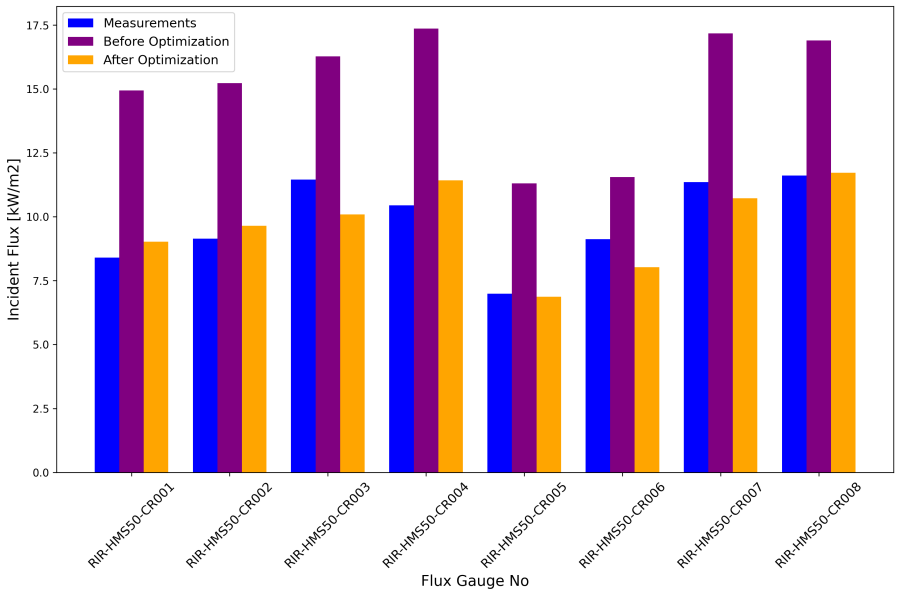

Figure 37: Comparison of Measurements, Pre-Optimization Simulation, and Post-Optimization Simulation at 9:50.

As presented in Tables 11 and 12, the measured versus simulated flux gauge values show significant improvements after optimization. For example, the error at flux gauge CR001 reduced from 77.73% to 7.43%, and at CR005 from 61.69% to 1.70%. These results demonstrate the substantial accuracy enhancements achieved through the optimization process. Results for subsequent time steps, after optimization, are provided in Appendix E.

5.2 Solar Operation Scenario

During the solar operation scenario, the required incident fluxes are influenced by the inlet and outlet temperatures of the molten salt, as well as the molten salt flow rate. Two different cases of partial and full operation are explained in this chapter.

5.2.1 Partial Load

The partial load case study was selected at 11:41, corresponding to stable incident flux conditions, as shown in Figure 38. At this time, 630 heliostats focused their reflections on aim points 7 and 17 of the receiver.

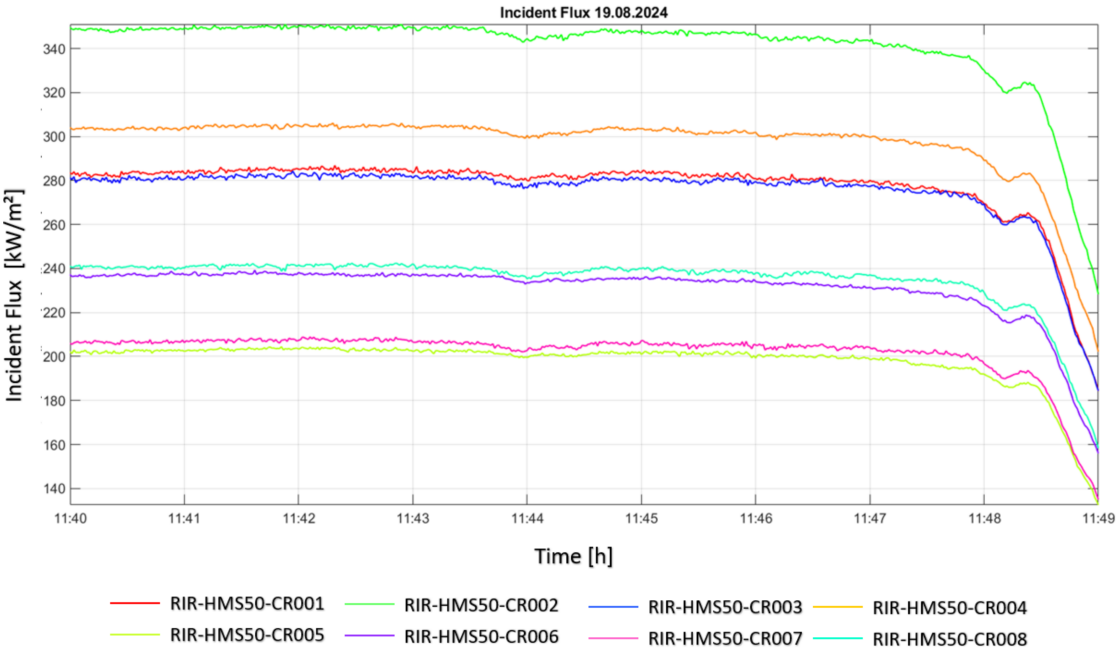

Figure 38: Incident Flux Measurements Using Flux Gauges During Partial Load Solar Operation.

As presented in Table 13, the maximum error, observed at flux gauge 4, was 8%. This error was minimized through an optimization process involving a slope error of 0.00254 and adjustments to the X and Z aim points by 0.17385 m and -0.47881 m, respectively.

Flux Gauge No.	Measurement Results	Simulated Results	Error %
RIR-HMS50-CR001	283.666	284.524	-0.303%
RIR-HMS50-CR002	350.5146	333.358	4.895%
RIR-HMS50-CR003	280.8064	290.922	-3.602%
RIR-HMS50-CR004	305.6526	332.769	**-8.872**%
RIR-HMS50-CR005	203.1858	196.421	3.329%
RIR-HMS50-CR006	236.9736	235.093	0.794%
RIR-HMS50-CR007	207.0196	210.085	-1.481%
RIR-HMS50-CR008	241.341	235.63	2.366%

Table 13: Measured Flux Gauge Values vs. Simulated Results During Partial Load Solar Operation.

5.2.2 Full Load

The full load case study was selected at 15:51, corresponding to the peak molten salt temperature of 602°C, during which the incident flux remained nearly constant, as shown in Figure 39. At this time, 839 heliostats were focused on aim points 7 and 17 on the receiver. Once the molten salt reached its peak temperature, the heliostat array began de-focusing from the receiver, causing a steady decline in the measured flux values after 15:51, as illustrated in Figure 39.

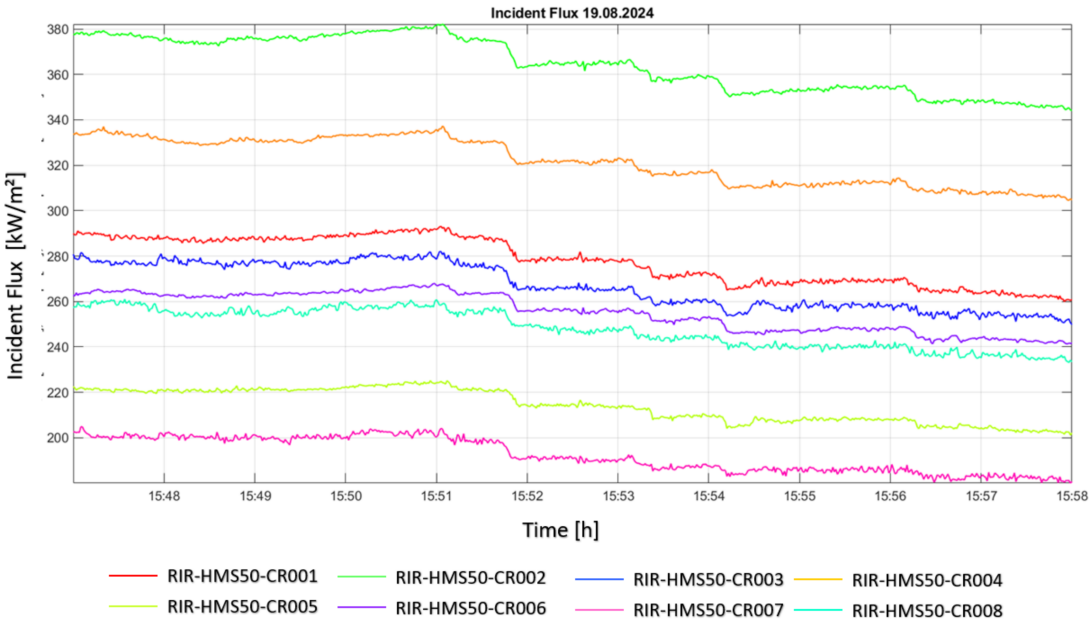

Figure 39: Incident Flux Measurements Using Flux Gauges During Full Load Solar Operation

As summarized in Table 14, the maximum error, observed at flux gauge 5, was 9%. This was minimized through an optimization process involving a slope error of 0.002504 and adjustments to the X and Z aim points by 0.2963 m and -0.58513 m, respectively.

Flux Gauge No.	Measurement Results	Simulated Results	Error %
RIR-HMS50-CR001	291.6300	277.749	-4.763%
RIR-HMS50-CR002	381.5187	369.929	-3.038%
RIR-HMS50-CR003	278.5687	270.854	-2.769%
RIR-HMS50-CR004	335.7584	353.444	5.627%
RIR-HMS50-CR005	224.3064	203.919	**-9.089** %
RIR-HMS50-CR006	267.0592	272.767	2.137%
RIR-HMS50-CR007	200.3627	185.156	-7.590%
RIR-HMS50-CR008	260.8605	237.84	**-8.825**%

Table 14: Measured Flux Gauge Values vs. Simulated Results During Full Load Solar Operation.

6 Optical Thermal Interface

This chapter describes the interface between optical and thermal simulations using FEMRAY, which bridges SPRAY and ANSYS. In the optical simulation with SPRAY, the receiver is modeled as a simplified two-dimensional rectangular surface. However, the thermal model represents the receiver in three dimensions to reflect the actual prototype. FEMRAY maps the flux density from SPRAY onto the FEM receiver, enabling a three-dimensional representation.

The FEMRAY process begins by importing the receiver geometry from ANSYS APDL and initiating SPRAY to calculate the solar flux density distribution. It incorporates the emissivity of the receiver and insulation surfaces. Using geometry data from ANSYS and flux distribution from SPRAY, FEMRAY assigns specific radiation flux densities to individual receiver elements, ensuring accurate mapping onto the three-dimensional geometry. FEMRAY generates a flux map containing the coordinates of each receiver element along with their corresponding solar flux densities. This flux map is then imported into ANSYS Workbench, where the solar flux density is applied to the receiver as a boundary condition for thermal simulation.

6.1 Preheating Operation

At the start of the optical simulation, 90 heliostats were focused on the receiver, resulting in relatively lower energy delivery. A significant portion of this energy was lost as spillage, while the absorber tubes and insulation absorbed smaller amounts of energy, with lower maximum heat flux values.

By the end of the optical simulation, the number of heliostats increased substantially, leading to higher energy delivery and absorption by the receiver. While spillage losses also increased significantly due to the higher energy input, the absorbed energy

by both the absorber tubes and insulation rose correspondingly, along with a notable increase in their maximum heat flux values. Reflection losses remained constant throughout the simulation.

This comparison emphasizes the impact of increased heliostat focus on energy distribution, absorption, and associated losses. A summary of both cases is provided in Table 15, and the heat flux distributions at the start and end of the simulation are illustrated in Figure 40.

Details	**09:50**	**10:10**
Heliostats	90	160
Delivered Energy (kW)	65.76	148.87
Spillage Losses (kW)	140.43	231.44
Reflection Losses (kW)	40.29	40.29
Absorbed Energy (kW)	25.48	58.96
Absorber Tubes (kW)	13.58	32.42
Max Heat Flux (kW/m^2)	11.65	25.2
Insulation (kW)	11.90	26.54
Max Heat Flux (kW/m^2)	3.01	6.2

Table 15: Sequential Schedule of Energy Distribution and Losses During Preheating.

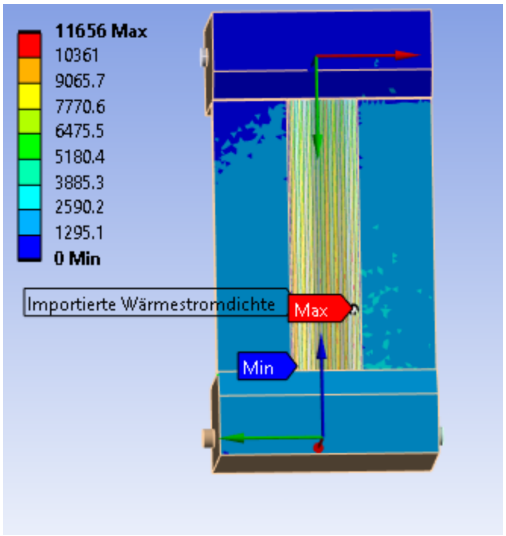

(a) Imported Heat Flux [W/m^2] at 9:50.

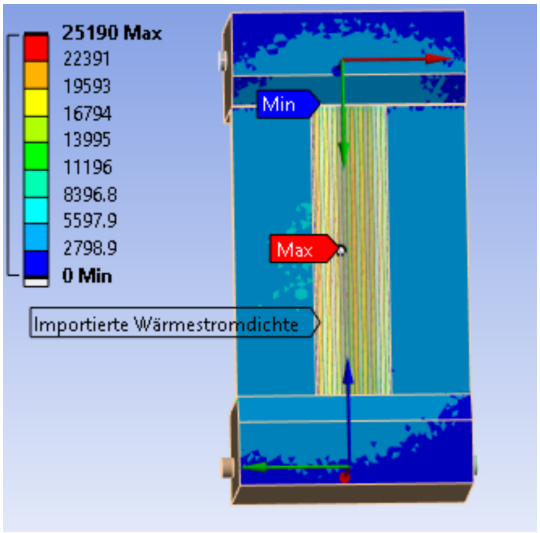

(b) Imported Heat Flux [W/m^2] at 10:10.

Figure 40: Heat Flux distributin During Preheating.

6.2 Solar Operation Scenario

During the Solar Operation Scenario, the number of focused heliostats increased compared to the preheating phase. Under Partial Load conditions, a significant amount of energy was delivered to the receiver, with a portion absorbed by the absorber tubes and radiation shield, while the remainder was lost as spillage and reflection.

Under Full Load conditions, the number of heliostats increased further (33.17% higher than Partial Load), resulting in a slight rise in delivered energy (3.54%) and absorption by both the absorber tubes and the radiation shield. However, the increase in absorbed energy was relatively small due to changes in weather conditions, particularly a decrease in Direct Normal Irradiance (DNI). Spillage and reflection losses also increased slightly in this scenario.

A summary of energy distribution and losses for both cases is provided in Table 16, while the heat flux distributions for Partial Load and Full Load are illustrated in Figure 41.

Details	**Partial Load**	**Full Load**
Heliostats	630	839
Delivered Energy (kW)	1234.00	1277.69
Spillage Losses (kW)	754.21	832.32
Reflection Losses (kW)	676.06	702.96
Absorbed Energy (kW)	557.94	574.73
Absorber Tubes (kW)	361.10	370.25
Max Heat Flux (kW/m^2)	327.20	350.50
Radiation Shield (kW)	196.85	204.49
Max Heat Flux (kW/m^2)	78.66	85.50

Table 16: Energy Distribution and Losses for Partial Load and Full Load Conditions.

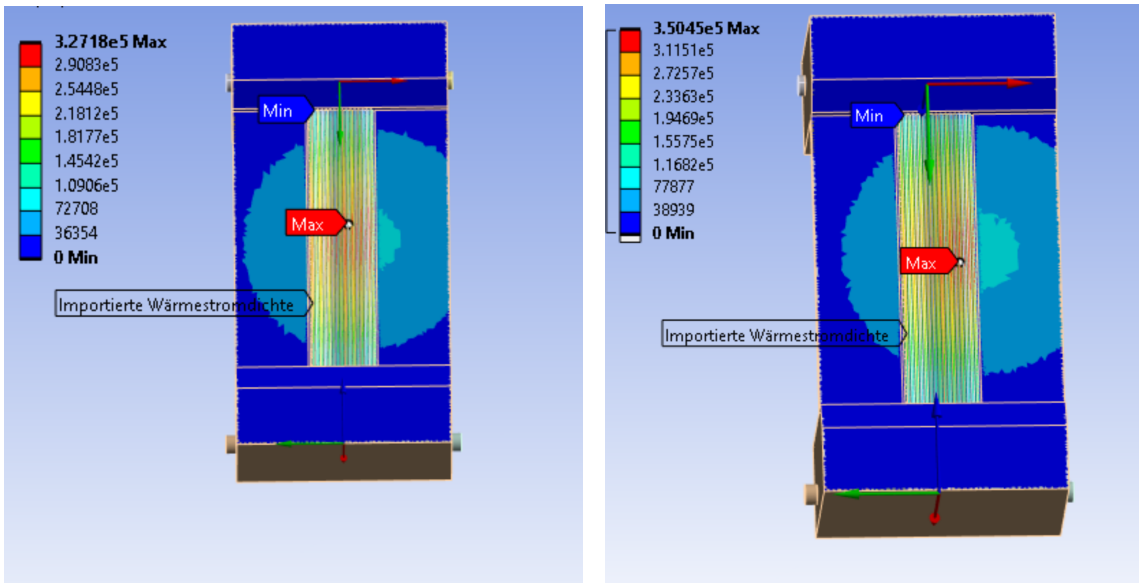

(a) Imported Heat Flux [W/m^2] in Partial Load at 11:41.

(b) Imported Heat Flux [W/m^2] in Full Load at 15:51.

Figure 41: Heat Flux distribution during Solar Operation.

7 Thermal Simulation Results

In this chapter, we present the thermal simulation results for two operational modes: Preheating Operation and Solar Operation. The simulation results are validated against experimental measurements.

7.1 Preheating Operation Scenario

During the Preheating Operation, specific measurements such as the ambient2 temperature (T_{ambient2}), were unavailable (see Convection to Ambient2). Therefore, an optimization process was implemented to minimize the Mean Squared Error (MSE) between the simulated and measured results. The temperature of ambient2 was evaluated over a range of values, spanning from 20% to 80% of the average rear side temperature. The MSE, calculated exclusively from Tube3 - Tube14 (Figure 17), accounts for differences in geometry between the prototype and commercial receivers.

Unlike the commercial receiver, which is cylindrical, the prototype has distinct starting and ending points. Consequently, wind magnitude and direction significantly affect the prototype's structure, particularly at its edges compared to the center. Further studies are necessary to investigate these effects, which are beyond the scope of this work. Based on the measurement results, the average rear side temperature of the absorber tubes between 9:50 and 10:10 was 252 °C. Table 17 summarizes the MSE values for variations in the average rear side temperature. The MSE reached its minimum at 49.06% of the average rear side temperature, as illustrated in Figure 42.

Average rear side temperature (%)	$T_{\mathbf{ambient\_2}}$ **(°C)**	**MSE**
20	50.4	836.41
40	100.9	143.25
60	151.3	158.66
80	201.8	615

Table 17: Summary of Percentage of Rear Side Temperature, Corresponding Ambient2 temperature, and MSE Values During Preheating.

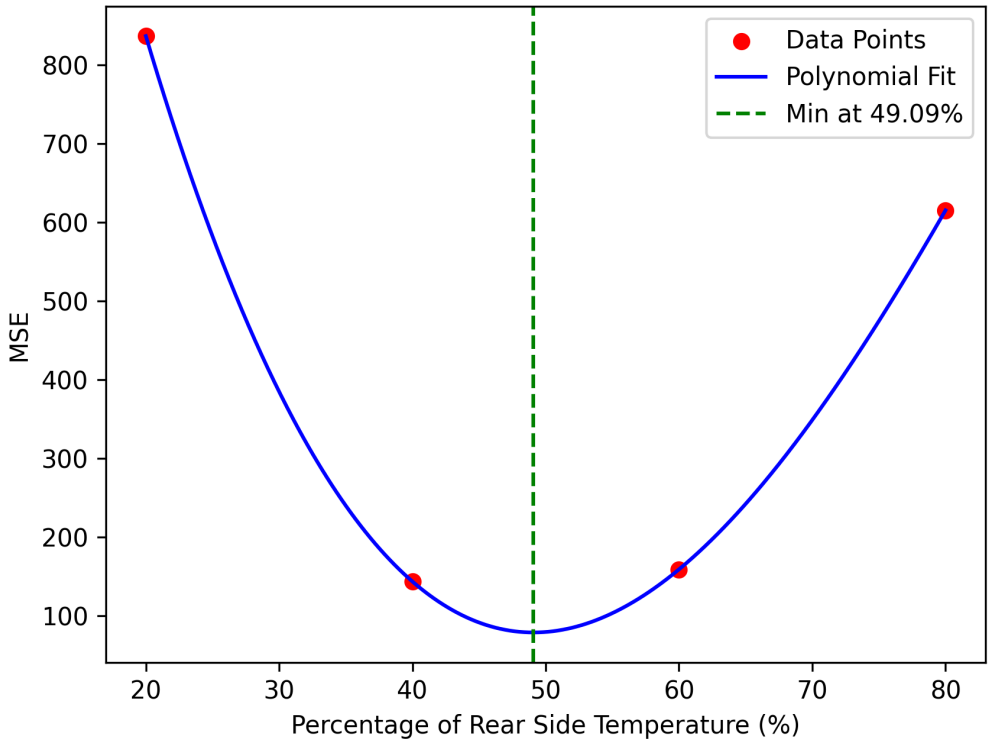

Figure 42: Percentage of Rear Side Temperature vs. Mean Square Error During Preheating.

The validated simulation results for the preheating scenario at the end of the transient simulation (10:10) showed a maximum temperature deviation of 15% for absorber tube1 compared to experimental measurements, as shown in Table 18 and Figure 43.

Tube_No	**Measurement Results** (°C)	**Simulated Results** (°C)	**Error** (%)
Tube1	306.07	351.19	-14.741
Tube2	293.13	326.48	-11.377
Tube3	302.43	324.27	-7.220
Tube4	308.58	323.72	-4.906
Tube5	316.02	323.27	-2.294
Tube6	321.57	324.5	-0.912
Tube7	322.94	323.33	-0.120
Tube8	324.45	323.67	0.240
Tube9	329.18	324.42	1.447
Tube10	329.07	324.08	1.516
Tube11	329.94	325.33	1.397
Tube12	326.10	323.58	0.774
Tube13	330.66	322.87	2.356
Tube14	331.14	324.34	2.055
Tube15	327.28	325.81	0.448
Tube16	327.72	354.14	-8.063

Table 18: Measurement vs. Simulated Values of Rear Side Tube Temperature During Preheating at 10:10.

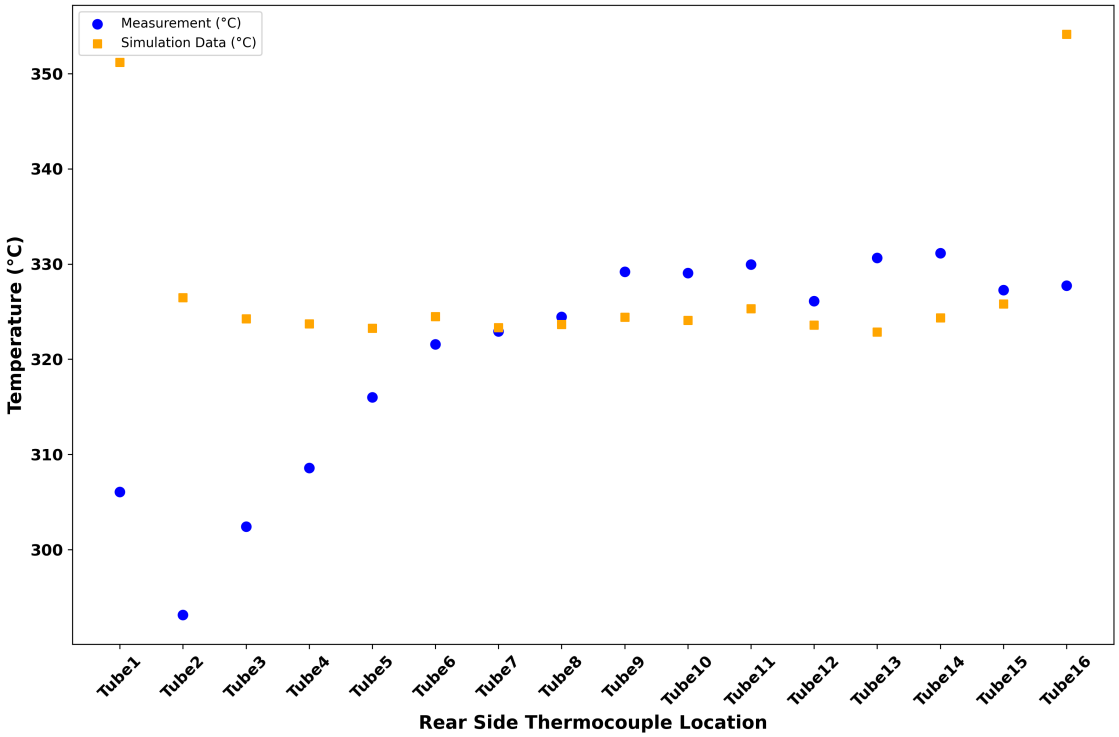

Figure 43: Measurement vs. Simulated Values of Rear Side Tube Temperature at During Preheating at 10:10.

Temperature Gradient Analysis

The temperature gradient for the middle absorber tube (Tube7) shows a linear increase during the thermal simulation period, as illustrated in Figure 44. The results indicate a maximum absolute error of 3%, as shown in Table 19. Temperature gradients for additional tubes are provided in **Appendix F**.

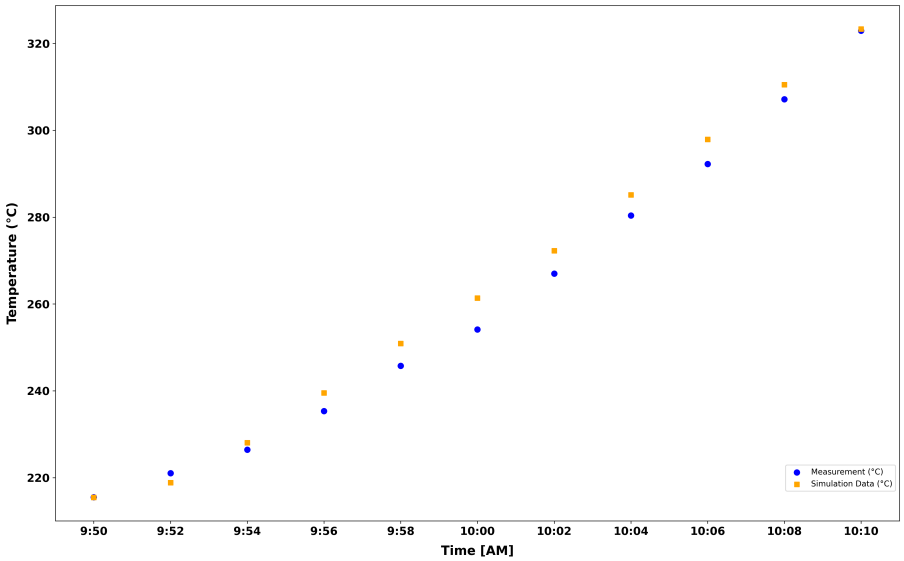

Figure 44: Measured vs. Simulated Temperature Gradients for Absorber Tube7 During Preheating.

Time	**Measurement Results** (°C)	**Simulated Results** (°C)	**Error** (%)
9:50	215.51	215.43	0.04%
9:52	221.01	218.84	0.98%
9:54	226.43	228.06	-0.72%
9:56	235.31	239.52	-1.79%
9:58	245.73	250.91	-2.11%
10:00	254.12	261.37	-2.85%
10:02	266.99	272.28	-1.98%
10:04	280.38	285.11	-1.69%
10:06	292.24	297.9	-1.94%
10:08	307.14	310.4	-1.06%
10:10	322.94	323.33	-0.12%

Table 19: Measured vs. Simulated Temperature Gradients for Absorber Tube7 During Preheating.

7.2 Solar Operation Scenario

During solar operation, molten salt serves as the primary HTF, capturing and transferring thermal energy from concentrated solar radiation. Table 4 summarizes three case studies analyzed under different conditions.

The simulation results correspond to the thermocouple installation locations. Two types of thermocouples were used: one measured the molten salt temperature, and the other measured the rear side temperature of the absorber tube, as shown in Figure 17. Validation results for each case study are presented below.

As explained in Convection to Ambient$_2$, the effect of T_{ambient2} was evaluated over a range from 20% to 80% of the average rear side temperature (350 °C). The influence of this variation on the rear side temperature of the absorber tubes was analyzed, as shown in Table 20 and Figure 45. Since changing T_{ambient2} had a minimal impact on the MSE, T_{ambient2} was set to 50% of the average rear side temperature.

Average rear side temperature (%)	$T_{\textbf{ambient2}}$ **(°C)**	**MSE**
20	70	11.72
40	140	10.36
60	210	9.11
80	280	7.73

Table 20: Summary of Percentage of Rear Side Temperature, Corresponding Ambient2 temperature, and MSE Values During Solar Operation.

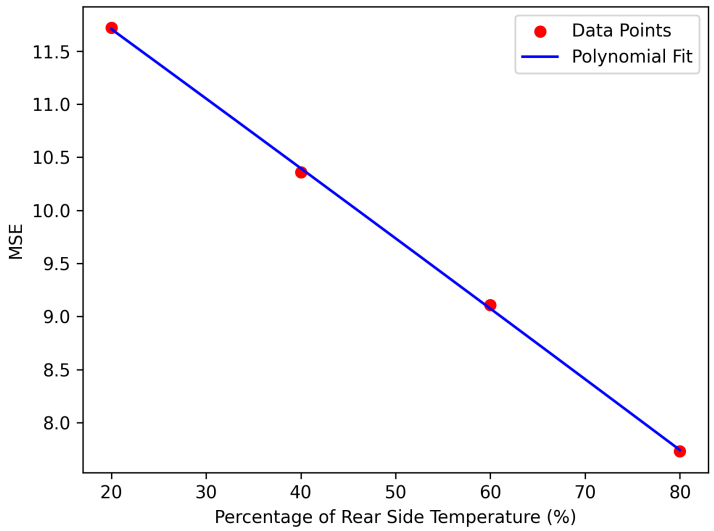

Figure 45: Percentage of Rear Side Temperature vs. Mean Square Error (MSE) During Solar Operation.

7.2.1 Calibration

During the calibration case study, no heliostats were focused on the receiver. The objective was to validate the thermal model under no heating conditions, comparing simulation results with measurements.

Figure 46 shows that the simulation results for the molten salt temperature are in close agreement with the measurements, with a maximum error of 0.1% observed at Header7 and an average error of 0.242%. The temperature decrease is attributed to frictional and general losses, including conductive and radiative heat dissipation along the pipeline.

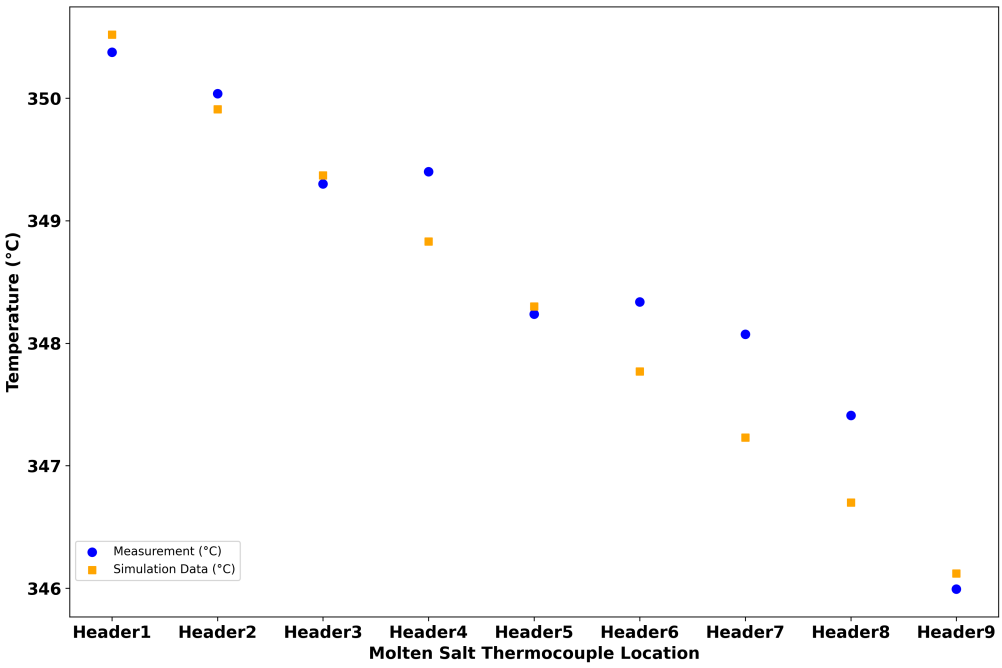

Figure 46: Measurement vs. Simulated Values of the Molten Salt Temperature during Calibration Case Study.

The rear side temperature validation, presented in Figure 47, also demonstrates strong agreement, with an average error of 0.820% and maximum deviations of 1.114% and 1.1% observed at Tube12 and Tube14, respectively. These results confirm the model's reliability for predicting molten salt and rear side absorber tube temperatures under no heating conditions.

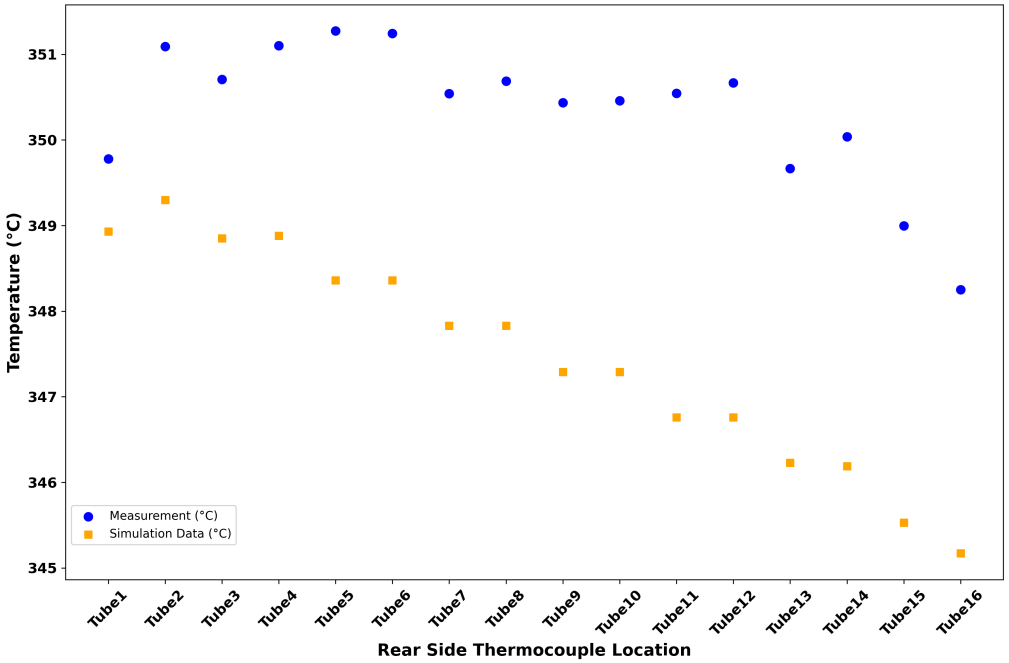

Figure 47: Measurement vs. Simulated Values of Rear Side Tube Temperature during Calibration Case Study.

7.2.2 Partial Load

In the part load case study, heliostats were focused on the receiver, introducing heat input to the molten salt system. This scenario validates the thermal model under partially operational conditions. As shown in Figure 48, the molten salt temperature increases along the pipeline, with a maximum error of 0.393% at Header4 and an average error of 0.17%. Similarly, the rear side temperature results, illustrated in Figure 49, align well with the measurements, with an average error of 0.25% and a maximum deviation of 2% at Tube1.

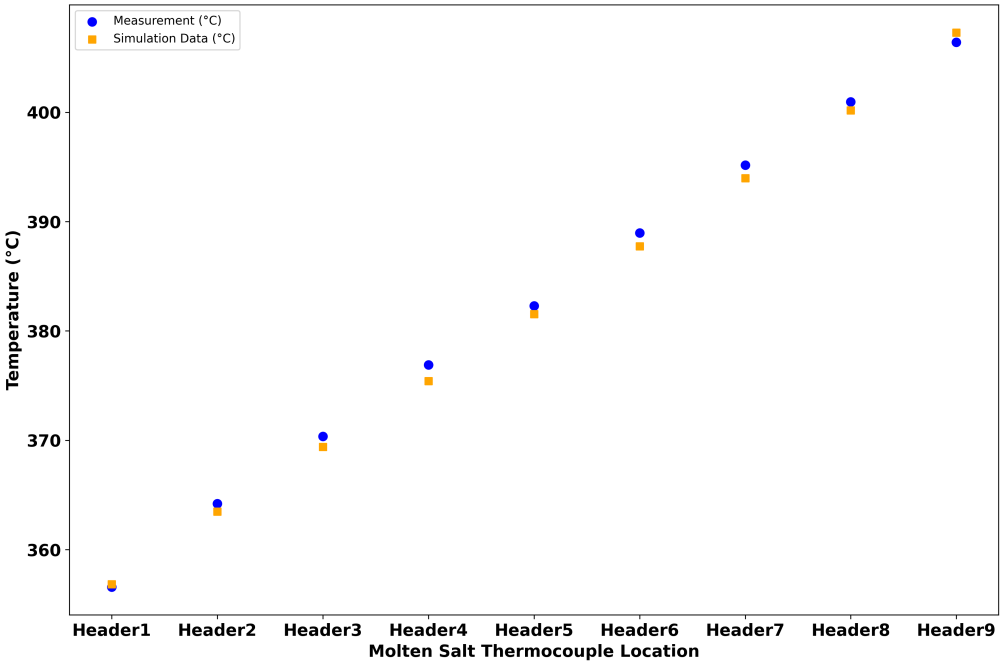

Figure 48: Measurement vs. Simulated Values of the Molten Salt Temperature during Partial Load Case Study.

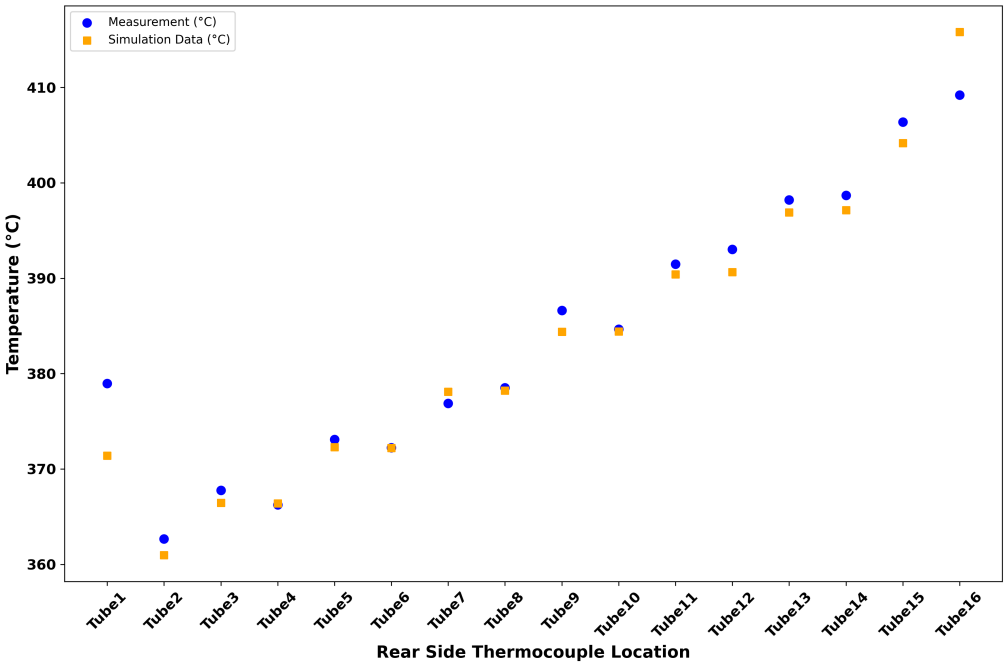

Figure 49: Measurement vs. Simulated Values of Rear Side Tube Temperature during Partial Load Case Study.

7.2.3 Full Load

In the full load case study, all heliostats were operational, delivering maximum energy to the receiver. This represents peak operating conditions and provides a critical validation of the thermal model under full system load. Figure 50 shows the molten salt temperature increases steadily along the pipeline, with a maximum error of 0.41% at Header7 and an average error of 0.24%. Similarly, the rear side temperature results, presented in Figure 51, show good agreement between simulations and measurements, with an average error of 0.8% and a maximum deviation of 1.23% at Tube9.

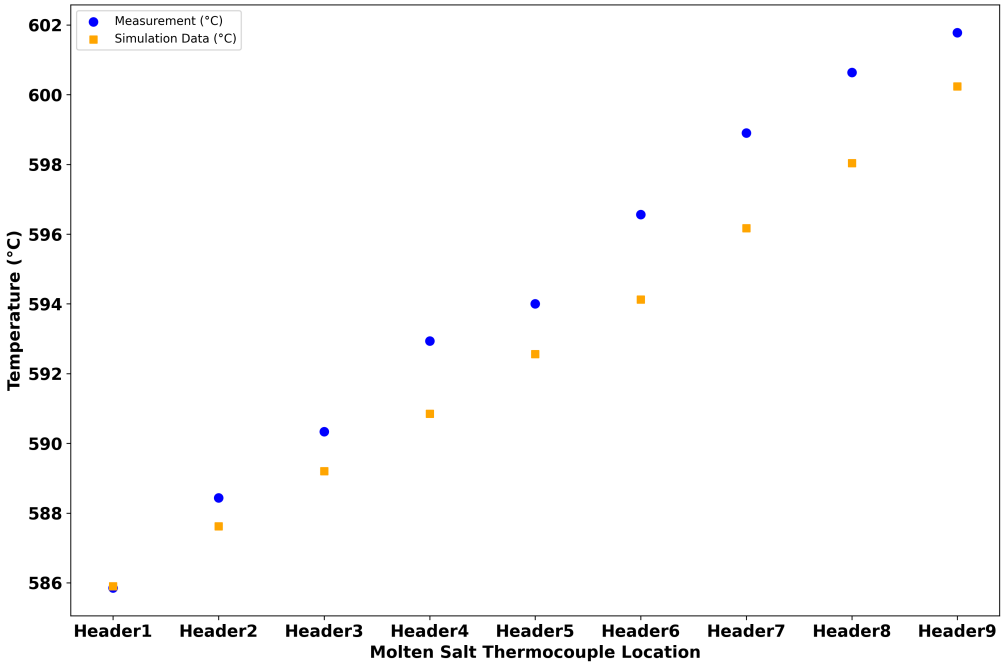

Figure 50: Measurement vs. Simulated Values of the Molten Salt Temperature during Full Load.

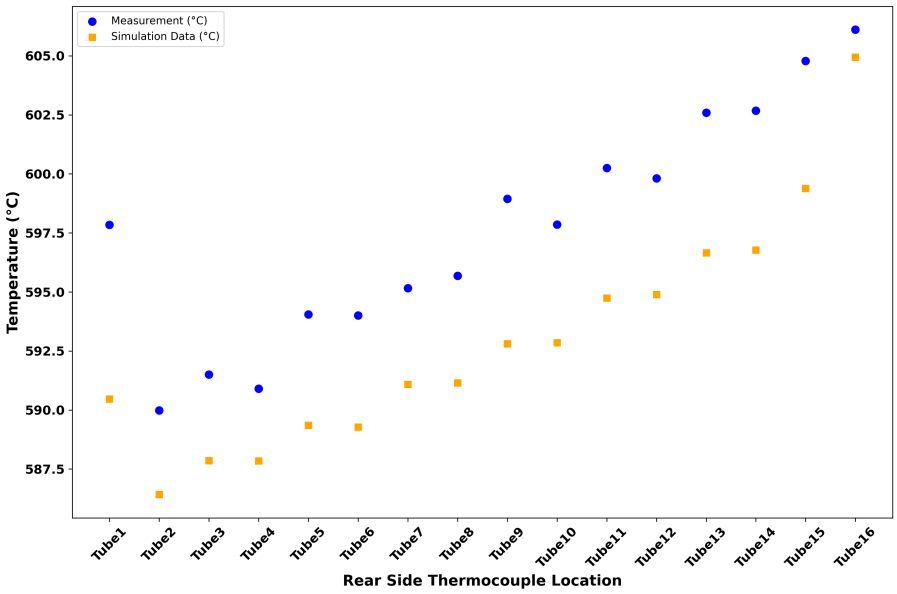

Figure 51: Measurement vs. Simulated Values of Rear Wall Tube Temperature during Full Load.

7.2.4 Heat Loss Analysis

The heat losses from the absorber tubes were analyzed under two operating conditions: Preheating operation and Solar Operation. The losses were divided into convective and radiative components for both the front and rear sides of the absorber tube.

Preheating Operation

During the preheating operation, two time steps were analyzed: the beginning of the simulation at 9:50 and the end of the simulation at 10:10, as presented in Table 21.

Time	**Front Side (W)**		**Back Side (W)**		**Total Losses (W)**		**Percentage (%)**	
	Conv.	**Rad.**	**Conv.**	**Rad.**	**Conv.**	**Rad.**	**Conv.**	**Rad.**
09:50	3740.6	5639.0	888.38	485.59	4628.98	6125.19	43.04%	56.96%
10:10	7112.3	16263.0	2987.4	2639.4	10099.7	18902.4	34.82%	65.18%

Table 21: Heat Losses During Preheating During Preheating.

At the start of the simulation (9:50), total losses were approximately half of those at the end (10:10). This was due to the relatively low temperature of the absorber tube, resulting in convective and radiative losses being nearly equal, with convective losses contributing 43.04 % of the total and radiative losses 56.96 %. By 10:10, as the temperature of the absorber tube increased, radiative losses became dominant, contributing 65.18 % compared to 34.82 % for convective losses. This shift highlights the increasing influence of radiative losses as the tube temperature rises during preheating.

Solar Operation

The heat losses during the solar operation were analyzed under three operating conditions: Calibration, Part Load, and Full Load. The losses were divided into convective and radiative components for both the front and rear sides of the absorber tube, as shown in Table 22.

Case	**Front Side (W)**		**Rear Side (W)**		**Total Losses (W)**		**Conv. %**	**Rad. %**
	Conv.	**Rad.**	**Conv.**	**Rad.**	**Conv.**	**Rad.**		
Calibration	7101.2	14480	2174.8	2141.4	9276	16621.4	36%	64%
Part Load	10938	24624	2643	2267.8	13581	26891.8	34%	66%
Full Load	14650	63924	4131.4	1006.8	18731.4	64930.8	22%	78%

Table 22: Heat Losses for Calibration, Part Load, and Full Load Cases.

As shown in Table 22, radiative losses increase significantly with higher loads, contributing 64 % during calibration and reaching 78 % under full load conditions. In contrast, convective losses, which account for 36 % during calibration, decrease to 22 % under full load. These changes are attributed to the rising pipe temperature with the increasing load.

These results highlight the dominance of radiative losses at higher loads and underscore the need for strategies to minimize them to improve system efficiency.

8 Conclusions

This study analyzed the thermo-optical performance of a high-performance test receiver system for next-generation molten salt solar tower plants. An FEM model of the test receiver was created in ANSYS, incorporating the receiver geometry and thermal boundary conditions established in this work.

Before filling the receiver with solar salt, the pipes must be preheated to prevent molten salt solidification. During the preheating operation, the receiver is filled with synthetic air, and the absorber tubes are heated using solar radiation, while other tubes, embedded in insulation, are heated with heat tracing. This process continues until the tube temperature reaches 350°C. Subsequently, the solar operation phase begins, and the receiver is filled with solar salt. Two operational scenarios were analyzed in the thermo-optical simulations: a transient thermal simulation for the 20-minute preheating phase and a steady-state thermal simulation for the solar operation phase.

Both simulations were coupled with a ray-tracing model, developed using SPRAY software, to determine the heat flux density distribution on the receiver surface and account for optical losses such as reflection and spillage. The accuracy of the optical simulation was validated by comparing measurement data with simulation results. An optimization process was conducted to adjust heliostat aiming on the receiver surface by minimizing the mean square error (MSE) between the measurements and the simulation results. This optimization reduced the error by approximately 70%. The optimization process revealed a maximum deviation of 16% during preheating, attributed to low flux density, whereas the maximum deviation during solar operation was 9%.

The thermal simulation was conducted using the FEMRAY interface program, integrated into the FEM model in ANSYS, to simulate the flux density distribution over

the receiver surface. The model evaluated the molten salt and rear tube side temperatures at the thermocouple locations during solar operation and calculated heat losses, including convection and radiation to the ambient environment. During preheating, only the rear tube side temperatures were validated against measurement data.

The convective heat transfer coefficient within the tubes was calculated using different approaches depending on the operational mode. During preheating, with stationary air, natural convection was considered. Due to the non-uniform flux distribution on the receiver tubes, identifying a suitable heat transfer coefficient from existing correlations or previous studies proved challenging. Consequently, a CFD model using CFX was employed to analyze the heat transfer at different time steps. In contrast, during solar operation, when the molten salt flow in the tubes is turbulent, the Gnielinski correlation was applied to calculate the convective heat transfer within the tubes.

An optimization process was also required to estimate the ambient temperature in the gap between the rear side of the absorber tubes and the insulation surface. The temperature T_{ambient} significantly influences convection losses during preheating and has a minor effect during solar operation.

We observed that radiation losses were approximately 2 to 3 times higher than convective losses. Additionally, the highest losses were observed at full load, as the molten salt and absorber tubes reached their maximum temperatures of 600°C and 605°C, respectively. The validation results showed a maximum deviation of 0.4% in the outlet molten salt temperature and 2% on the rear side of the absorber tubes during solar operation. However, during the preheating phase at 10:10, the maximum deviation was 15% on the rear side of the absorber Tube1.

Future work on the HPMS-II receiver test system should focus on further investigating the wind magnitude and direction, as well as the friction of the receiver tubes, which was neglected in this study assuming smooth tubes. Both of these parameters significantly impact convective losses to the atmosphere. Furthermore, the current preheating process takes approximately 2 hours during measurements. Therefore, further research is needed to reduce preheating time and minimize thermal stress. This will require a structural-mechanical evaluation based on thermal analysis.

A Material Properties

Molten Salt Properties

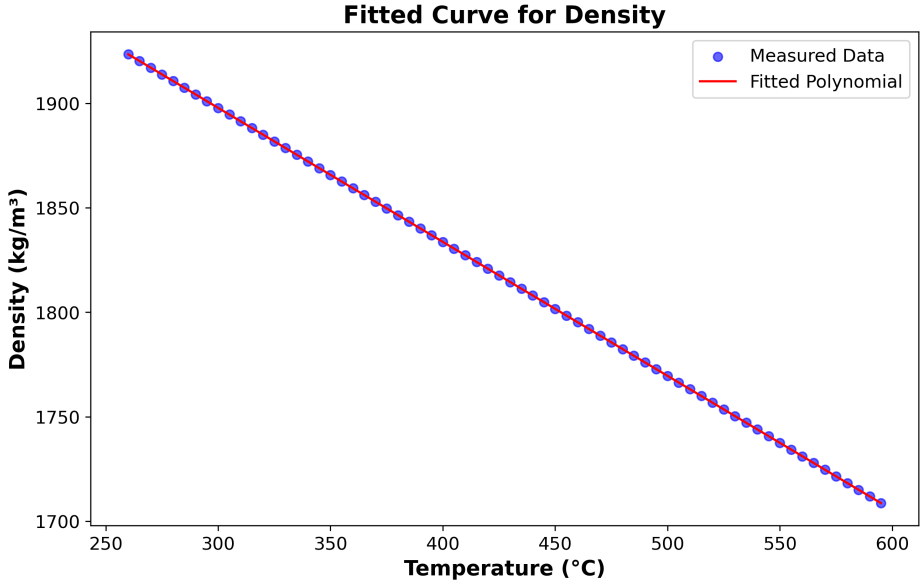

Figure 52: Fitted Polynomial Curve for Measured Density vs. Temperature with fitted Polynomial equation
$y = 2.090 \times 10^{3} - 6.411 \times 10^{-1} x$.

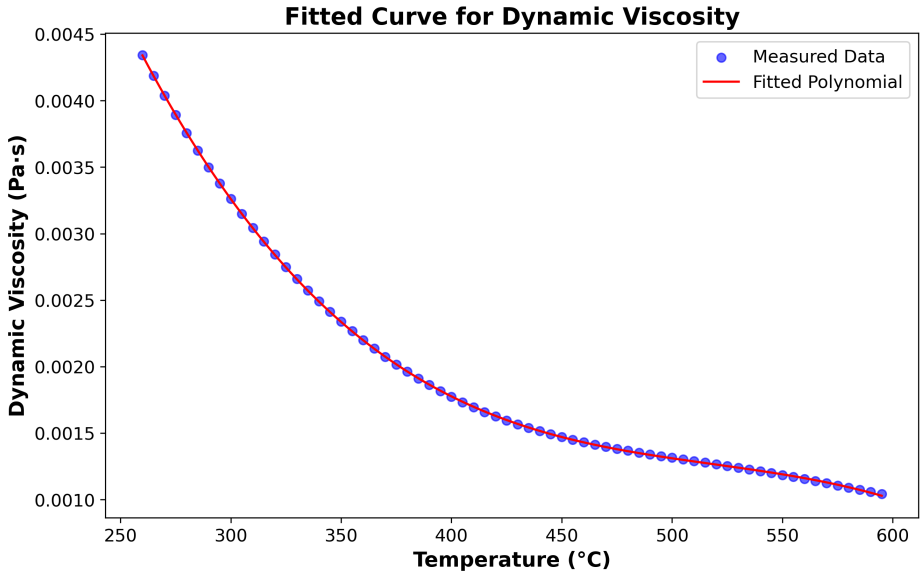

Figure 53: Fitted Polynomial Curve for Measured Dynamic Viscosity vs. Temperature with fitted Polynomial equation
$y = 2.297 \times 10^{-2} + (-1.230 \times 10^{-4})x^{1} + (2.408 \times 10^{-7})x^{2} + (-1.704 \times 10^{-10})x^{3} + (1.507 \times 10^{-14})x^{4}$.

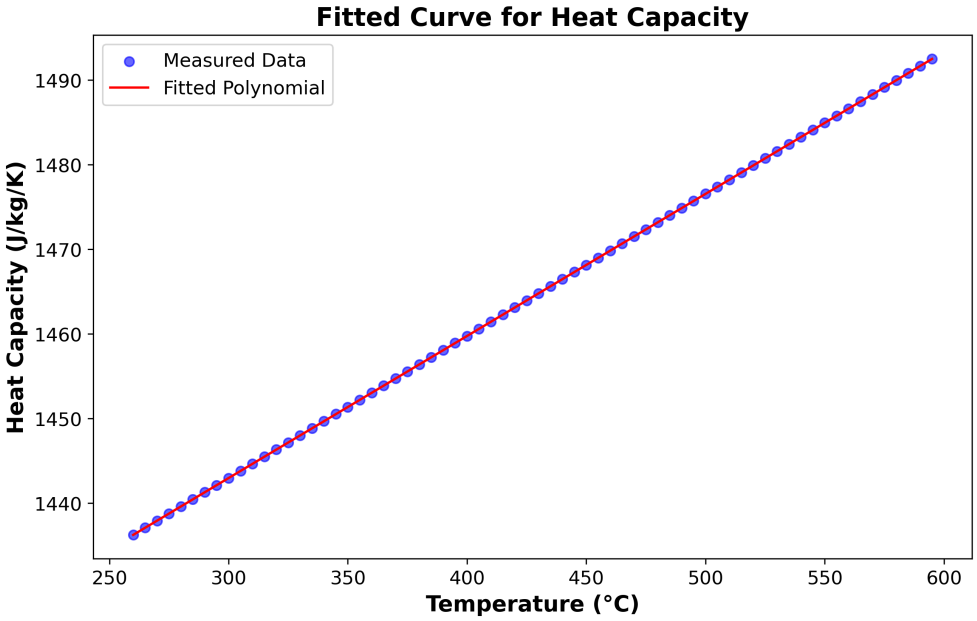

Figure 54: Fitted Polynomial Curve for Measured Heat Capacity vs. Temperature with fitted Polynomial equation
$y = 1.393 \times 10^{3} + 1.679 \times 10^{-1}x$.

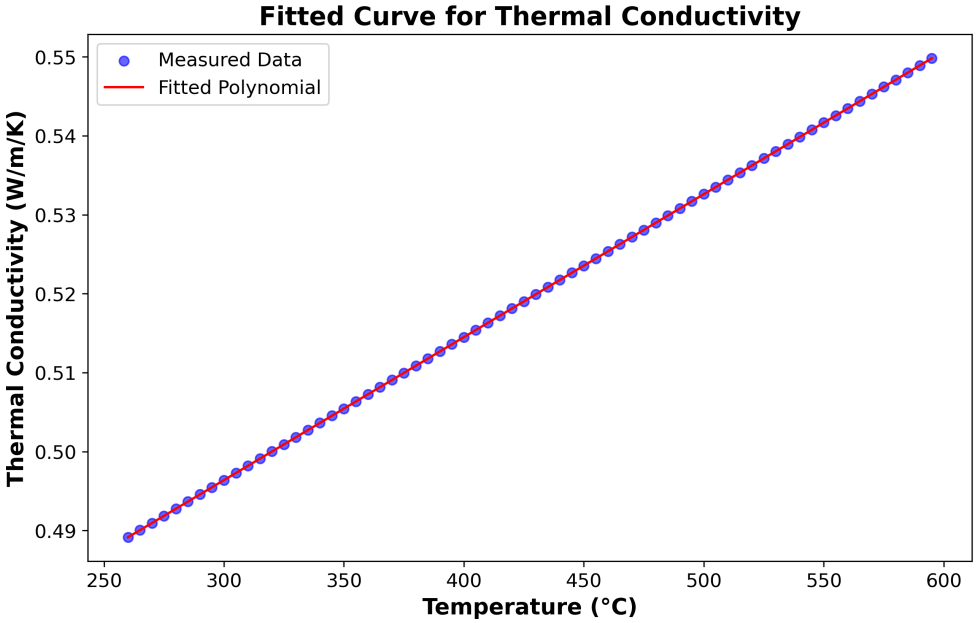

Figure 55: Fitted Polynomial Curve for Measured Thermal Conductivity vs. Temperature with fitted Polynomial equation
$y = 4.421 \times 10^{-1} + 1.811 \times 10^{-4}x$.

DMV 310N Properties

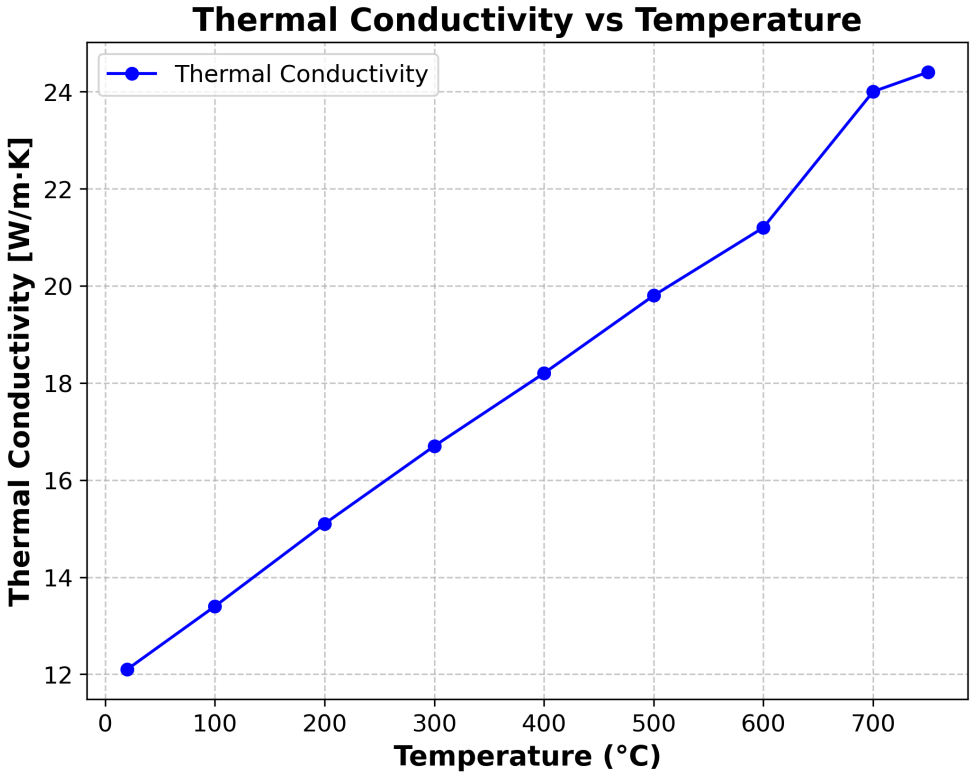

Figure 56: Thermal conductivity vs temperature GmbH 2024.

Due to the lack of information on the density and specific heat capacity of DMV 310N, and given the similarity in Cr/Ni composition between DMV 310N and 316LN stainless steel, the thermophysical properties of 316LN at room temperature were used as substitutes, as these are the only available data Ltd. 2024.

The chosen values in transient simulation are: specific heat capacity, $485\,\mathrm{J/kg \cdot K}$, and density, $7990\,\mathrm{kg/m^3}$.

B CFD Preheating

B.1 Boundary Conditions for CFD Simulation

B.1.1 Constant Temperature

The effect of heat tracing on bending pipes has been considered as a constant temperature applied to the absorber tube during the CFD simulation, as described in Table 23.

Time Step	**Upper Edge Temperature** [°C]	**Lower Edge Temperature** [°C]
10:00	369.79	357.65
10:06	371.73	365.66
10:10	373.6	364.3

Table 23: Temperature values at upper and lower edges at different time steps.

B.1.2 Convection and Radiative Losses

The incident flux was imported from an optical simulation into the CFD model within the CFX program. Consequently, radiation losses could not be directly activated. To address this limitation, radiation losses were calculated analytically using Equations 2.26 and 2.28 and combined with convection losses from Equation 2.3. The resulting combined heat transfer coefficient (HTC_{combined}) was incorporated into the CFD simulation to account for both convective and radiative losses, as illustrated in the flowchart in Figure 57. The combined HTC was further expressed as a function of wall temperature for both sides of the absorber tube.

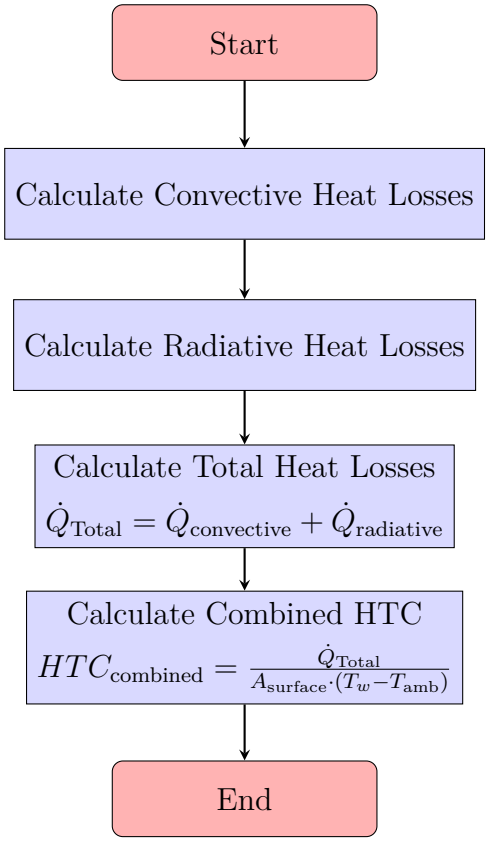

Figure 57: Flowchart for Calculating the Combined HTC on the Outer Wall Surfaces.

Front Side of Absorber Tube

The convective HTC was calculated at a wind velocity of 0.6 m/s, as illustrated in Figure 16. Convective losses were then determined using Equation 2.3, while radiative losses were calculated using Equation 2.26 as a function of the outer wall temperature. Following the process outlined in the flowchart in Figure 57, the HTC_{combined} for the front side of the absorber tube is represented in Figure 58.

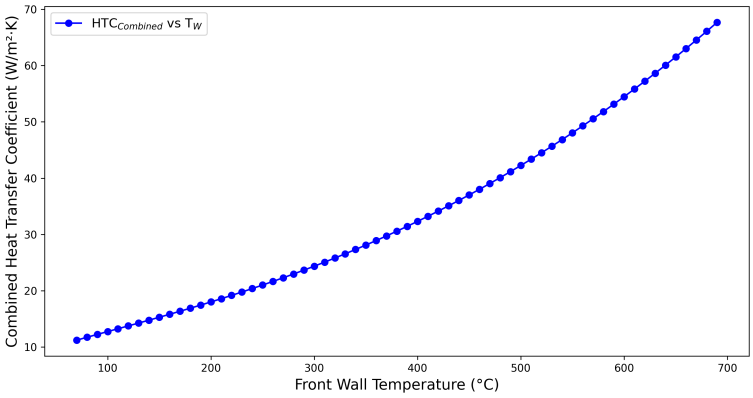

Figure 58: Combined HTC vs Front Wall Temperature.

Rear Side of Absorber Tube

The HTC_{Combined} for the rear side was calculated using the same approach as for the front side. However, Figure 18 was used to determine the convective HTC on the rear side, while Equation 2.28 was employed to calculate the radiation losses as a function of the outer wall temperature. Due to insufficient experimental data, the temperature difference between $T_{\textbf{ambient}_2}$ and $T_{\textbf{acceptance}}$ was assumed to be 30 [°C].

As discussed in Section: Convection to Ambient$_2$, during pre-heating, the ambient$_2$ temperature (T_{ambient_2}) has a significant influence on the HTC. Therefore, the value of T_{ambient_2} varies with the time step, as shown in Table 24. This variation leads to different equivalent HTCs on the rear side, as illustrated in Figures 59, 60, and 61 for various time steps.

Time	**Measurement Temperature [°C]**	$T_{\textbf{ambient2}}$ **[°C]**	$T_{\textbf{acceptance}}$ **[°C]**	$T_{\textbf{w}}$ **[°C]**	**View Factor**
10:00	254.12	130	160	200-500	1
10:06	292.24	145	175	215-500	1
10:10	322.94	165	195	235-500	1

Table 24: Rear Side Temperature During Preheating.

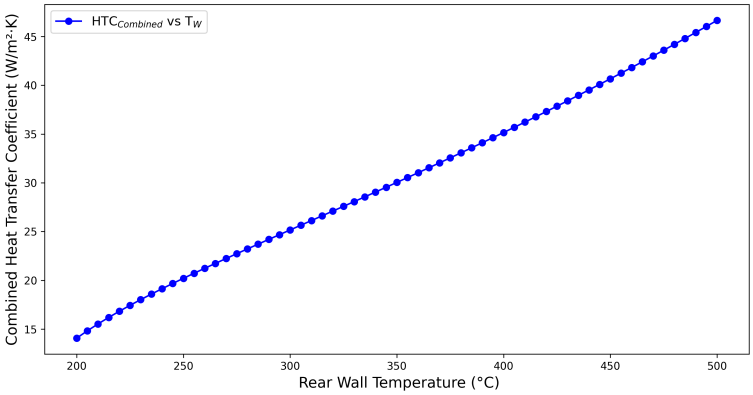

Figure 59: Combined HTC vs. Rear Side Temperature at 10:00.

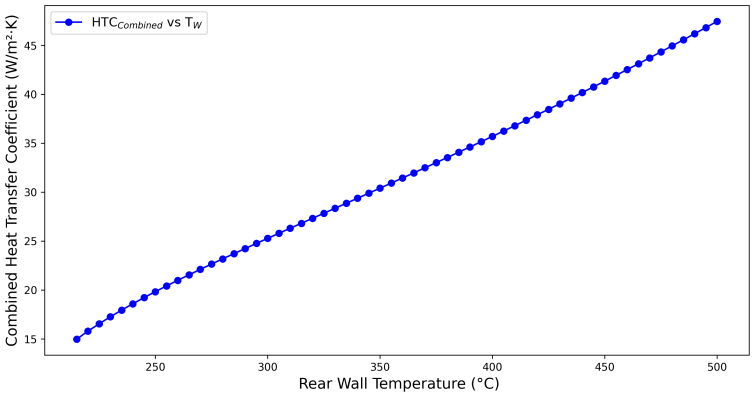

Figure 60: Combined HTC vs. Rear Side Temperature at 10:06.

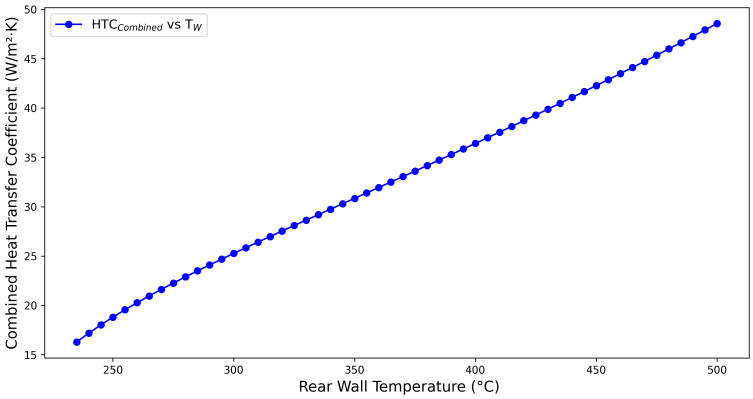

Figure 61: Combined HTC vs. Rear Side Temperature at 10:10.

B.2 Convective HTC During at 10:00

At 10:00, the maximum flux distribution on the front side of the absorber tube is $2.556 \times 10^3\,\mathrm{W/m^2}$, as illustrated in Figure 62. This results in a non-uniform temperature distribution, as shown in Figure 63. The variations in buoyancy forces represents in Figure 64.

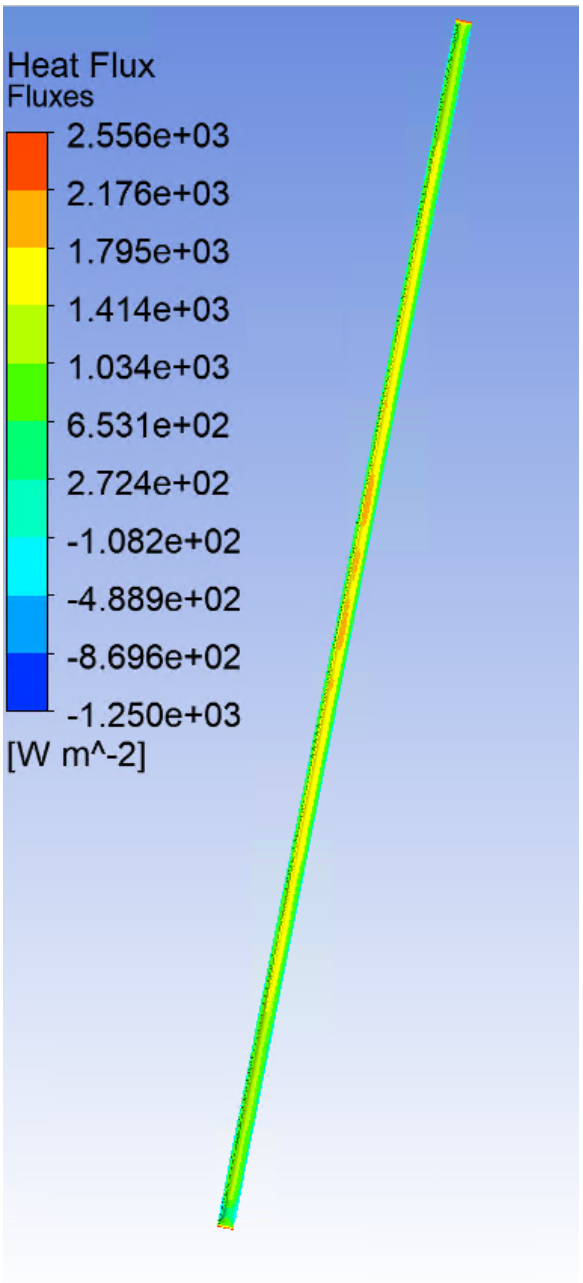

Figure 62: Flux Distribution on the Front Side of the Absorber Tube During Preheating at 10:00.

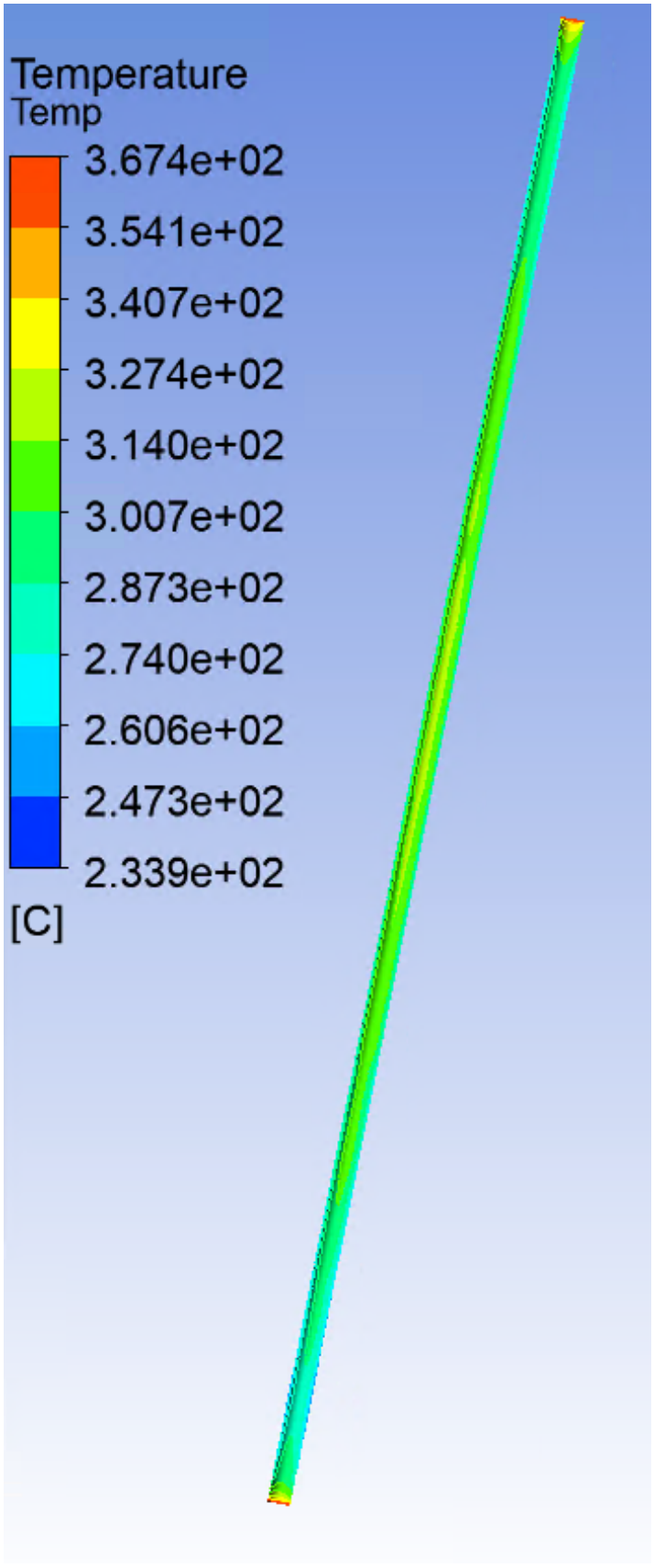

Figure 63: Temperature Distribution on the Front Side of the Absorber Tube During Preheating at 10:00.

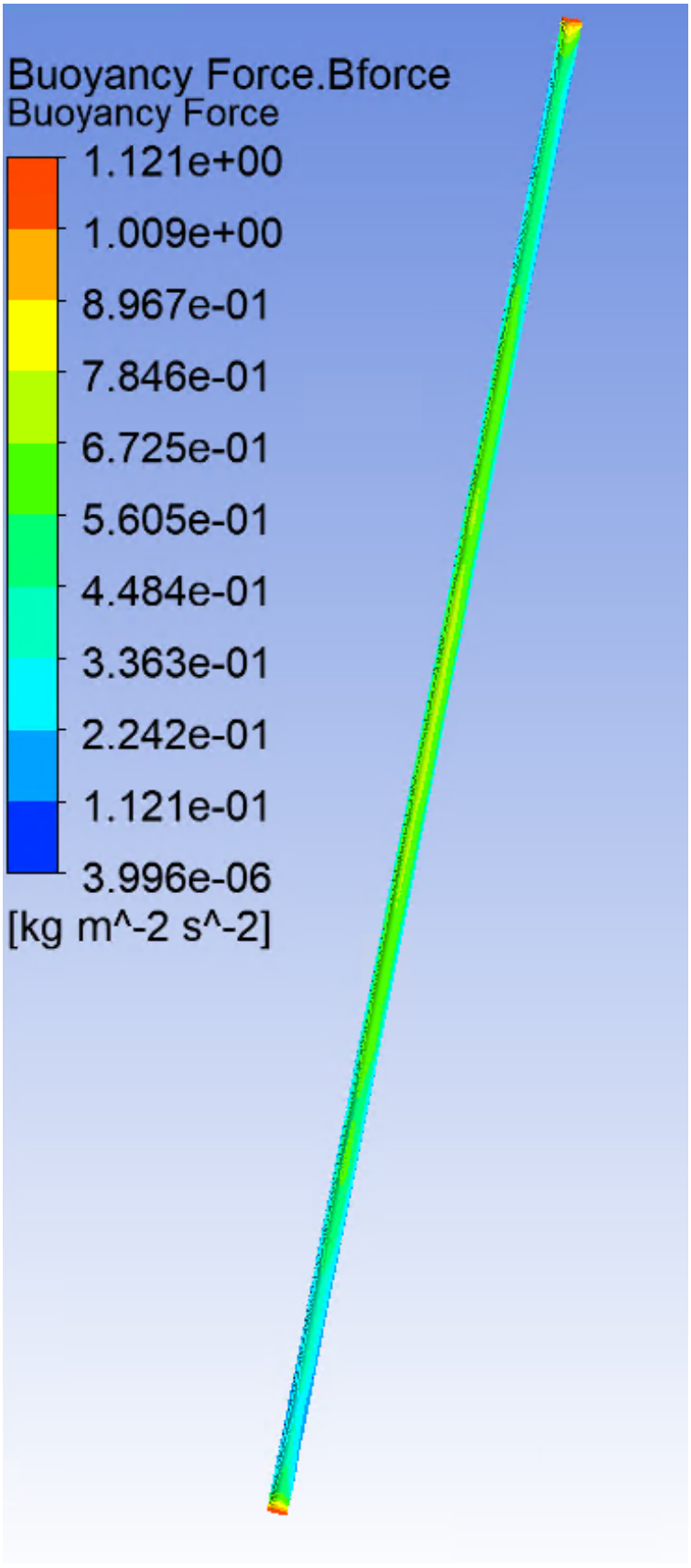

Figure 64: Buoyancy Force Distribution on the Front Side of the Absorber Tube During Preheating at 10:00.

The temperature distribution of air in the ZX plane is illustrated in Figure 65. The simulated temperature was 256.262°C, while the measured temperature was 254.12°C with absolute error 0.84 %.

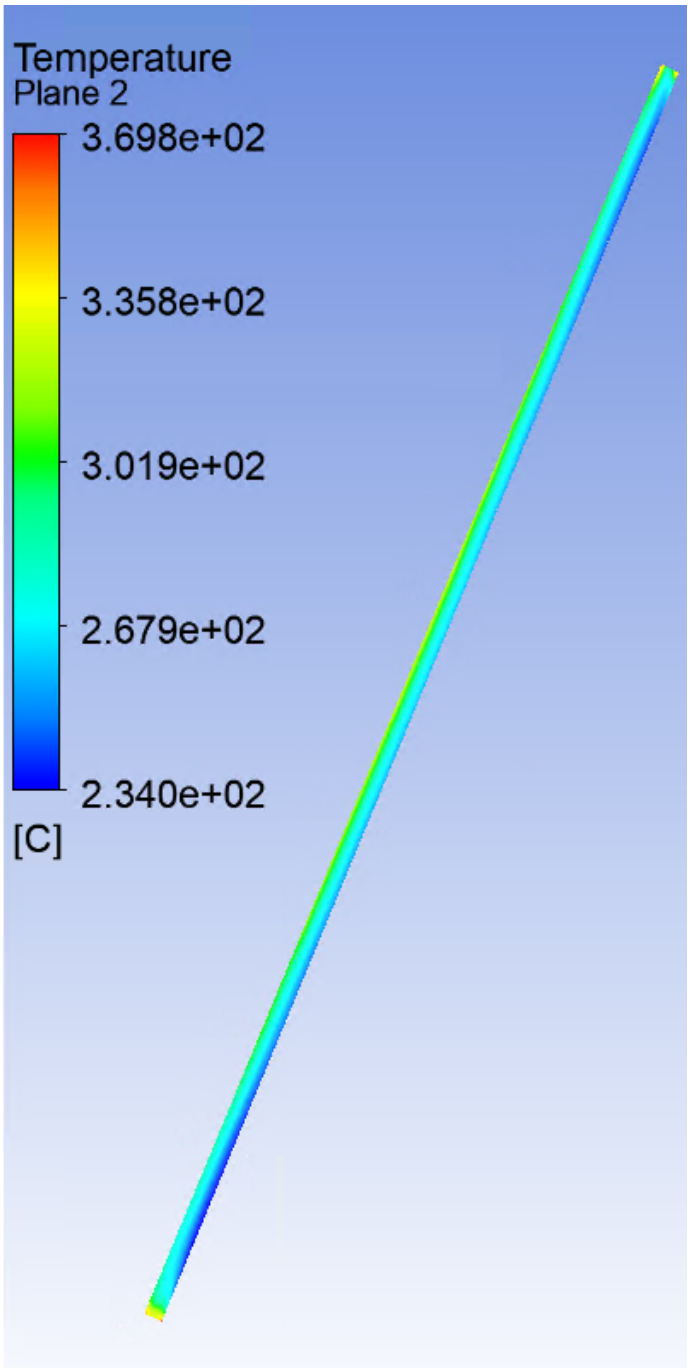

Figure 65: Temperature Distribution in the ZX Plane During Preheating at 10:00.

To calculate the wall HTC within the tube, its variation along the Z-axis is illustrated

in Figure 66. The average wall HTC at 10:00 AM is calculated as 4.75 W/m^2K "Calculated at Average Air Temperature 273.612°C.

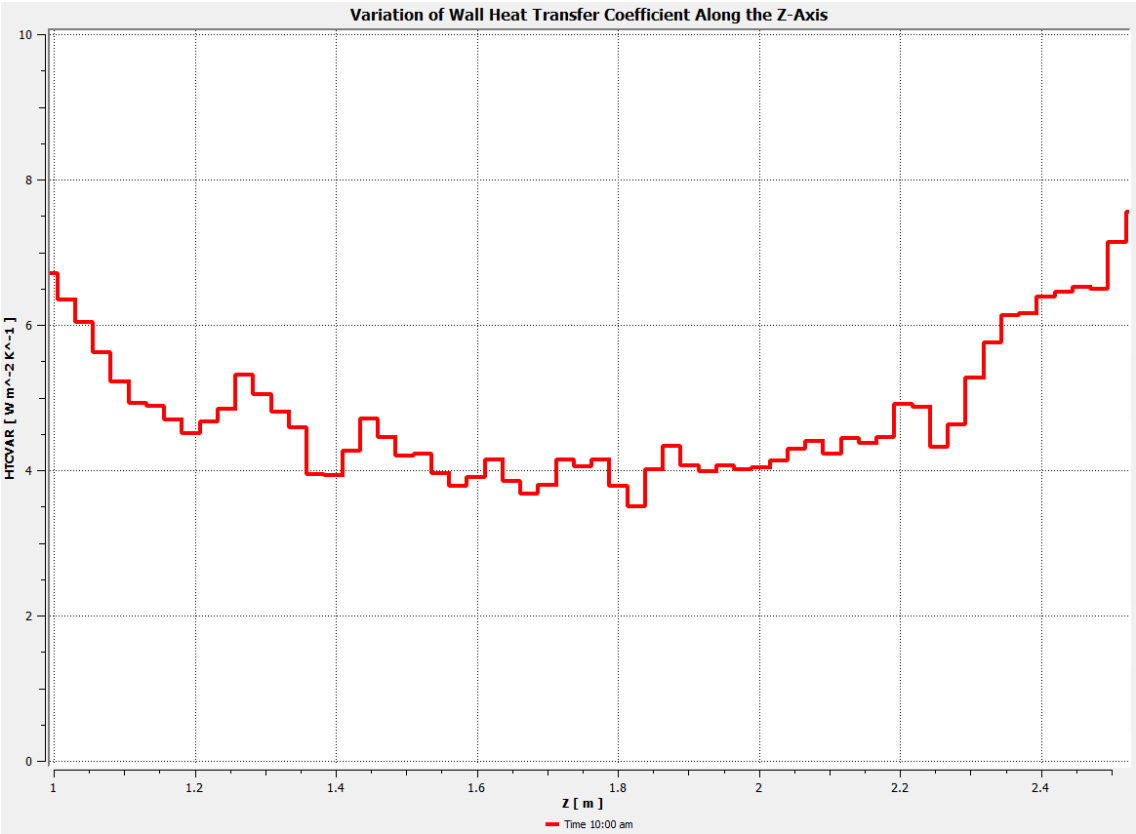

Figure 66: Wall Heat Transfer Coefficient Variation along the Z-Axis During Preheating at 10:00.

B.3 Convective HTC at 10:06

At 10:06, the maximum flux distribution on the front side of the absorber tube is $2.822 \times 10^3\,\mathrm{W/m^2}$, as illustrated in Figure 67. This results in a non-uniform temperature distribution, as shown in Figure 68. The variations in buoyancy forces represents in Figure 69.

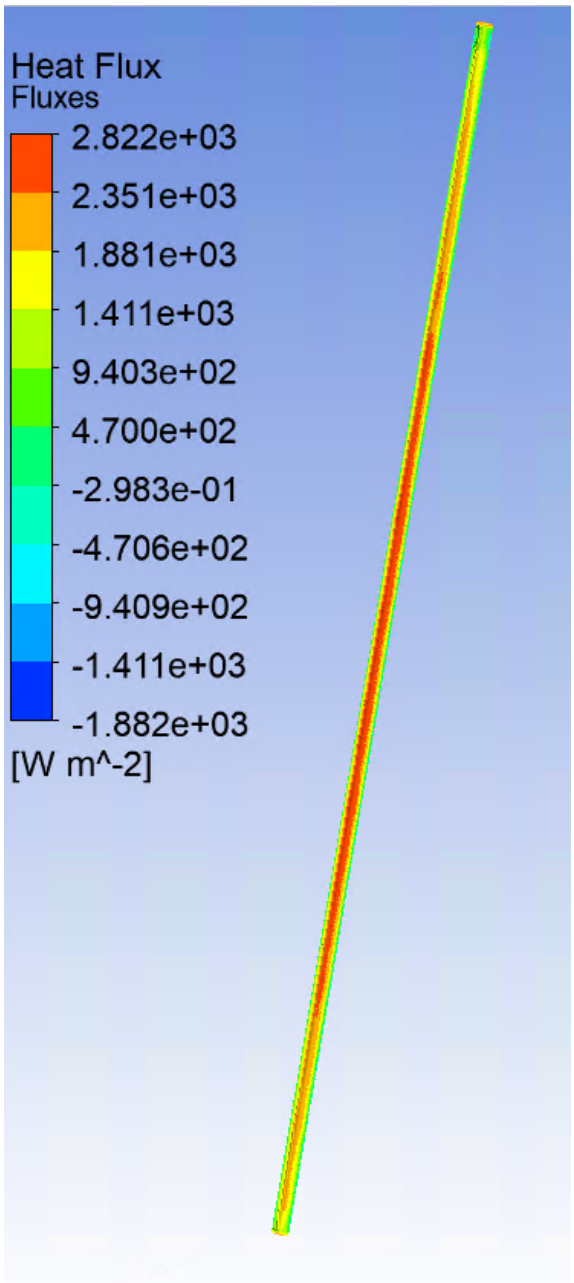

Figure 67: Flux Distribution on the Front Side of the Absorber Tube During Preheating at 10:06.

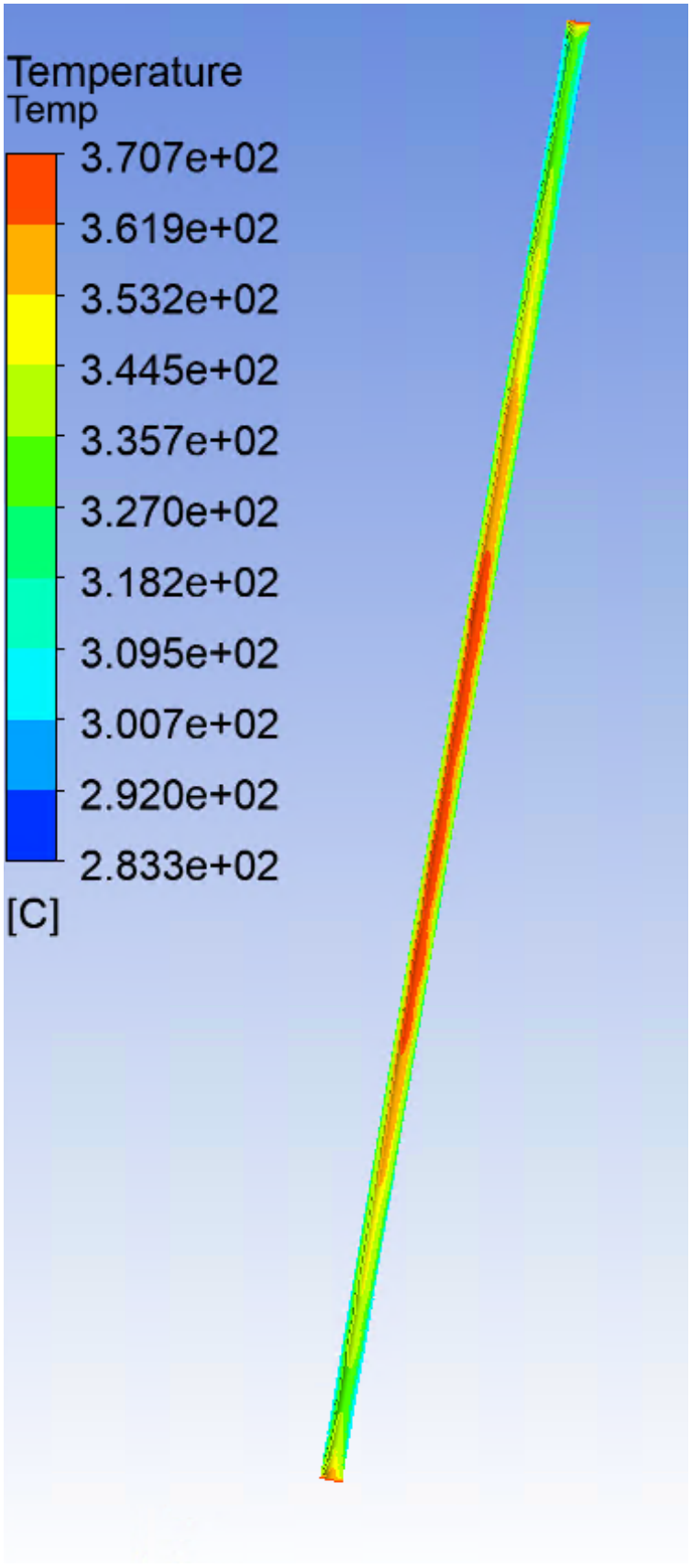

Figure 68: Temperature Distribution on the Front Side of the Absorber Tube During Preheating at 10:06.

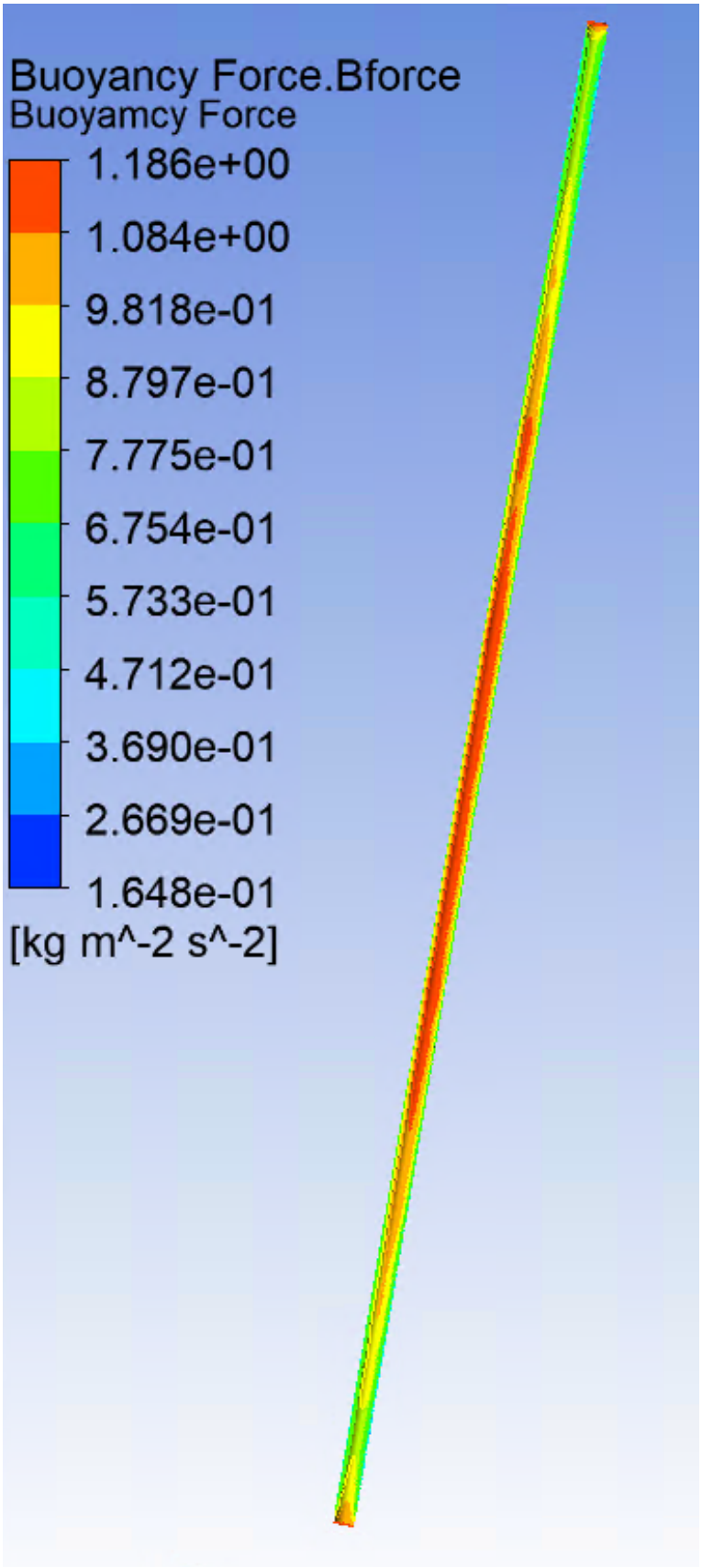

Figure 69: Buoyancy Force Distribution on the Front Side of the Absorber Tube During Preheating at 10:06.

The temperature distribution of air in the ZX plane is illustrated in Figure 70. The simulated temperature was 290.331°C, while the measured temperature was 292.24°C with absolute error 0.65 %.

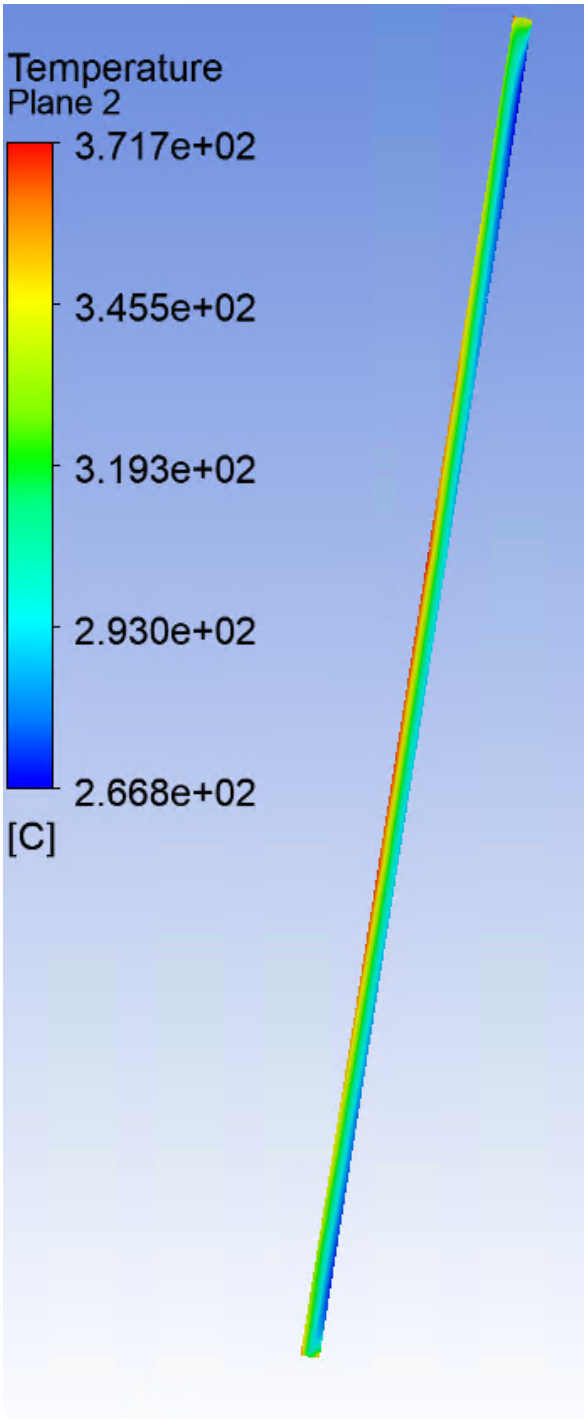

Figure 70: Temperature Distribution in the ZX Plane During Preheating at 10:06.

To calculate the wall HTC within the tube, its variation along the Z-axis is illustrated in Figure 71. The average wall HTC at 10:06 is calculated as 4.48 W/m^2K "Calculated at Average Air Temperature 312.646°C.

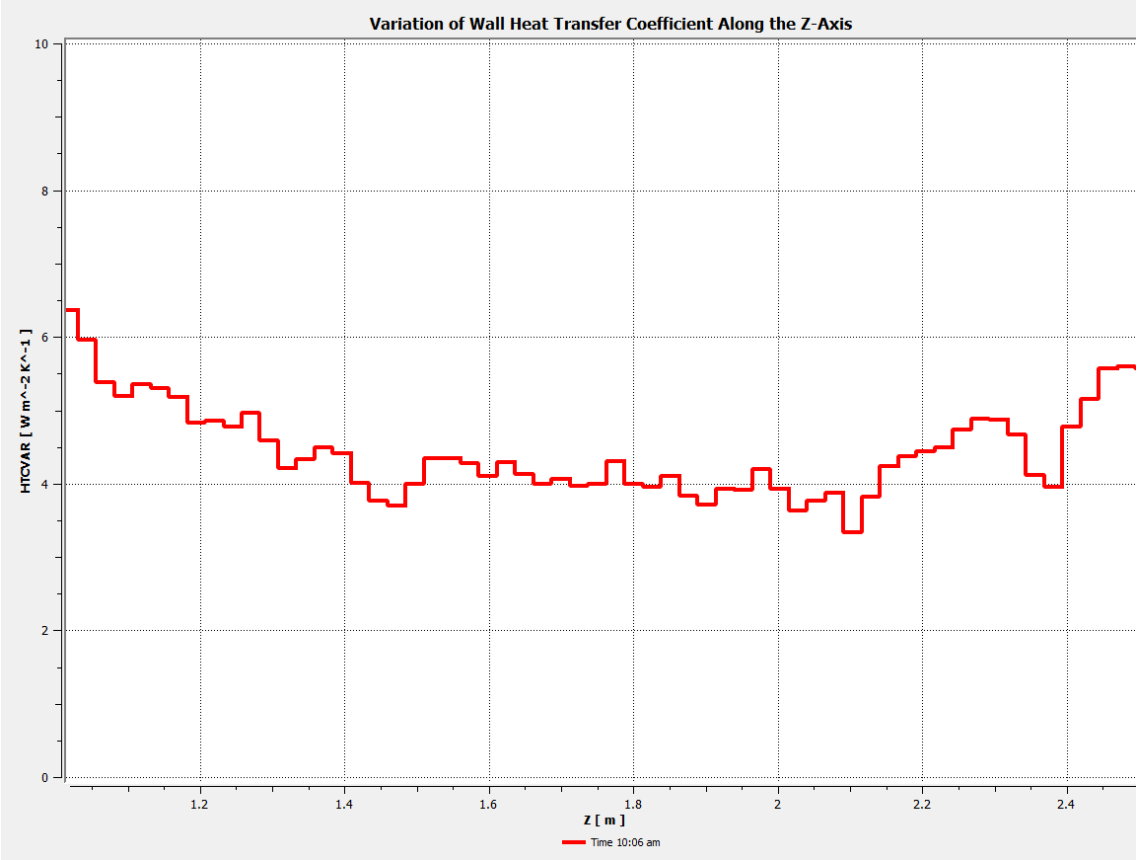

Figure 71: Wall Heat Transfer Coefficient Variation along the Z-Axis During Preheating at 10:06.

C Model Validation

C.1 CFD Model

Designation Model	**Description & Unit**	**Set1**	**Set2**	**Set3**	**Set4**	**Set5**	**Set6**	**Set7**	**Set8**	**Set9**
`n_circ_Absorb`	No. Of Elements over 1/4 pipe circumference (Absorber tubes)	2	4	6	8	10	12	12	12	12
`size_Absorber`	No. Of Elements over axial direction (Absorber tube)	40	80	120	200	300	350	400	450	500
`Fluid_body`	Element size of the Air (Body) [m]	0.1	0.05	0.035	0.03	0.025	0.023	0.02	0.018	0.015
Total nodes		70,523	102,547	152,711	230,674	324,682	373,959	384,846	429,403	499,823
Total Elements		135,610	186,184	297,894	435,964	619,567	676,370	699,212	795,820	940,662

Table 25: Mesh Refinement Analysis for Various Numerical Simulations for CFD Model.

C.2 Thermal Model

Designation Model	**Description & Unit**	**Set$_1$**	**Set$_2$**	**Set$_3$**	**Set$_4$**	**Set$_5$**	**Set$_6$**	**Set$_7$**	**Set$_8$**
`n_circ_Absorb`	No. Of Elements over 1/4 pipe circumference (Absorber tubes)	2	4	8	8	8	8	8	8
`n_circ_VB`	No. Of elements over 1/2 extent (Connecting bend)	2	4	8	8	8	8	8	8
`n_circ_head`	No. Of elements over 1/2 extent (Header)	4	8	16	16	16	16	16	16
`size_Absorber`	Element size in axial direction [m] (Absorber tube)	0.08	0.04	0.03	0.02	0.018	0.015	0.013	0.013
Face Sizing	Element size of insulation areas in contact with VB or header	0.08	0.04	0.03	0.02	0.018	0.015	0.013	0.013
Line body	Element size of molten salt [m]	0.08	0.04	0.03	0.02	0.018	0.015	0.013	0.013
VB/Absorber Element	Element size refinement at Connecting bend and Absorber tube [m]	0.09	0.045	0.035	0.025	0.0225	0.02	0.018	0.018
VB/Header Element	Element size refinement at Header [m]	0.045	0.0225	0.0175	0.0125	0.0115	0.01	0.009	0.009
`size_insulation`	Element size of the Insulation (Body) [m]	0.2	0.15	0.1	0.1	0.10	0.1	0.1	0.1
size_insulation Faces	Element size of the Insulation (Irradiation Shield) [m]	0.1	0.075	0.05	0.05	0.05	0.05	0.05	0.05
Total nodes		350,373	583,691	912,922	1,342,805	1,559,130	2,147,111	2,424,734	2,482,398
Total Elements		133,476	138,908	230,481	418,618	440,529	772,623	872,776	905,074

Table 26: Mesh Refinement Analysis for Various Numerical Simulations for Thermal Model.

D Tower Dimensions and Coordinates

Tower	Dimensions H,W,D [m]	Coordinates of tower base X,Y,Z [m]
Solar Tower	60.00 X 9.84 X 15.11	0.0,-10.755,0.0
Multifocus Tower	54.00 X 8.64 X 15.00	-17.60,-7.58,0.0

Table 27: Towers Dimensions and Coordinates.

Aim Point Nr.	Coordinates X,Y,Z [m]
0	-17.985 X -3.2 X 29.750
1	-18.170 X -3.2 X 29.750
2	-18.355 X -3.2 X 29.750
3	-18.540 X -3.2 X 29.750
4	-18.725 X -3.2 X 29.750
5	-17.985 X -3.2 X 29.375
6	-18.170 X -3.2 X 29.375
7	-18.355 X -3.2 X 29.375
8	-18.540 X -3.2 X 29.375
9	-18.725 X -3.2 X 29.375
10	-17.985 X -3.2 X 29.000
11	-18.170 X -3.2 X 29.000
12	-18.355 X -3.2 X 29.000
13	-18.540 X -3.2 X 29.000
14	-18.725 X -3.2 X 29.000
15	-17.985 X -3.2 X 28.625
16	-18.170 X-3.2 X 28.625
17	-18.355 X -3.2 X 28.625
18	-18.540 X -3.2 X 28.625
19	-18.725 X -3.2 X 28.625
20	-17.985 X -3.2 X 28.250
21	-18.170 X -3.2 X 28.250
22	-18.355 X -3.2 X 28.250
23	-18.540 X -3.2 X 28.250
24	-18.725 X -3.2 X 28.250

Table 28: Aim Point Coordinates on HPMS-II Receiver.

E Optical Pre-Heating results

Flux Gauge No.	Measurement Results (kW/m^2)	Simulated Results (kW/m^2)	Error (%)
RIR-HMS50-CR001	10.47829914	10.7403	2.500 %
RIR-HMS50-CR002	10.11510982	10.638	5.169 %
RIR-HMS50-CR003	13.11467397	11.5579	**-11.870** %
RIR-HMS50-CR004	11.11505462	11.0298	-0.767 %
RIR-HMS50-CR005	9.818922653	9.6592	-1.627 %
RIR-HMS50-CR006	10.4995557	10.0836	-3.962 %
RIR-HMS50-CR007	12.00173925	11.7587	-2.025 %
RIR-HMS50-CR008	12.32242958	10.8821	**-11.689** %

Table 29: Measured Flux Gauge Values vs. Simulated Results at 9:52 Post-Optimization Simulation, Slope Error = 0.003486, $X_{\text{shifting}} = -0.245$ m and $Z_{\text{shifting}} = -0.131$ m.

Flux Gauge No.	Measurement Results (kW/m^2)	Simulated Results (kW/m^2)	Error (%)
RIR-HMS50-CR001	12.52791405	12.9128	3.072 %
RIR-HMS50-CR002	12.82097551	12.9311	0.859 %
RIR-HMS50-CR003	14.68348277	13.7239	-6.535 %
RIR-HMS50-CR004	13.40341595	13.2649	-1.033 %
RIR-HMS50-CR005	12.08923782	11.4834	-5.011 %
RIR-HMS50-CR006	13.34316635	11.5077	**-13.756** %
RIR-HMS50-CR007	13.59731211	13.1969	-2.945 %
RIR-HMS50-CR008	14.65935094	12.3047	**-16.062** %

Table 30: Measured Flux Gauge Values vs. Simulated Results at 9:54 Post-Optimization Simulation, Slope Error = 0.003361 , $X_{\text{shifting}} = -0.165$ m and $Z_{\text{shifting}} = -0.294$ m.

Flux Gauge No.	Measurement Results (kW/m^2)	Simulated Results (kW/m^2)	Error (%)
RIR-HMS50-CR001	12.77875204	13.9309	9.016 %
RIR-HMS50-CR002	13.03896543	13.7101	5.147 %
RIR-HMS50-CR003	15.11631584	14.0474	-7.071 %
RIR-HMS50-CR004	13.66722584	13.6448	-0.164 %
RIR-HMS50-CR005	12.24746166	11.825	-3.449 %
RIR-HMS50-CR006	13.4361993	11.534	**-14.157** %
RIR-HMS50-CR007	14.0761595	13.9328	-1.018 %
RIR-HMS50-CR008	15.01942036	13.9852	-6.886 %

Table 31: Measured Flux Gauge Values vs. Simulated Results at 9:56 Post-Optimization Simulation, Slope Error = 0.003274 , $X_{\text{shifting}} = -0.038$ m and $Z_{\text{shifting}} = -0.197$ m.

Flux Gauge No.	Measurement Results (kW/m^2)	Simulated Results (kW/m^2)	Error (%)
RIR-HMS50-CR001	13.79536172	14.4239	4.556 %
RIR-HMS50-CR002	14.025326733	14.4213	2.823 %
RIR-HMS50-CR003	15.26574132	15.4755	1.374 %
RIR-HMS50-CR004	14.29147674	14.8997	4.256 %
RIR-HMS50-CR005	13.65819964	13.3306	-2.399 %
RIR-HMS50-CR006	14.97296483	13.3346	**-10.942** %
RIR-HMS50-CR007	14.03517516	14.0529	0.126 %
RIR-HMS50-CR008	15.80607216	13.9674	**-11.633** %

Table 32: Measured Flux Gauge Values vs. Simulated Results at 9:58 Post-Optimization Simulation, Slope Error = 0.003401 , $X_{\text{shifting}} = -0.093$ m and $Z_{\text{shifting}} = -0.189$ m.

Flux Gauge No.	Measurement Results (kW/m^2)	Simulated Results (kW/m^2)	Error (%)
RIR-HMS50-CR001	14.8391819	15.6573	5.513 %
RIR-HMS50-CR002	14.84008561	15.7606	6.203 %
RIR-HMS50-CR003	16.54879276	15.6644	-5.344 %
RIR-HMS50-CR004	14.76693668	15.9361	7.917 %
RIR-HMS50-CR005	15.481087	13.7126	**-11.424** %
RIR-HMS50-CR006	16.03266325	13.9717	**-12.855** %
RIR-HMS50-CR007	15.43913962	15.1695	-1.746 %
RIR-HMS50-CR008	16.05875247	14.3093	**-10.894** %

Table 33: Measured Flux Gauge Values vs. Simulated Results at 10:00 Post-Optimization Simulation, Slope Error = 0.003447 , $X_{\text{shifting}} = -0.0170$ m and $Z_{\text{shifting}} = -0.1883$ m.

Flux Gauge No.	Measurement Results (kW/m^2)	Simulated Results (kW/m^2)	Error (%)
RIR-HMS50-CR001	16.82879224	18.0256	7.112 %
RIR-HMS50-CR002	16.21603734	17.1252	5.607 %
RIR-HMS50-CR003	18.37716699	18.7625	2.097 %
RIR-HMS50-CR004	16.20100729	16.8156	3.794 %
RIR-HMS50-CR005	16.74722543	15.8938	-5.096 %
RIR-HMS50-CR006	16.91851053	15.6704	-7.377 %
RIR-HMS50-CR007	17.24243629	18.066	4.776 %
RIR-HMS50-CR008	17.44923782	15.8826	**-8.978** %

Table 34: Measured Flux Gauge Values vs. Simulated Results at 10:02 Post-Optimization Simulation, Slope Error = 0.00326 , $X_{\text{shifting}} = -0.19092$ m and $Z_{\text{shifting}} = -0.26705$ m.

Flux Gauge No.	Measurement Results (kW/m^2)	Simulated Results (kW/m^2)	Error (%)
RIR-HMS50-CR001	19.55172845	20.4309	4.497 %
RIR-HMS50-CR002	22.06374857	20.7664	-5.880 %
RIR-HMS50-CR003	20.96644009	20.8392	-0.607 %
RIR-HMS50-CR004	21.05457916	21.888	3.958 %
RIR-HMS50-CR005	19.4705556	18.1609	-6.726 %
RIR-HMS50-CR006	21.37970461	19.4292	**-9.123** %
RIR-HMS50-CR007	19.38270731	19.9311	2.829 %
RIR-HMS50-CR008	21.38584593	19.0265	**-11.032** %

Table 35: Measured Flux Gauge Values vs. Simulated Results at 10:06 Post-Optimization Simulation, Slope Error = 0.00316 , $X_{\text{shifting}} = 0.085$ m and $Z_{\text{shifting}} = -0.358$ m.

Flux Gauge No.	Measurement Results (kW/m^2)	Simulated Results (kW/m^2)	Error (%)
RIR-HMS50-CR001	21.584597869873	21.2838	-1.394 %
RIR-HMS50-CR002	22.335799987793	23.2446	4.069 %
RIR-HMS50-CR003	23.7440894775391	22.6296	-4.694 %
RIR-HMS50-CR004	21.6209850158691	22.7824	5.372 %
RIR-HMS50-CR005	21.1949469451904	19.8223	**-6.476** %
RIR-HMS50-CR006	21.8689886627197	21.2323	-2.911 %
RIR-HMS50-CR007	20.8164487762451	20.7015	-0.552 %
RIR-HMS50-CR008	21.6411277923584	21.1377	-2.326 %

Table 36: Measured Flux Gauge Values vs. Simulated Results at 10:08 Post-Optimization Simulation, Slope Error = 0.003114 , $X_{\text{shifting}} = 0.144785$ m and $Z_{\text{shifting}} = -0.41333$ m.

Flux Gauge No.	Measurement Results (kW/m^2)	Simulated Results (kW/m^2)	Error (%)
RIR-HMS50-CR001	23.3401153411865	24.6418	5.577 %
RIR-HMS50-CR002	23.7912750244141	23.3509	-1.851 %
RIR-HMS50-CR003	26.2813148498535	24.702	-6.009 %
RIR-HMS50-CR004	22.4023857116699	23.2502	3.784 %
RIR-HMS50-CR005	22.2892392730713	22.5883	1.342 %
RIR-HMS50-CR006	23.3399735412598	21.1515	**-9.377** %
RIR-HMS50-CR007	23.2740867919922	22.8948	-1.630 %
RIR-HMS50-CR008	21.8908347320557	21.1539	-3.366 %

Table 37: Measured Flux Gauge Values vs. Simulated Results at 10:10 Post-Optimization Simulation, Slope Error = 0.003011 , $X_{\text{shifting}} = -0.20762$ m and $Z_{\text{shifting}} = -0.4219$ m.

F Temperature Gradient from 9:50 to 10:10 for Various Absorber Tubes

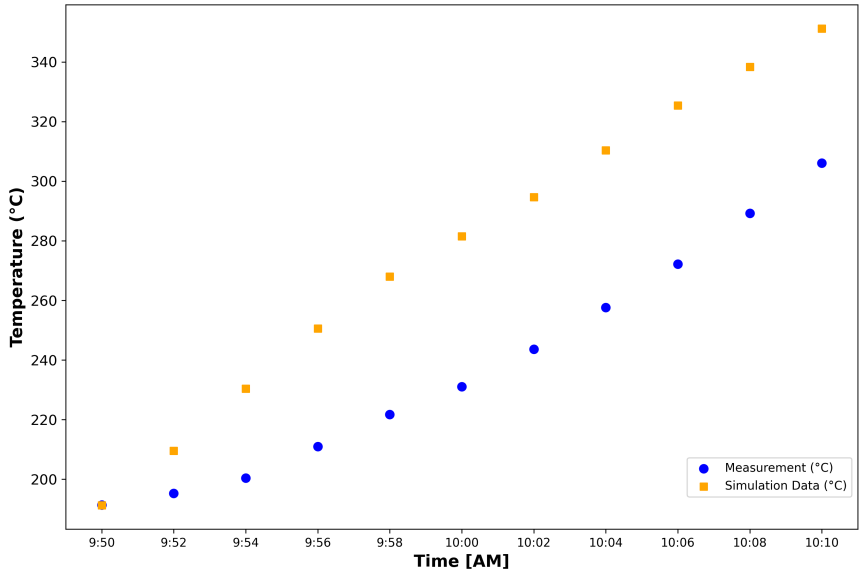

Figure 72: Measured vs. Simulated Temperature Gradients for Absorber Tube_1 from 9:50 to 10:10, Showing a Maximum Absolute Error of 22%.

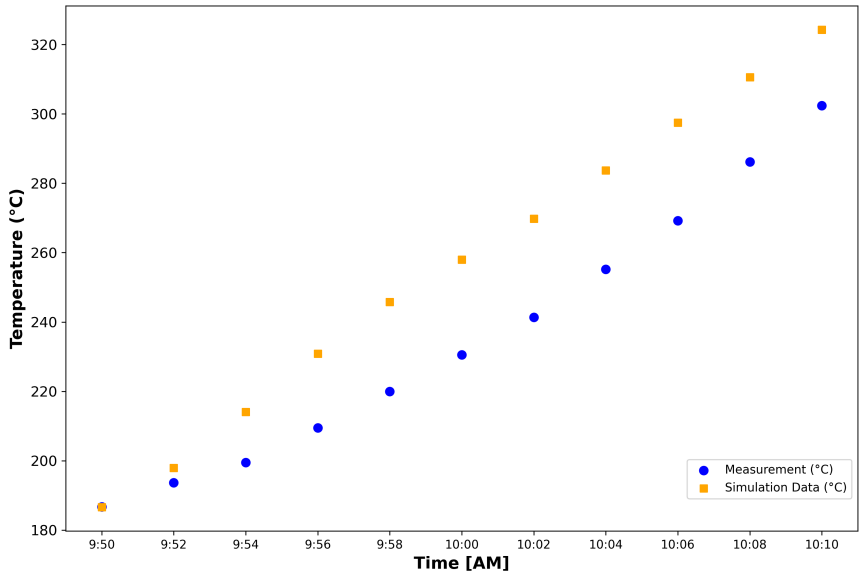

Figure 73: Measured vs. Simulated Temperature Gradients for Absorber Tube_3 from 9:50 to 10:10, Showing a Maximum Absolute Error of 12%.

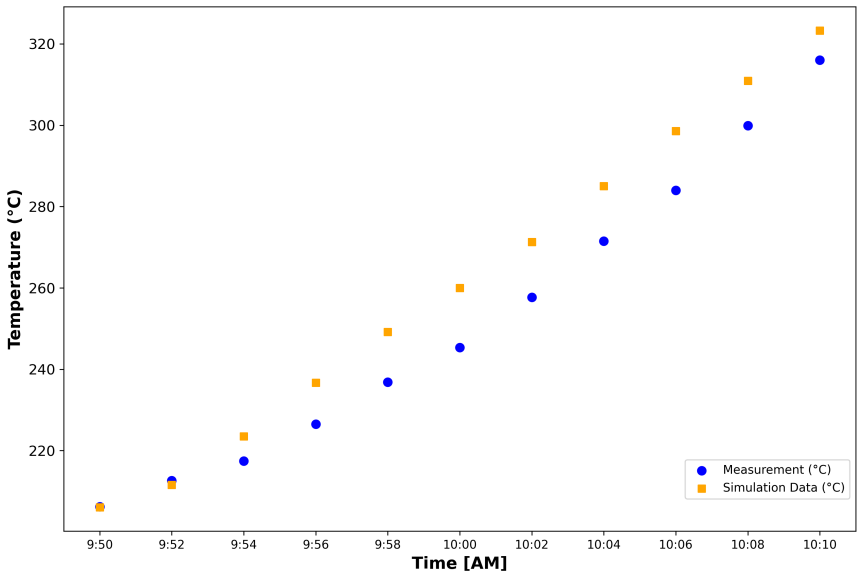

Figure 74: Measured vs. Simulated Temperature Gradients for Absorber Tube_5 from 9:50 to 10:10, Showing a Maximum Absolute Error of 6%.

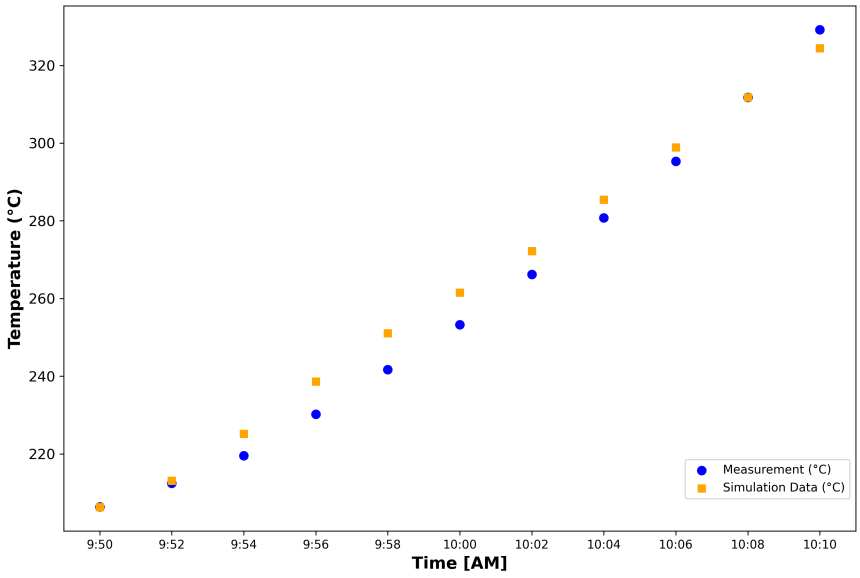

Figure 75: Measured vs. Simulated Temperature Gradients for Absorber Tube_9 from 9:50 to 10:10, Showing a Maximum Absolute Error of 3.3%.

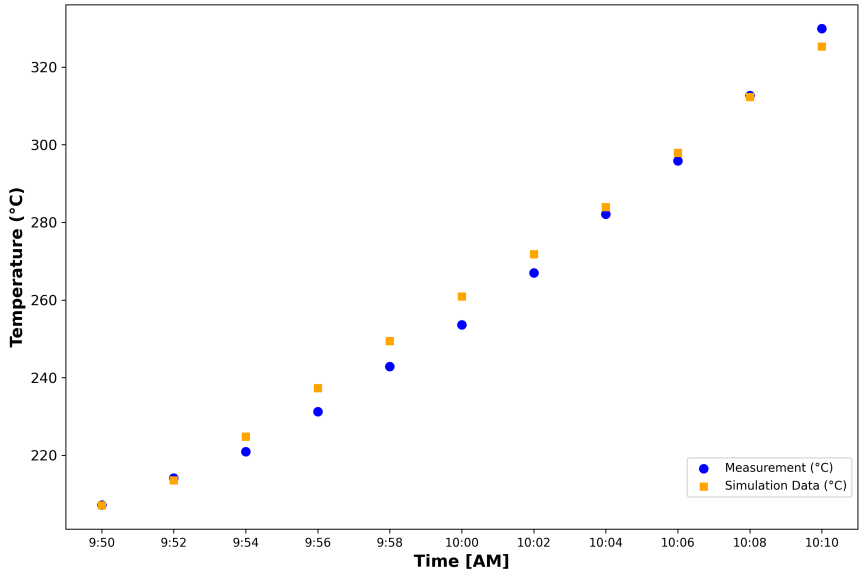

Figure 76: Measured vs. Simulated Temperature Gradients for Absorber Tube_{11} from 9:50 to 10:10, Showing a Maximum Absolute Error of 2.9%.

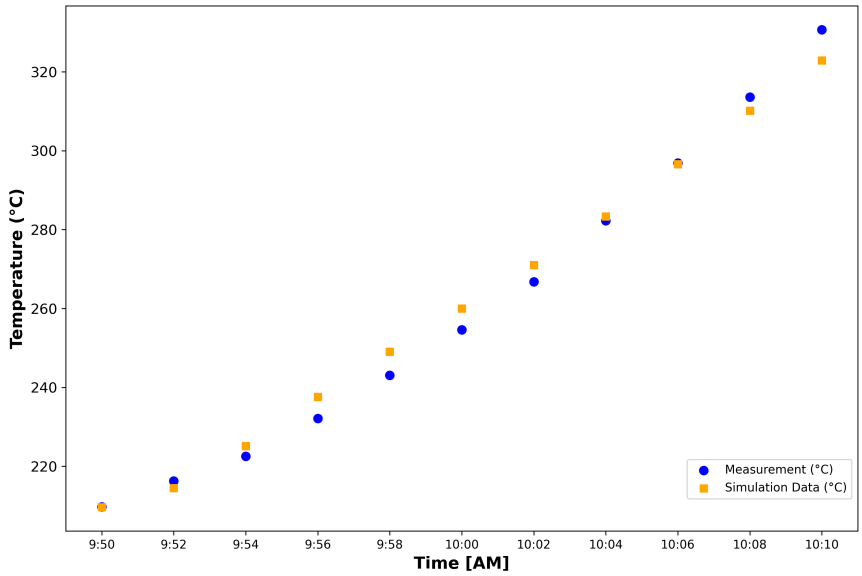

Figure 77: Measured vs. Simulated Temperature Gradients for Absorber Tube_{13} from 9:50 to 10:10, Showing a Maximum Absolute Error of 2.1%.

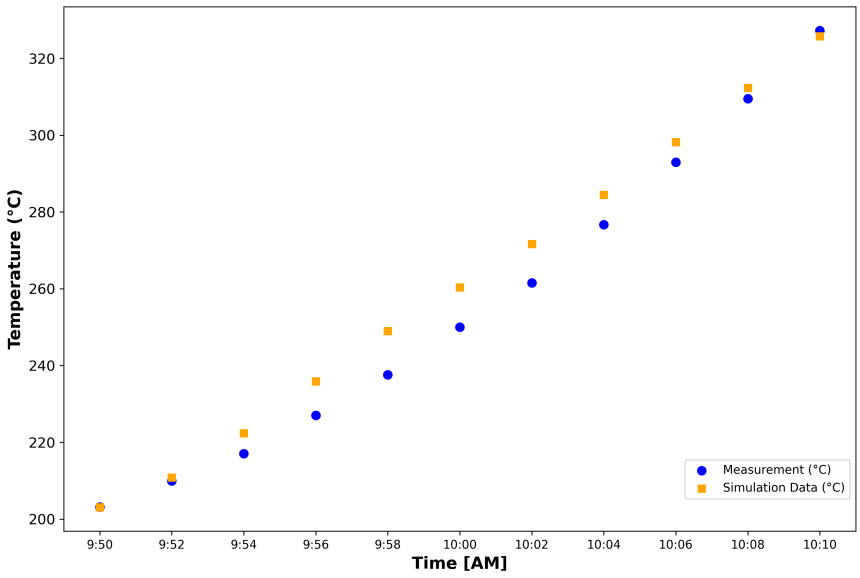

Figure 78: Measured vs. Simulated Temperature Gradients for Absorber Tube_{15} from 9:50 to 10:10, Showing a Maximum Absolute Error of 4.1%.

Bibliography

(IRENA), I. R. E. A. (2021). *Renewable Power Generation Costs in 2020*. Tech. rep. Available: https://www.irena.org/publications/2021/Jun/Renewable-Power-Costs-in-2020. International Renewable Energy Agency.

Albarbar, A. and A. Arar (2019). "Performance Assessment and Improvement of Central Receivers Used for Solar Thermal Plants". In: *Energies* 12, p. 3079. DOI: 10.3390/en12163079.

Besarati, S. M., D. Y. Goswami, and E. K. Stefanakos (2014). "Optimal heliostat aiming strategy for uniform distribution of heat flux on the receiver of a solar power tower plant". In: *Energy Conversion and Management* 84, pp. 234–243. DOI: 10.1016/j.enconman.2014.04.030.

BRADSHAW ROBERT W, e. a. (2002). "Final Test and Evaluation Results from the Solar Two Project". In: *U.S. Department of Energy Office of Scientific and Technical Information*. DOI: https://doi.org/10.2172/793226.

Cathy Frantz Matthias Binder, B. S.-K. and K. Busch (2022). "Basic engineering of a high performance molten salt tower receiver system". In: *AIP Conference Proceedings* 2445.1. DOI: https://doi.org/10.1063/5.0085895.

Çengel, Y. A. (2003). *Heat Transfer A Practical Approach*. 2nd. McGraw-Hill.

Falahat, F. M. and M. R. Gomaa (2022). "A review study on solar tower using different heat transfer fluid". In: *Technology Audit and Production Reserves.* 6. DOI: 10.15587/2706-5448.2022.267560.

Frantz, C., R. Buck, et al. (2023). "Experimental Analysis of Forced Convective Heat Transfer of Nitrate Salt in a Circular Tube at High Reynolds Numbers and Temperatures". In: *International Journal of Heat and Mass Transfer* 201. DOI: 10.1016/j.ijheatmasstransfer.2022.123563.

Frantz, C., M. Ebert, et al. (2023). "Experimental Receiver Setup of a High Performance Molten Salt Test Receiver System". In: *AIP Conference Proceedings* 2815, pp. 100003-1–100003-9. DOI: 10.2172/793226.

García, L., M. Burisch, and M. Sanchez (2015). "Spillage estimation in a heliostats field for solar field optimization". In: *Energy Procedia* 69. International Conference on Concentrating Solar Power and Chemical Energy Systems, SolarPACES 2014, pp. 1269–1276. DOI: 10.1016/j.egypro.2015.03.156.

Geiger1, M., F. Gross1, and R. Buck (2018). "HeliOS Control System Virtually Operates a 100 MW Molten Salt Tower". In: *AIP Conference Proceedings* 2033.1. DOI: 10.1063/1.5067208.

GmbH, M. S. T. (2024). *DMV 310 N: High Temperature Austenitic Stainless Steel*. https://www.dmvtubes.com/fileadmin/DMV/Doc/DMV_DS/DMV310N_SEPT2024.pdf.

Hicdurmaz, S., J. Grobbel, R. Buck, and B. Hoffschmidt (2024). "Modelling reflection in the centrifugal solar particle receiver". In: *Solar Energy* 273. DOI: 10.1016/j.solener.2024.112546.

Ho, C. K. (2016). "A review of high-temperature particle receivers for concentrating solar power". In: *Applied Thermal Engineering* 109, pp. 958–969. DOI: 10.1016/j.applthermaleng.2016.04.103.

Ho, C. K., A. R. Mahoney, et al. (2013). "Characterization of Pyromark 2500 Paint for High-Temperature Solar Receivers". In: *J. Sol. Energy Eng.* 136. DOI: doi.org/10.1115/1.4024031.

Holman, J. P. (2009). *Heat Transfer: A Practical Approach*. 10th. McGraw-Hill.

Hussaini, Z. A., P. King, and C. Sansom (2020). "Numerical Simulation and Design of Multi-Tower Concentrated Solar Power Fields". In: *Sustainability* 12.6. DOI: 10.3390/su12062402.

International Renewable Energy Agency (IRENA) (2024). *Renewable Capacity Statistics 2024*. International Renewable Energy Agency (IRENA).

Kolb, G. J. (2011). "An evaluation of possible next-generation high temperature molten-salt power towers". In: *U.S. Department of Energy Office of Scientific and Technical Information , OSTI.GOV*. DOI: https://doi.org/10.2172/1035342.

Ltd., F. T. (2024). *Alloy 316LN (UNS S31653 / WNR 1.4429): Stainless Steel Tubes*. URL: https://www.finetubes.co.uk/products/materials/stainless-steel-tubes/alloy-316ln-uns-s31653-wnr-14429?utm_source=chatgpt.com.

Mun, J. and A. R. Tutul (2023). "A Review Paper on Performance Analysis and Optimization of Concentrated Solar Power Systems". In: *ResearchGate*.

Pendyala1, R., S. U. Ilyas, and d Yean Sang Wong (2021). "Heat Transfer Performance of Different Fluids During Natural Convection in Enclosures with Varying Aspect Ratios". In: *E3S Web of Conferences* 287. DOI: 10.1051/e3sconf/202128703010.

R.Buck (2024). *Solar Power Raytracing Tool SPRAY , User Manual*.

Reyes Rodríguez Sánchez, M. de los (2015). "On the Design of Solar External Receivers". Directed by Domingo Santana Santana and Carolina Marugán Cruz. PhD thesis. Leganés, Spain: Universidad Carlos III de Madrid, Departamento de Ingeniería Térmica y de Fluidos.

Siebers, D. and J. Kraabel (1984). *Estimating Convective Energy Losses From Solar Centeral Recievers*. Tech. rep. Sandia National Laboratories.

SolarPACES (2024). *CSP Projects Around the World*.

Uhlig, R., C. Frantz, and A. Fritsch (2016). "Effects of vertically ribbed surface roughness on the forced convective heat losses in central receiver systems". In: *AIP Conference Proceedings*. Vol. 1734, p. 030036. DOI: 10.1063/1.4949088.

Zhang, H., J. Baeyens, et al. (2013). "Concentrated solar power plants: Review and design methodology". In: *Renewable and Sustainable Energy Reviews* 22. DOI: 10.1016/j.rser.2013.01.032.

Zhu, G. and C. Libby (2017). "Review and future perspective of central receiver design and performance". In: *AIP Conference Proceedings*. 1850. DOI: 10.1063/1.4984395.